Chair of Geology and Economic Geology

Master's Thesis

Aplite Hosted Reichenspitz-Type Molybdenite Mineralization in the Central Tauern Window, Salzburg/Tyrol

November 2018

Timotheus Martin Christoph Steiner, BSc

Die Eidesstattliche Erklärung muss unterschrieben und mit Datum versehen in Ihre Abschlussarbeit eingebunden werden.

EIDESSTATTLICHE ERKLÄRUNG

Ich erkläre an Eides statt, dass ich diese Arbeit selbständig verfasst, andere als die angegebenen Quellen und Hilfsmittel nicht benutzt, und mich auch sonst keiner unerlaubten Hilfsmittel bedient habe.

Ich erkläre, dass ich die Richtlinien des Senats der Montanuniversität Leoben zu "Gute wissenschaftliche Praxis" gelesen, verstanden und befolgt habe.

Weiters erkläre ich, dass die elektronische und gedruckte Version der eingereichten wissenschaftlichen Abschlussarbeit formal und inhaltlich identisch sind.

Datum 10.11.2018

Unterschrift Verfasser/in
Timotheus Martin Christoph, Steiner
Matrikelnummer: 01335364

Acknowledgments

Many thanks to all, who made this thesis possible. At first, this is addressed to my supervisor Prof. Frank Melcher and the Professors of the Institute of Geology at the MUL whose samples and pre-results could be used. Then it is dedicated to all, who accompanied me at the fieldwork, namely Frank Melcher, Alexander Ordosch, Max Berger, Christoph Lassl and Regina Finkel. My thanks are also addressed to Prof. Thomas Meisel and Prof. Gerd Rantitsch, who helped me with the chemical analyses. Further, I want to thank the technicians preparing my thin sections. Last, but definitively not least, I want to thank my parents, who enabled me to choose this field of study.

Abstract

Vein-type Mo mineralization is known from the Subpenninic Central Gneis units in the Tauern Window of the Eastern Alps; the type locality is located at the Alpeinerscharte in the Tux gneiss core. The aplitic granite (known as Reichenspitzgranit) building up the Reichenspitze at the border Salzburg/Tyrol (Austria) is host to low-grade molybdenum mineralization showing slightly differing structural and mineralogical attributes. It is bound to the area Reichenspitze-Gabler-upper Mannlkar-upper Roßkar and the ridge N-Zillerscharte to Zillerplattenscharte. Both areas yield variably sized aplitic stocks. Significant glacial retreat of the last 60 years made an update of the geological map necessary, as additional aplite bodies and faults became exposed. The post-orogenic A-type aplitic granites intruded at 282±6 Ma (Besang et al., 1968) into older Variscan I-type plutons. SiO_2 contents of the aplites range from 73-77%, clearly distinguishable from 70-73% SiO_2 of the gneisses. Both lithologies are low in CaO (1-3% for the gneisses; below 1% for the aplites), and the aplites are enriched in K_2O compared to the gneisses (3-4% for the gneisses; 4-6% for the aplites). The aplites have a high content of high field strength elements and a negative Eu anomaly (chondrite normalized). In the pneumatolytic stage, a low-grade low fluorine calc-alkaline molybdenum porphyry system developed, probably similar to the Endako porphyry in British Columbia. The molybdenite formed in quartz veins and impregnations, that are often associated with ENE-WSW trending regional faults. Accessory minerals are pyrite, traces of chalcopyrite, minor Bi-Te minerals (native bismuth, bismuthinite and other phases), uraninite and thorite. The mineralization is enriched in Mo, Cu, Y, Ce, Rb, Th and U, and depleted in Ba, Sr and Li with respect to the host rocks. The Oligocene thermal event (Tauernkristallisation) of the Alpine orogenesis reached at least upper greenschist facies conditions and produced a widespread saussuritisation of plagioclase. During this event, a complex assemblage of secondary Mo-bearing minerals, rare earth element-bearing minerals (e.g., a conspicuous allanite-zircon-thorite assemblage) and a variety of poorly characterized Bi-bearing phases formed due to remobilization.

Zusammenfassung

In den subpenninischen Zentralgneisen des Tauernfensters treten ganggebundene Molybdänmineralisationen auf; die Typlokalität ist die Alpeiner Scharte im Tuxer Kern. Im die Reichenspitze aufbauenden Aplitgranit ist eine Molybdänmineralisation mit abweichenden mineralogischen und strukturellen Eigenschaften entwickelt. Die Mineralisation ist an die Bereiche Reichenspitze-Gabler-oberes Mannlkar-oberes Roßkar und den Grat N-Zillerscharte zur Zillerplattenscharte gebunden. Ein signifikanter Gletscherrückgang in den letzten 60 Jahren

machte ein Update der geologischen Karte notwendig, da dadurch zusätzliche aplitische Intrusionskörper und Störungen aufgeschlossen wurden. Der postorogene A-Typ Aplitgranit ist vor 282±6 Millionen Jahren (Besang et al., 1968) in die umgebenden älteren, ebenfalls variszischen I-Typ Plutone intrudiert. Der Aplitgranit hat SiO_2 Gehalte von 73-77%, die Gneise weisen 70-73% SiO_2 auf. Beide Lithologien haben einen niedrigen CaO-Gehalt (1-3% bei den Gneisen; unter 1% bei den Apliten) und die Aplite sind im Verhältnis zu den Gneisen an K_2O angereichert (3-4% bei den Gneisen; 4-6% bei den Apliten). Die Aplite sind mit high field strength elements angereichert und weisen eine negative chondritnormalisierte Eu Anomalie auf. Im pneumatolytischen Stadium entwickelte sich ein low-grade low fluorine calc-alkaline molybdenum porphyry system, das Ähnlichkeit mit dem Mo Porphyry in Endako, British Columbia hat. Der Molybdänit tritt in Quarzgängen und Imprägnationen gemeinsam mit wenig Pyrit und Spuren von Chalkopyrit, Bi-Te-Mineralen (gediegen Wismut, Bismuthinit und andere Phasen), Uraninit and Thorit auf und ist oft mit ENE-WSW streichenden regionalen Störungen assoziiert. In der Mineralisation sind Mo, Cu, Y, Ce, Rb, Th und U gegenüber dem Nebengestein angereichert, Ba, Sr und Li sind abgereichert. Während der alpidischen Orogenese wurden im Zuge der Tauernkristallisation zumindest Bedingungen der oberen Grünschieferfazies erreicht und es erfolgte eine verbreitete Saussuritisierung der Plagioklase. Dabei bildeten sich durch Remobilisation sekundäre Molybdänminerale, Seltene Erden enthaltende Minerale (z.B. eine auffällige Allanit-Zirkon-Thorit Vergesellschaftung) und verschiedene analytisch schlecht charakterisierbare Bi-Phasen.

Table of contents

1 Introduction

The studied area is located at the western margin of Salzburg, SW of Krimml in the Reichenspitzgruppe. 35 km W is the Alpeinerscharte Mo deposit, at which exploration work was conducted during World War II (Anonymus, 1943). The studied mineralization is one of 8 known Mo mineralizations ("GBA: IRIS - Interaktives RohstoffInformationsSystem," 2018) in the Tauern Window and a typical occurrence regarding the aplitic host rock, as the others are hosted in various granite types and sulfide-quartz veins (Meixner, 1952).

The Mo mineralization in the Reichenspitze area is known since the geological mapping in the 1960´s (Karl, 1964; Schmidegg, 1964), but there was almost no work conducted on the mineralization except some collectors searching for mineral specimen (Burgsteiner, 2017; Walter et al., 2016). Exploratory fieldwork has been conducted by scientists of the Montanuniversität Leoben in collaboration with collectors of the Schurfgemeinschaft Zinkwand in the years 2012-2017. This thesis aims to summarize existing information on this occurrence and to characterize it further.

2 Geological Overview

The working area is situated in the W Tauern window in the Alpine orogen. Figure 1 shows the location marked with the sampled locations mostly in the Tux nappe bordering the Zillertal nappe to the S. Together with the Post-Variscan cover, the Tux nappe, the Zillertal nappe and the Ahorn nappe form the W part of the Venediger duplex complex (Schmid et al., 2013). Altogether, they belong to the Subpenninic nappe system (Schmid et al., 2013, 2004), i.e., they derive from the distal European margin. In the Carboniferous, during the Variscan orogeny and metamorphism, the Tauern Batholith intruded over 100 Ma during four magmatic pulses at ≥370 Ma, 340 Ma, 300-280 Ma and <280 Ma (Eichhorn et al., 2000; Veselá et al., 2011). The intrusive ages correspond to the evolution of the Variscan orogen from an active margin over the collision stage to the orogenic collapse (Eichhorn et al., 2000). In the Triassic (ca. 215 Ma), the breakup of Pangea caused an increased heat-flow resulting in a thermal overprint and crustal-scale faulting (Finger et al., 2017). In the Paleocene, an eclogite event affected the S Tauern Window, which was followed by a blueschist metamorphic event in the Eocene (Schmid et al., 2004). In the Oligocene (30 Ma, Christensen et al., 1994; Finger et al., 2017) conditions reached amphibolite facies related to the closure of the Alpine Tethys (Schmid et al., 2013; Schuster et al., 2004). In the literature, this event is often referred to as Tauernkristallisation.

Due to the exhumation along detachment faults (Brenner fault and Katschberg fault) after the Oligocene, N-S oriented “alpine joints” opened which host the famous Tauerngold.

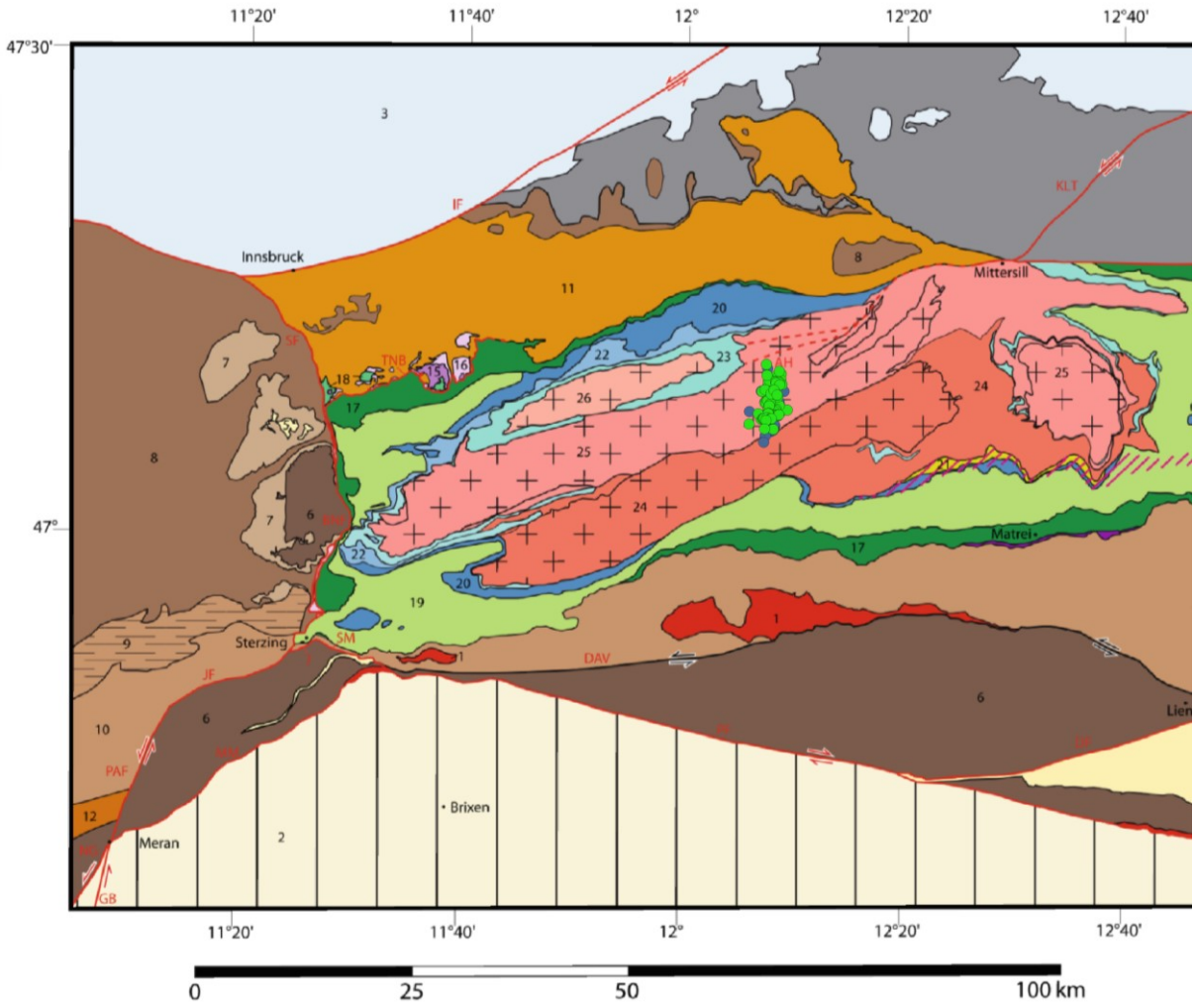

Figure 1: Tectonic overview of the W part of the Tauern Window, the studied area is marked with green and blue points (sampled locations). Modified from Schmid et al. (2013). Legend: 1 = Periadriatic plutons (Oligocene; 2 = Southern Alps; 6 = Basement complexes; 7 = Mesozoic cover; 8 = Variscan basement; 9 = Schneeberg-Radenthein Units; 11 = Innsbruck-Wagrain-Katschberg Quartzphyllite Units; 12 = High-grade Variscan basement; 15 = Lower Austroalpine unit south of the Tauern Window; 16 = Hippold Nappe including Hochfeind Nappe; 17 = Matrei Zone; 19 = Glockner Nappe System; 20 = Modereck Nappe system; 22 = Wolfendorn Nappe; 23 = Post-Variscan cover of nappes in the Venediger Duplex; 24 = Zillertal-Riffl, Sonnblick-Romate and Mureck-Storz nappes; 25 = Tux-Granatspitz and Hochalm nappes; 26 = Ahorn and Göss nappes.

The Tauern Window experienced a polyphase metallogeny starting in the Cambrian and finishing in the Miocene. The ore provinces are described in the IRIS (“GBA: IRIS - Interaktives RohstoffInformationsSystem,” 2018): The oldest deposits are stratabound polymetallic massive sulfide deposits in ophiolitic sequences (“GBA: IRIS - Interaktives RohstoffInformationsSystem,” 2018). The next generation was formed during the Variscan orogeny, outstanding amongst them the Alpeinerscharte Mo deposit (Langthaler et al., 2004; Melcher et al., 1996; Mostler et al., 1982) deposit and the Felbertal scheelite deposit (Höll and Eichhorn, 2000; Kozlik et al., 2016b and references therein). In the Mesozoic, some sedimentary deposits (evaporites) formed on the cover sequences (“GBA: IRIS - Interaktives

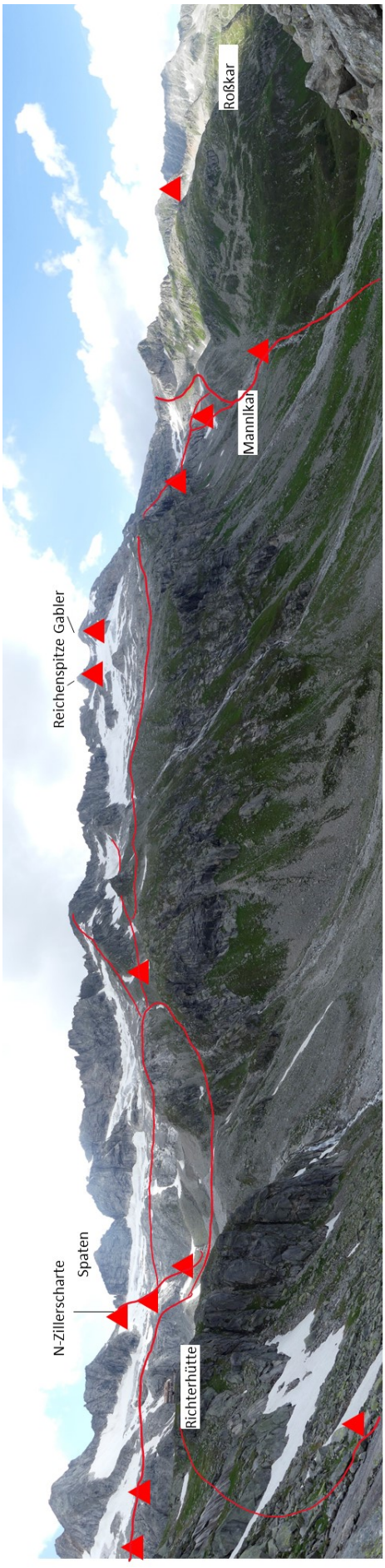

RohstoffInformationsSystem," 2018). During the Alpine orogeny, many deposits were metamorphosed and remobilized leading amongst others to U-Cu mineralizations ("GBA: IRIS - Interaktives RohstoffInformationsSystem," 2018). Finally, in the Miocene gold mineralizations formed in structurally controlled veins in granite gneiss and the schist cover in the central and western Tauern Window due to regional extension ("GBA: IRIS - Interaktives RohstoffInformationsSystem," 2018; Paar et al., 2006).

3 Methods

3.1 Fieldwork

◀*Figure 2: Panoramic view from the ascent to the Richterhütte, red triangles mark samples with Mol, red lines are walked tracks.*

The fieldwork was conducted in the years 2012-2018 by scientists of the Montanuniversität Leoben and members of the Schurfgemeinschaft Zinkwand. Fieldwork for this thesis has been carried out during the summer months in 2017 and 2018. Logistics depended on the alpine hut used as basecamp:

Richterhütte: Drive by car to Krimml (4-5 hours from Leoben), from there with a tourist taxi to the Krimmler Tauernhaus and by foot to the Richterhütte. A ropeway covers the last 300 m altitude difference for material transport, that was used for sample transportation. Up to this place, cycling is possible, but not further on the way up. See Figure 2 for a panoramic view of the working area in the Richterhütte area.

Zittauer Hütte: Drive by car to the Familienhotel Finkau (4-5 hours from Leoben), from there by foot or bike (no speed difference uphill) to the ropeway for material transport to the Zittauer Hütte. The last 300 m altitude gain must be walked, but the backpack can be

transported. The bike was used for a fast and comparatively easy descent with heavy loaded backpacks.

Plauener Hütte: Drive by car to Bärenbad (5 hours from Leoben), from there with a public bus to the dam and by foot in 1.5 hours to the Plauener Hütte.

The fieldwork itself was no mapping but reconnaissance work, see Figure 4 for the tracks and Figures 2 and 3 for field images: The existing paths and easily accessible outcrops were walked and checked for molybdenite mineralization. Lithology changes were noted, but not mapped laterally. Also, the newly ice-free rocks below the glaciers were walked and wherever possible the ridges were climbed or at least approached. In sum, one-fourth of the fieldwork was conducted on paths, the remaining trackless in mostly high-alpine rocky or moraine terrain. Aside from the dangers of the environment one of the main challenges was, that outcrops were either extremely large (e.g., rock faces or giant inclined slabs below glaciers) or covered by moraine material, glaciers or snow.

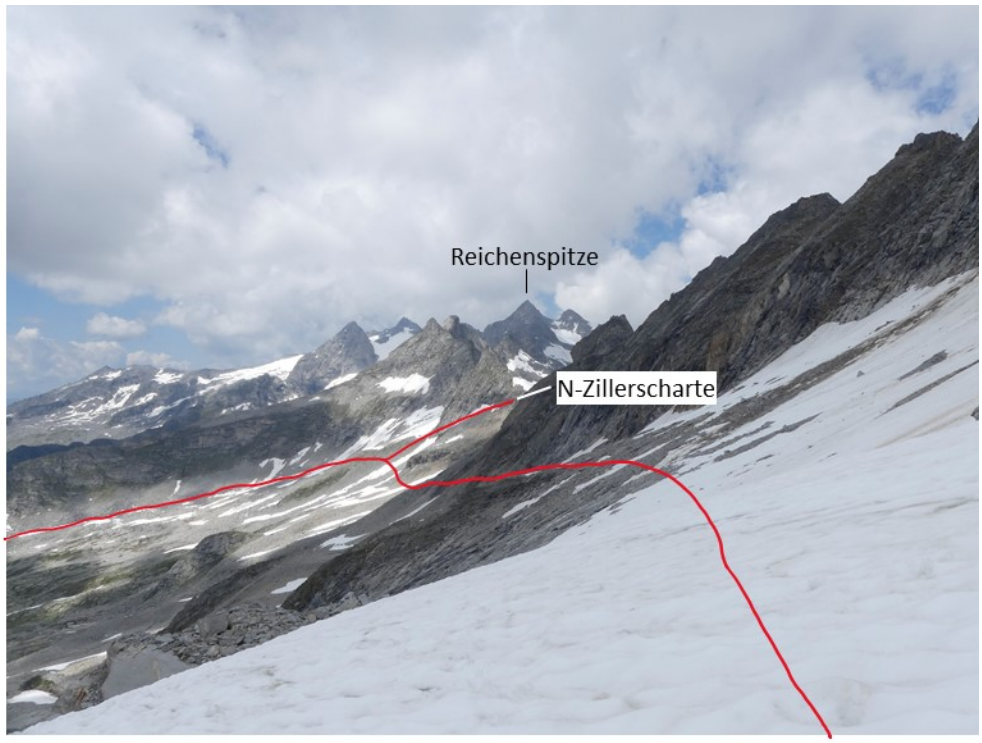

Figure 3: View to the N from below the Zillerplattenspitze, red lines are walked tracks.

For sampling, a 2.5 kg hammer and sometimes a chisel were used to get samples of about 1 kg for geochemical analysis. More was not possible due to the challenging terrain and the long hauling distances to the car to gather a reasonable number of samples. In the years 2017 and 2018, every sample was recorded with GPS coordinates, which were rechecked at the office with georeferenced aerial photographs (Orthophotos from Basemap.at), since the GPS accuracy

can be insufficient in high-relief areas. The list of all samples with GPS coordinates, description and thin section number if available can be found in the Appendix.

3.2 Microscopy

Most samples examined with one of the other methods were examined by optical microscopy as polished 30 µm thin sections with an Olympus B201 and an Olympus BX40 with a Canon EOS 450D for microphotos.

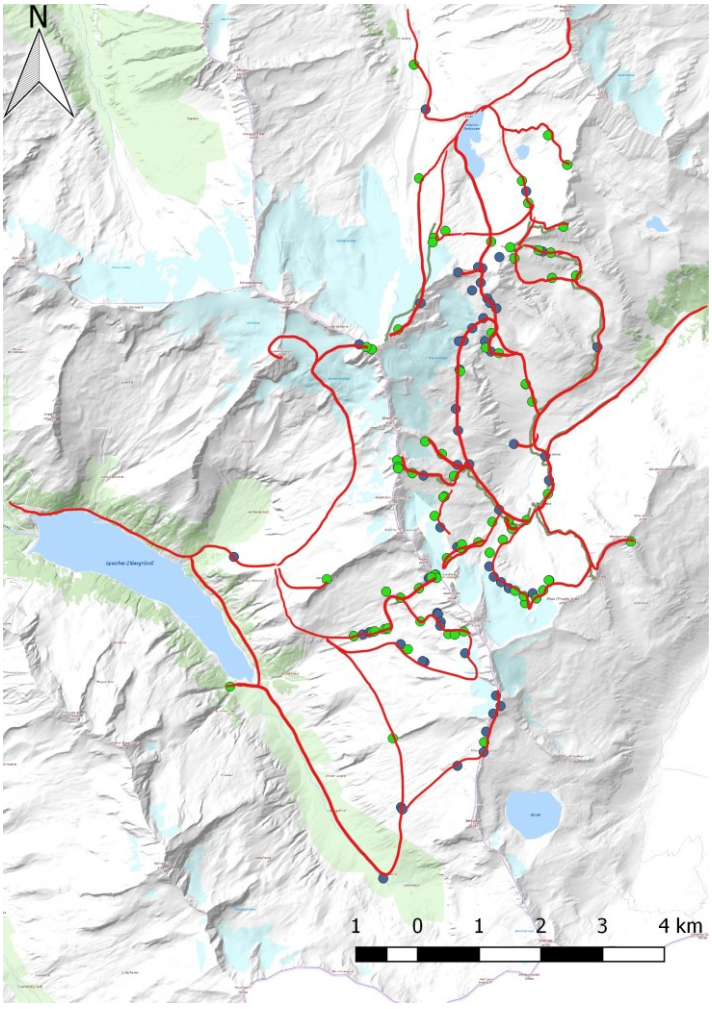

Figure 4: Map of the tracks in the working area. Green points are samples, blue points are mapped features.

3.3 XRF

All samples measured with the XRF were prepared by the following steps:

1. Crushing of at least 500 g sample and milling of at least 100 g with an agate disc mill
2. Drying at 105 °C for at least 2 hours to determine dry mass
3. Burning at 1050 °C for two hours to determine the loss on ignition (LOI)
4. Melting 1 g of the burnt powder with 8 g Lithium borate ($Li_2B_4O_7$) to XRF fused discs

The measurements were conducted with Panalytical/Malvern AXIOS XRF instruments at the chair of Geology and Economic Geology the Chair of General and Analytical Chemistry, both at the Montanuniversity Leoben.

3.4 ICP-MS

All samples measured with ICP-MS at the Chair of General and Analytical Chemistry were prepared by the following steps to obtain a sodium peroxide digestion:

1. Weighting in 0.1000 g milled sample and 0.6 g sodium peroxide (Na_2O_2)
2. Burning for 45 minutes at 500 °C in graphite crucibles
3. After cooling putting the crucibles in Teflon cups, filling up the crucibles with deionized water
4. 5 minutes time for reactions while heated to 90 °C and stirred until reactions in the crucibles stop
5. Pouring and washing the graphite crucible in the Teflon cup with deionized water
6. Filling everything from the Teflon cup in a tube and centrifuge
7. Decanting in a 100 ml flask
8. Filling the solid residue with 3 ml 3 molar hydrochloric acid (HCl) and shake until complete dissolution, then pouring in the flask
9. Washing the graphite crucible with 2 ml concentrated HCl and pouring that in the flask
10. Filling up the 100 ml flask with deionized water and homogenizing
11. Keeping 50 ml for the measurements in a screw tube
12. Pipetting 1 ml from the screw tube in a test tube
13. Pipetting 4 ml nitric acid (HNO_3) and 100 µl of a Ge/In/Re standard solution in the test tube

The measurements were conducted with an Agilent Technologies 7500ce ICP-MS.

3.5 SEM

All samples analyzed using the SEM, a Zeiss Evo MA 10, were polished 30 µm thin sections with vacuum graphite coating. Measuring conditions were 15-20 kV with a Bruker EDX detector.

3.6 Raman

The measurements were conducted with a Jobin Yvon Labram with a 532.2 nm Nd-YAG laser and diffraction gratings of 1200 grooves/mm with an Olympus BX 40 microscope with transmitted light at room temperature.

3.7 Software

For statistical analysis and graph production, the software R with installed GCDkit (Janoušek et al., 2006) was used. Simple diagrams were produced with Microsoft Excel. Maps were produced in QGIS 3.2. The structural data were plotted with Stereonet (Allmendinger et al., 2011; Cardozo and Allmendinger, 2013).

4 Results

4.1 Petrography

Although Schermaier (1993) introduced a new classification scheme for the central gneisses (Zentralgneise) in this area, this study uses modernized names after Karl (1964, 1963, 1962, 1961), which are also used in the geological map (Karl and Schmidegg, 1979). The exact classification would have gone beyond the scope of a master thesis. Moreover, it is not relevant for the problem and comparison with the geological map is easier for successor researchers. For the new classification, the reader is referred to Schermaier (1993) pages 115-118.

4.1.1 Granitic Ortho-Gneiss (Augen- und Flasergneise sensu Karl)

Augengneiss is the dominant lithology in the studied area. As the German name suggests, they are orthogneisses with large (up to 3 cm) bright feldspar clasts, mostly K-feldspar, and many mafic enclaves (Figure 5b). The modal composition leads to granitic protoliths originating from fractional crystallization. The orthogneiss is nearly everywhere foliated and in some areas mylonitic. The mylonitic shear zones formed during a late stage of the Alpine orogenesis since they do not show any younger deformation, strike SW-NE and contain sheared alpine joints.

Figure 5a shows a typical Augengneiss with a sheared joint.

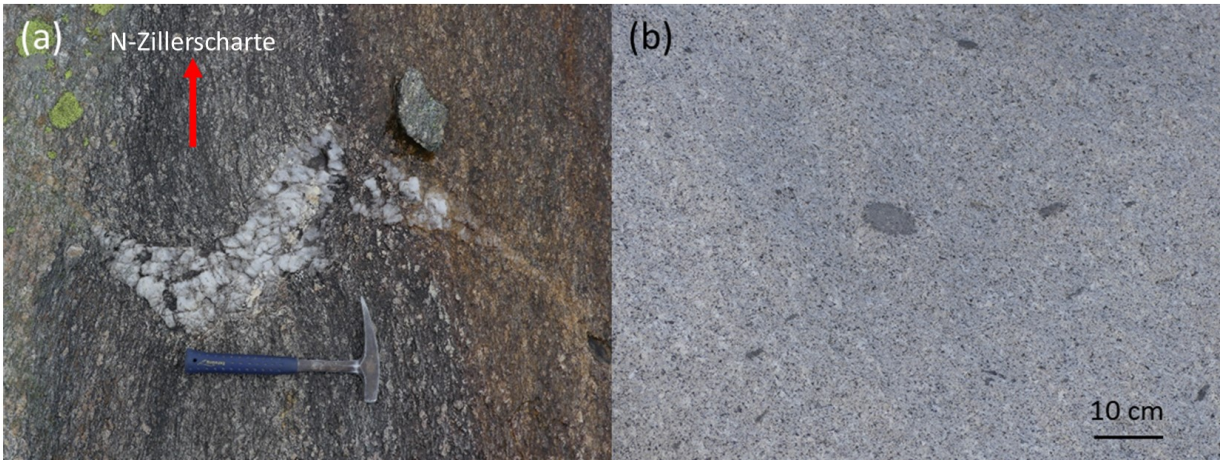

Figure 5: Orthogneiss; a: sheared alpine joint in sheared gneiss. 300 m SW of N Zillerscharte on glacial polish in the shear zone; undeformed gneiss with mafic enclaves at the Hanemannweg below the N Zillerscharte.

Figure 6 shows a typical example of the Augengneiss with large K-feldspar clasts surrounded by smaller grains of quartz, chlorite, often biotite or muscovite (in this case not visible) and plagioclase. Note, that the plagioclase is strongly saussuritizised. This is not everywhere the case, but very often and especially in the proximity to the aplitic granite and can change even on the scale of a thin section. Garnet, zircon and epidote are common accessories.

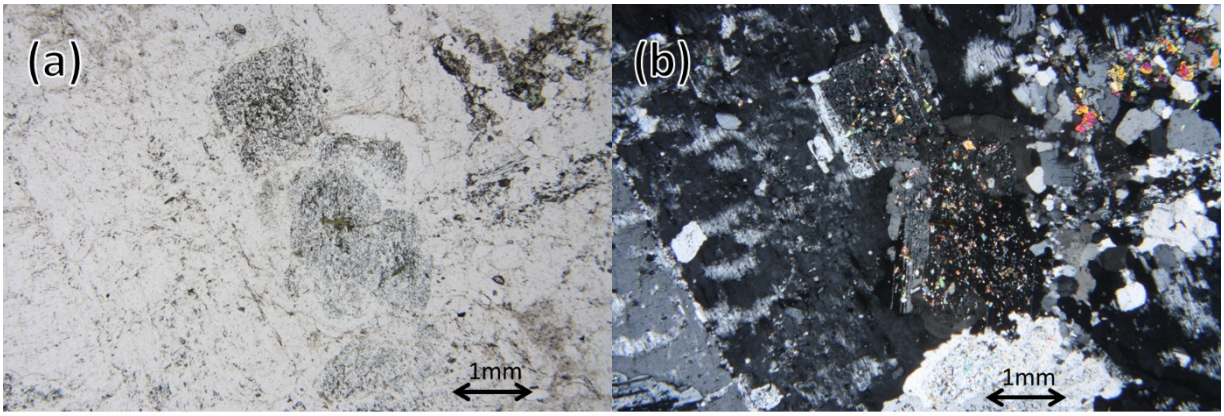

Figure 6:Microscopic images of the Augengneiss. (a) II N, (b) X N. The large crystal to the left is a twinned K-feldspars, in the center are saussuritizised plagioclases, the rounded grey grains to the right are quartzes, the greenish grains are chlorites and the grains with higher interference colors are zircons. Sample 15RH16.

4.1.2 Mafic dykes (Basischer Gang sensu Karl)

Distributed throughout the area are mafic dykes following the general foliation trend. Most of them are 1-5 m thick, although there are some thicker examples (about 20 m seen on the N face of the Roßkarscharte). They contain xenoliths of the host rock and (Figure 8, sample 17PH13 from the Zillerplattenscharte).

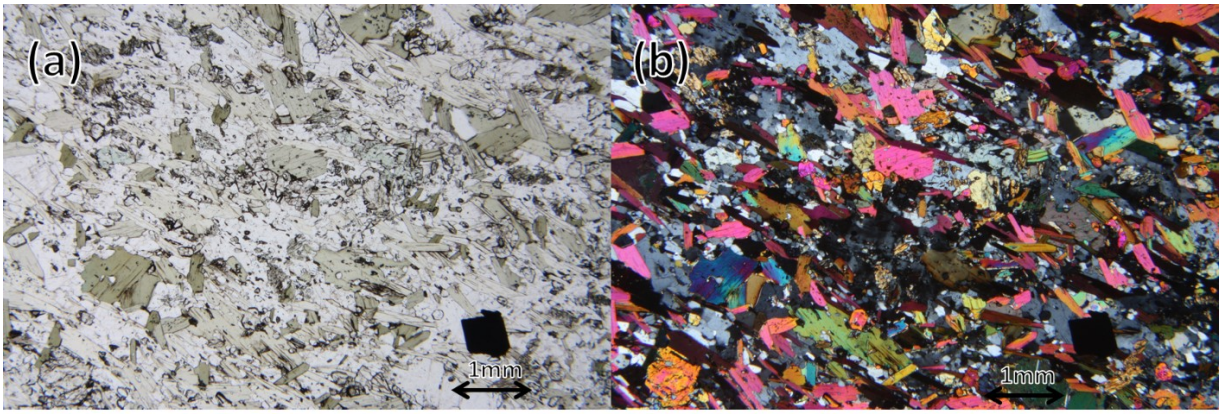

Figure 7: Microscopic images of the mafic dykes. (a) II N, (b) X N. Colorless minerals are plagioclase and quartz, green minerals are chlorite, epidote and amphibole, the dark cube to the lower right is pyrite. Sample 15RH14.

Figure 8: Mafic dyke with aplitic xenoliths (next to the hammer) in aplitic granite, E flank of mount Gabler.

Figure 7 shows microscopic images of the mafic dykes. As they encountered at least two metamorphic events, they are present as amphibole-bearing chlorite-epidote-schists now. Other main components are quartz, plagioclase and orthoclase; accessories are calcite, pyrite, titanite and apatite. The minerals were identified using Raman spectroscopy.

4.1.3 Aplitic Granite (Aplitgranit des Typus Reichenspitze sensu Karl)

The type locality of the aplitic granite is the highest peak in the studied area, the Reichenspitze (3303 m). It is the youngest granite in the area (Finger et al., 1993; Karl, 1962, 1961; Schermaier, 1993), which could be confirmed as intrusion contacts are visible. Figure 9 shows hand specimen of the aplitic granite in the typical coarse-grained, aplitic and slightly greenish appearance.

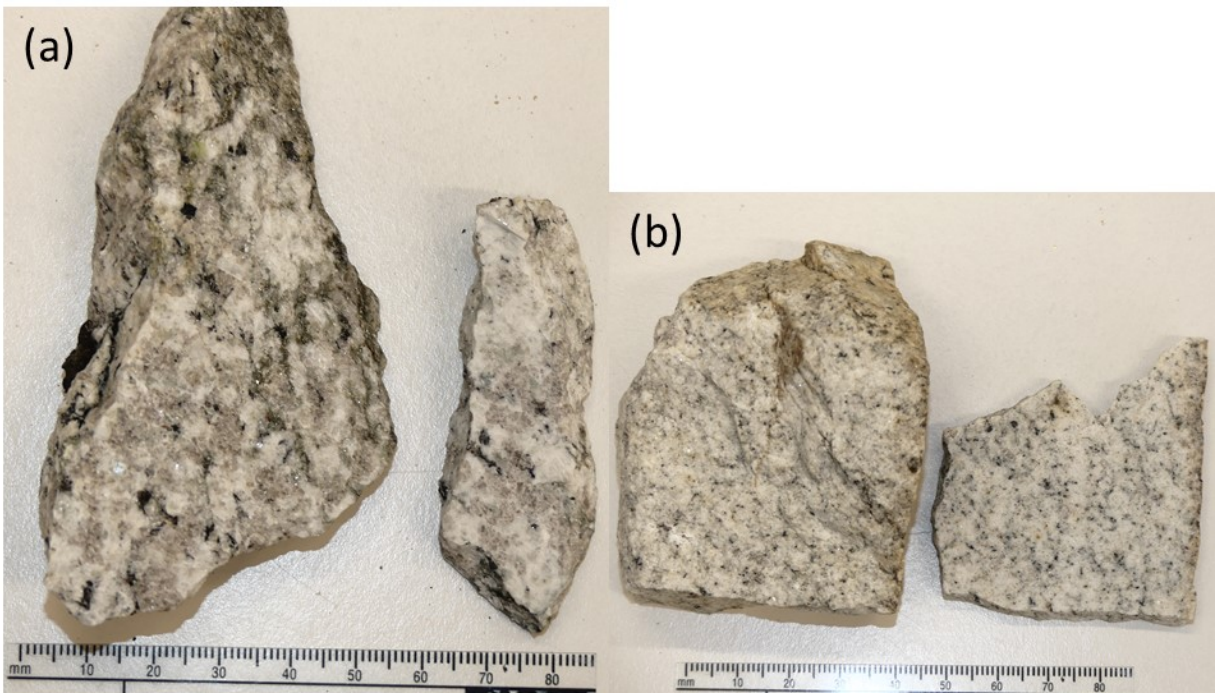

Figure 9: Hand specimen of the aplitic granite; a: sample 17PH01, b: sample 17PH10.

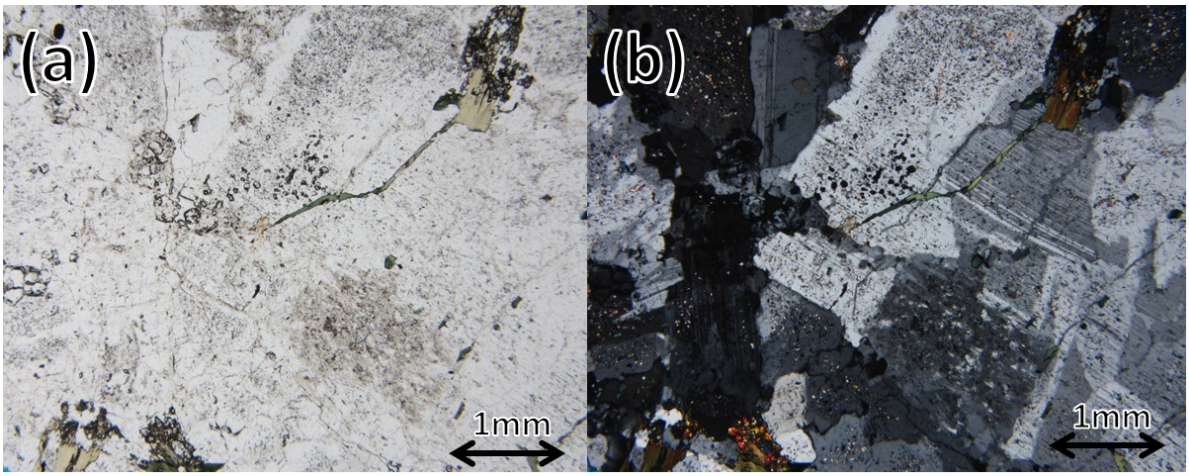

Figure 10: Microscopic images of the aplitic granite. (a) II N, (b) X N. The large crystals with polysynthetic twinning and microliths are plagioclase, in the left part is quartz (destructive interference), the green platy minerals are chlorites and the small grains with higher interference colors in the lower left corner are zircons. Sample 17PH01.

The main components of the aplitic granite are quartz, plagioclase and K-feldspar; minor components are garnet, chlorite, muscovite and biotite. Accessories are zircon and epidote. K-feldspars are often broken to pieces and look similar to quartz. Most plagioclase is strongly saussuritizised and filled with microlites. Nests of chlorite, garnet, zircon, epidote, the latter often with elevated rare-earth-element (REE) content, are typical. The typical texture is shown in Figure 10.

4.1.4 Molybdenite mineralization

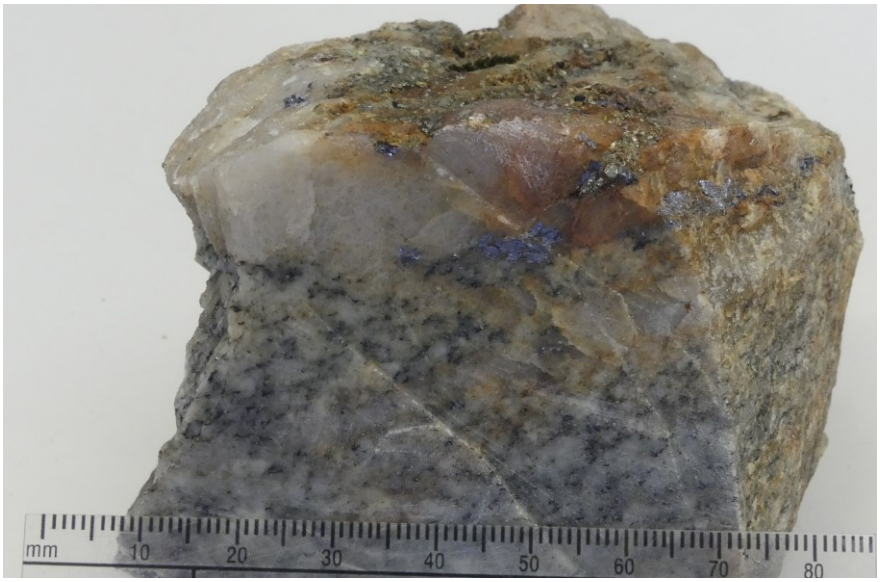

Figure 11: Hand specimen of Augengneiss with mineralized quartz joint (molybdenite and pyrite), sample 18PH5.

Molybdenite occurs in the studied area in two types: in quartz-filled veins (Figures 11 and 12d) and disseminated (Figure 13). The former is less abundant and does not occur in every mineralized zone. However, both are mainly bound to mineralized zones (Figure 17), that differ from non-mineralized zones in terms of field appearance, mineralogy and field appearance. Features are a rusty, often spotted appearance (Figures 11-14) and a slight greenish chlorite alteration. Both are also developed outside these zones, but there is an association with the mineralization. The area around the N-Zillerscharte including some aplitic stocks to the S is mineralized. The Gabler/Reichenspitze area is mineralized (Walter et al., 2016) and there is a mineralization striking from the Mannlkar to the Roßkar, which is probably connected with the Reichenspitze/Gabler mineralization. All occurrences are cut by faults, which are associated with the mineralization, the N-Zillerscharte is the most obvious example with the mineralization reaching the highest grades directly in the shear zone. Molybdenite was sparsely found outside these zones (Figure 17), and if, only in boulders.

The aplite bound disseminated type (Figure 12 c and e, and Figure 13) occurs often as flakes lacking obvious fluid paths (Figure 12e) and in the vicinity of intrusion contacts (sample 18PH12). The vein type has a rusty halo and occurs in aplites (sample 18ZT2) and gneisses (Figure 11, sample 18PH5).

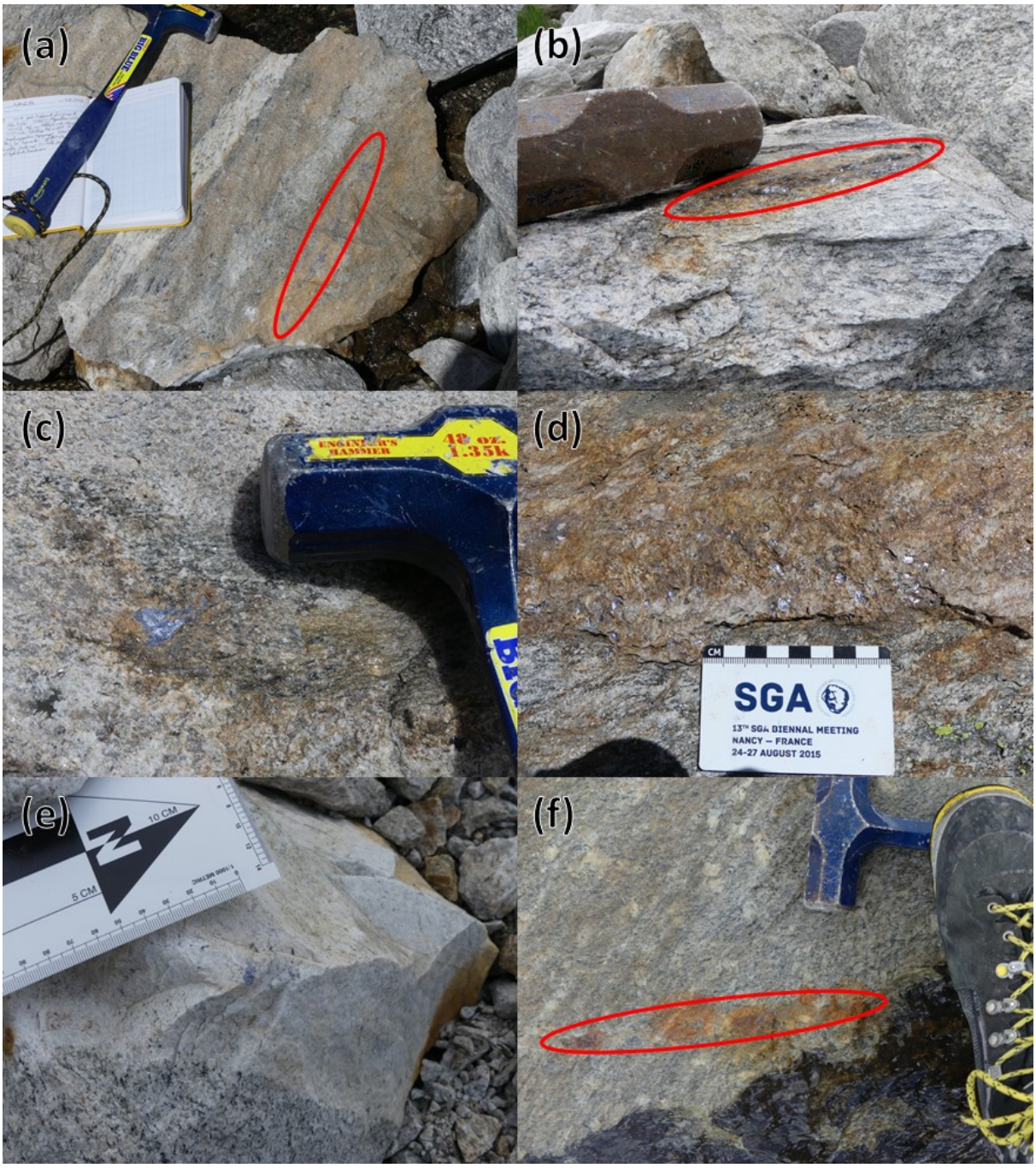

Figure 12: Molybdenites in the field, red ellipses mark molybdenite. a: near the Richterhütte in debris, b: SW of the N-Zillerscharte, c: in the Mannlkar directly on the hiking path, e: in the upper Mannlkar near the ridge to the W, e: near the Richterhütte in debris, f: S of the old Richterhütte below mount Gabler.

Also, mixed types (Figure 12 a, b and f, and Figure 14) can be found, where macroscopically no quartz joint is visible, but the mineralization is distributed along planes. Under the microscope, this type often shows very large muscovite and quartz crystals surrounding the molybdenite. In the mineralized zones abundant molybdenite of either type can be easily found, but outside it is very scarce. Molybdenite is oriented parallel to the Alpine schistosity in all mineralization types.

Figure 13: Hand specimen of aplitic granite with disseminated molybdenite mineralization, sample 17PH07.

Figure 14: Hand specimen of mineralized Augengneiss with the mixed type mineralization, molybdenite is circled red, sample 17RH37.

Under the microscope, the two types are clearly distinguishable. The disseminated type (Figure 15) yields molybdenite aggregates directly in the normal texture. The joint type (Figure 16) yields large quartz and muscovite around the molybdenite aggregates, together they differ significantly from the host rock regarding grain size (larger), texture (no foliation) and paragenesis (no feldspar or accessories). Both mineralization types are often surrounded by heavily saussuritizised plagioclase, a remarkably high density of micro fluid inclusions or rusty grain borders. Unfortunately, the fluid inclusions were too small for further measurements.

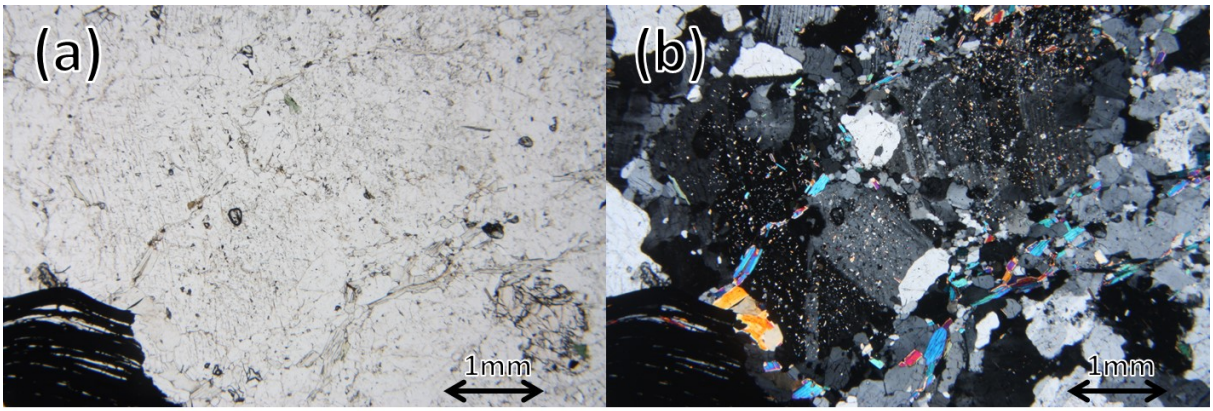

Figure 15: Microscopic images of disseminated molybdenite in aplitic granite. (a) II N, (b) X N. The opaque platy aggregate to the lower left is molybdenite, the squarisch crytals with microliths are plagioclase, in between are small quartz and muscovite (blue and yellow interference colors) and in the lower right corner is a garnet (slightly pinkish in II N, isotropic). Sample 17PH09.

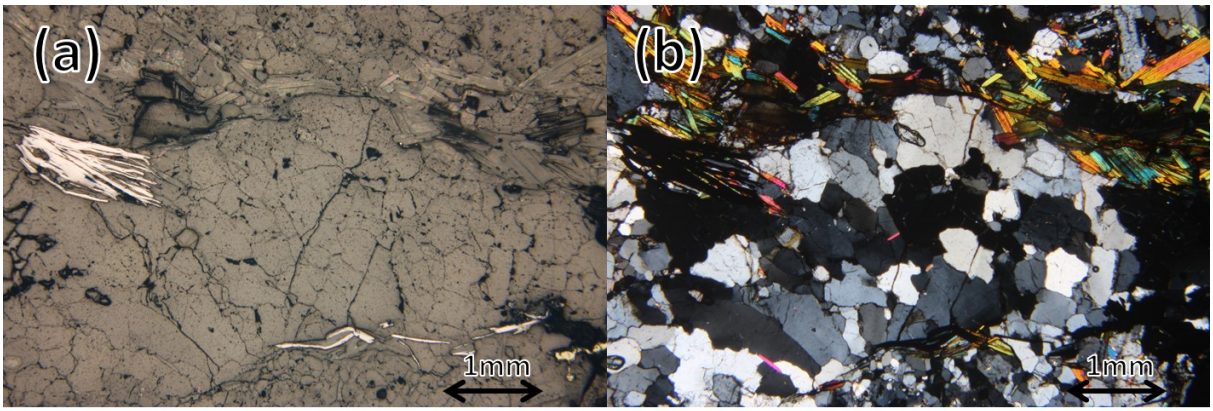

Figure 16: Microscopic images of a quartz joint with molybdenite in granite. (a) reflected light, (b) X N. The grains with low interference colors in the central part are quartz, the platy grains with higher interference colours are muscovite grown in the joint, the platy aggregates with a high white reflection are molybdenite and the small yellow reflecting grain to the lower right is pyrite. Note the significantly smaller grain size of the host rock at the lower and upper edge. Sample 17RH18.

4.1.5 Alpine veins

Throughout the whole area Alpine shear veins, which appear in any lithology are distributed. Most of them are filled with a typical paragenesis of adular (hydrothermal formed orthoclase), quartz, carbonate, chlorite and sometimes muscovite or sulfides in variable portions. Sometimes, the joints are not filled completely and show isomorphic crystals of the named minerals. A typical example can be seen in Figure 5.

4.2 Map and Field Observations

The results of the fieldwork were compiled into an update of the geological map “Blatt Krimml 1:50 000” (Karl and Schmidegg, 1979). The mineralization in the areas Reichenspitze, Rosskar and Gabler is known from the geological mapping, but it was only mentioned without further research (Karl, 1964; Schmidegg, 1964). Most of the geological borders were taken as they are, but there were some changes made:

- Karl and Schmidegg (1979) differentiate between tonalitic gneiss ("Tonalitischer Gneis", unit 47), Augengneiss with aplitic dykes ("Augen- und Flasergneis", unit 48) and granitic gneiss ("Granitischer Gneis", unit 49). This study yielded, that all of them are the same granitic orthogneiss, showing variably strong deformation and a slight fractionation trend. This is particularly obvious at the S limit of the map below the Zillerplattenscharte. There, the hiking path follows a distinct ~50m wide mylonitic shear zone in the granitic orthogneiss, but the geological map displays a lithology change.
- Some large shear zones were mapped
- The glaciers were updated to their extent in the year 2015 (in this year the newest available orthographic photos were produced)
- Due to the glacial retreat, large areas, which were covered by ice during the original mapping, are accessible – although dangerous and not recommended for people without sound alpine experience – and were mapped. In these areas, two additional bodies of aplitic granite were found.
- Some moraines were changed to Alluvium and vice versa based on field evidence and analysis of airborne imagery and the digital elevation model. This could be caused by glacial retreat or availability of modern methods.

It is noticeable, that below 2500 m above sea-level no outcrops of aplitic granite or molybdenite bearing rocks exist, both are concentrated along the ridges with the Reichenspitze as a prominent example and highest peak of the area. It is reasonable to assume, that the aplitic granite as youngest pluton is the most competent and therefore had a higher resistance against the forces of tectonics and erosion producing the highest peaks of the area. Furthermore, it has to be noted, that there is a spatial correlation between large mapped ENE-WSW trending alpine faults or shear zones and molybdenite.

Regarding the young sediments, a differentiation is important in areas being ice-free in 1850 and areas not being ice-free in 1850. While the former are overgrown and stable, the latter yield no significant vegetation and are highly unstable and are regularly affected by debris flows. This is particularly problematic in the area N of the Richterhütte since the hydroelectric power station supplying the hut was destroyed every year since 2016. The best solution to face this

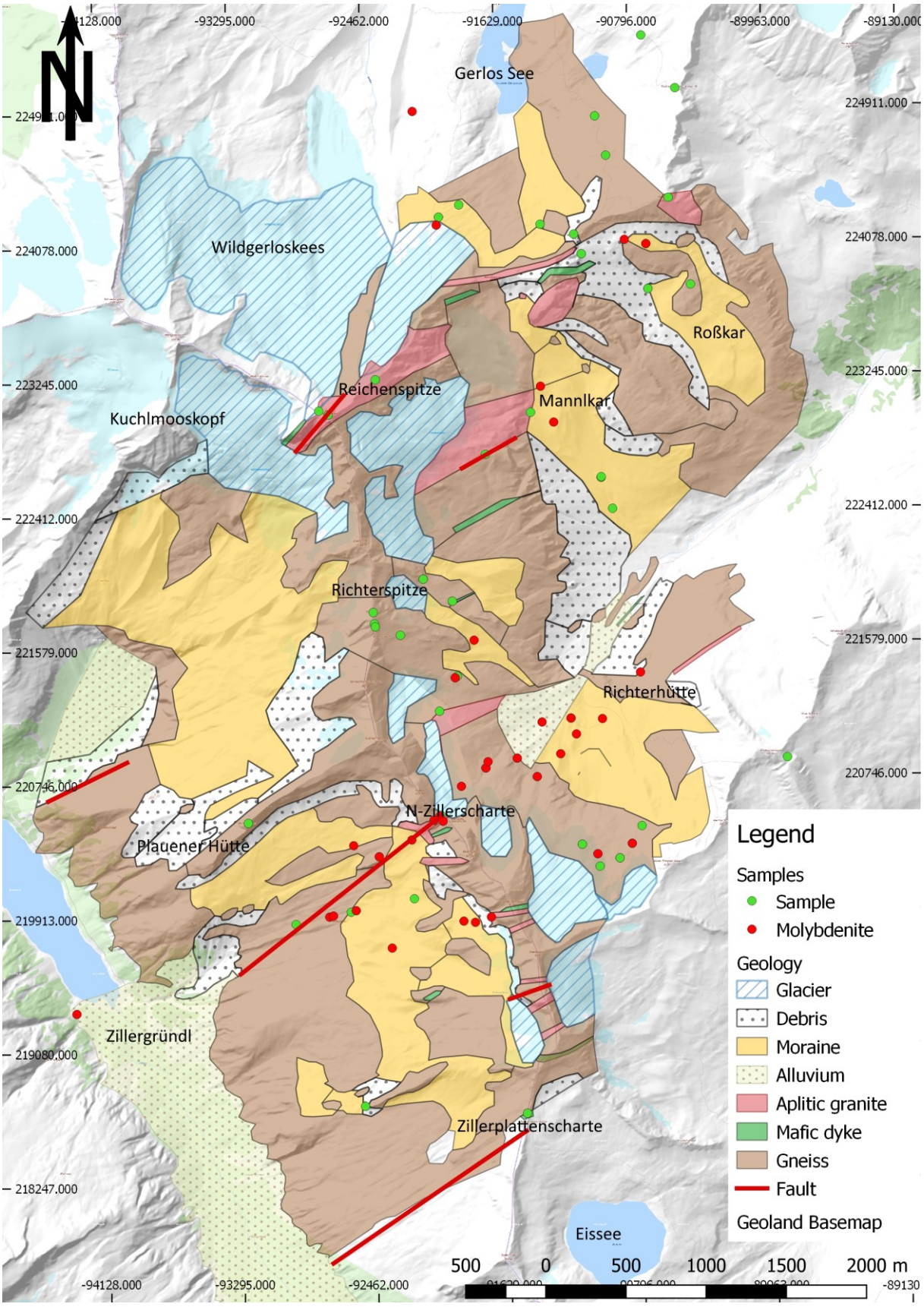

Figure 17: Geological map of the working area. Grid coordinates are in the GK M31 (31255) Austria Central coordinate system.

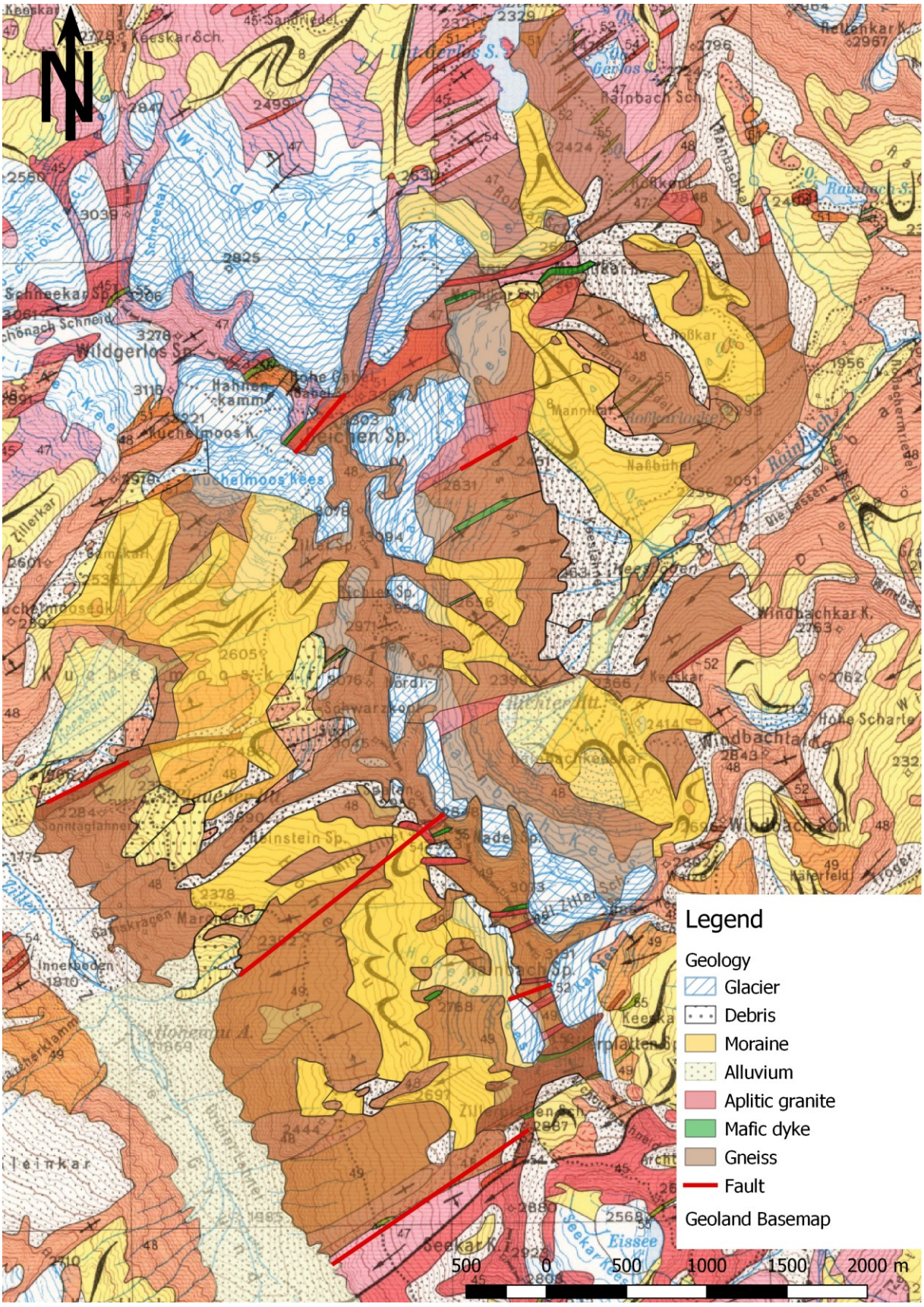

Figure 18: Geological map of the working area with the official geological map (Karl and Schmidegg, 1979) as background.

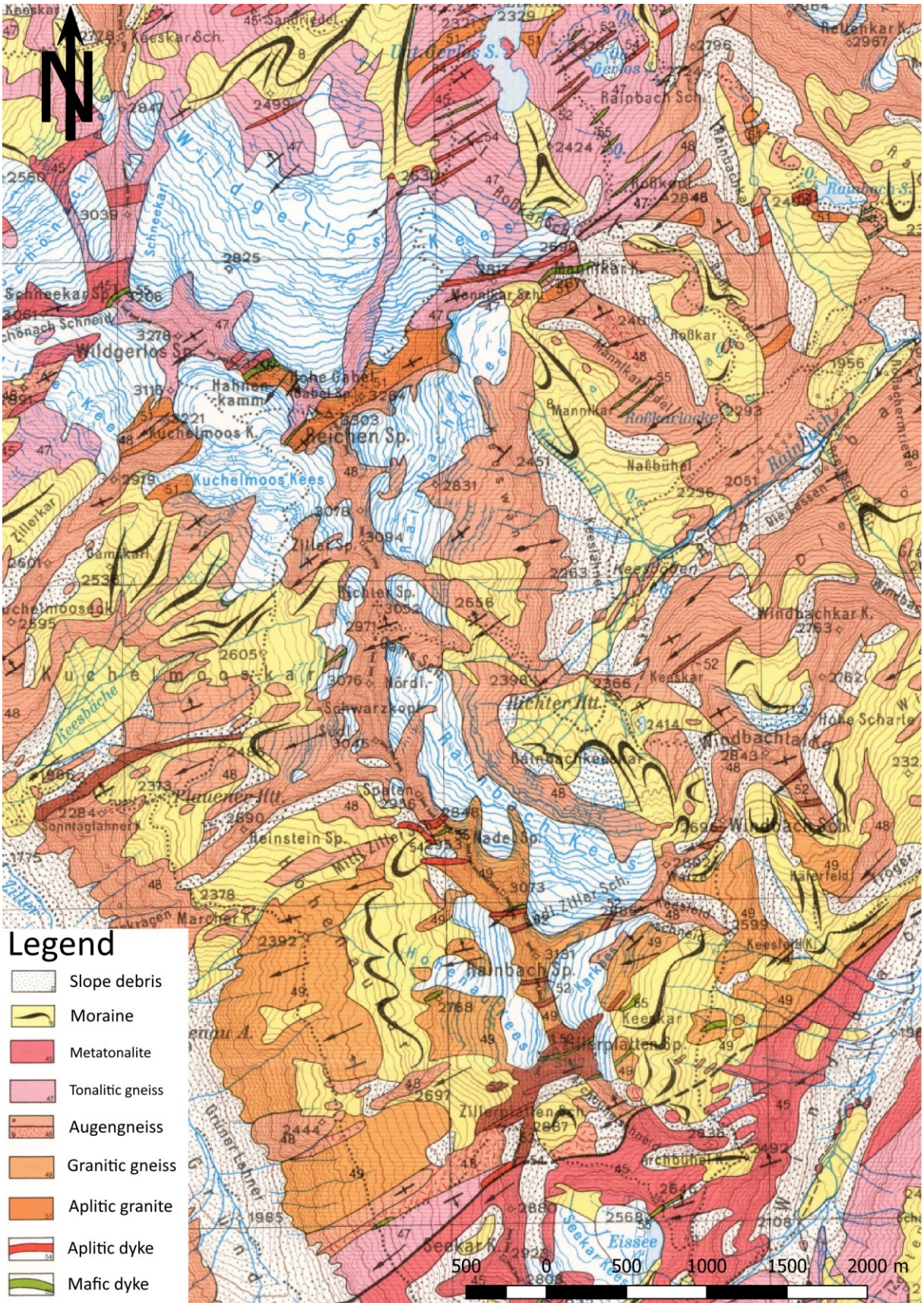

Figure 19: The official geological map (Karl and Schmidegg, 1979), modified to fit the extent of the map area with a reduced legend.

problem would be a reconstruction of the power station in a safe, overgrown area some 100m away since the current one was built directly in the fan.

Figure 17 shows the compiled map with a topographic map as background. Figure 18 compares this map with the geological map (Karl and Schmidegg, 1979) and Figure 19 shows only the geological map for a better comparison.

4.3 Structural geology

The whole Reichenspitz area was affected by Alpine shearing resulting in a uniform E-W striking cleavage dipping steeply to the N (Figure 20). This is also the direction of the major faults (Figure 17) and of many mafic dykes. For the latter, it can be assumed, that they were sheared into this direction. Sheared Alpine mineralized veins (Figure 5a) suggest a dextral shear sense during the late Alpine orogeny. Sharp, straight contacts of mafic dykes (Figure 8) and the aplitic granites (Figure 20b) point to intrusions in a brittle regime and hence low temperatures.

The morphology formed due to the Pleistocene glaciation and is dominated by U-shaped valleys with steep glacial polished walls and moraines in the valley floor. Higher peaks and ridges (e.g. the ridge Zillerplattenscharte-Spaten-Richterspitze-Reichenspitze-Gabler-Mannlkarkopf) are former nunataks and hence deeply cracked and rugged.

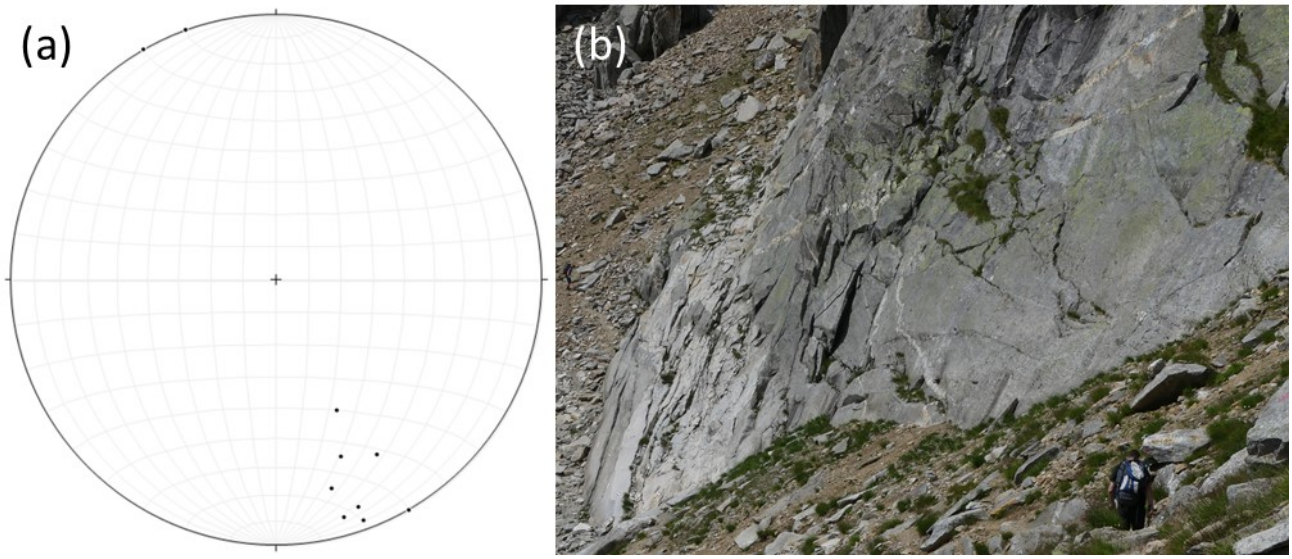

Figure 20: a: Schmidt net of the schistosity planes' pole points, b: intrusive veins of the aplitic granite in gneiss at the hiking path below the Roßkarscharte on the S side.

4.4 Geochemistry

Most samples were measured as fused discs at the XRF of the Chair of Geology and Economic Geology in Leoben. Five samples were also measured for comparison and high-precision trace

element geochemistry at the Chair of General and Analytical Chemistry by ICP-MS and XRF. All data can be found in the Appendix.

4.4.1 Full Digestion

The following samples were measured at the Chair of General and Analytical Chemistry:

- 17PH01: The reference sample for the aplitic granite from the type locality on the summit of the Reichenspitze in the central part of the intrusion. This sample was used as a reference for inter-sample comparison and geotectonic classification.
- 17PH08, 17PH09, 17PH10: Samples from a mineralized fault in the N Zillerscharte with 17PH10 being the most unaltered. Those were chosen to observe gradients in the alteration.
- 17RH26: A mineralized sample from the Roßkar with allanite. The sample is somewhat similar to the aplitic granite microscopically and macroscopically despite its allanite content and was chosen to check geochemical similarity.

The trace element analyses of these samples are used in the discussion for geotectonic classification of the aplitic granites.

4.4.2 XRF

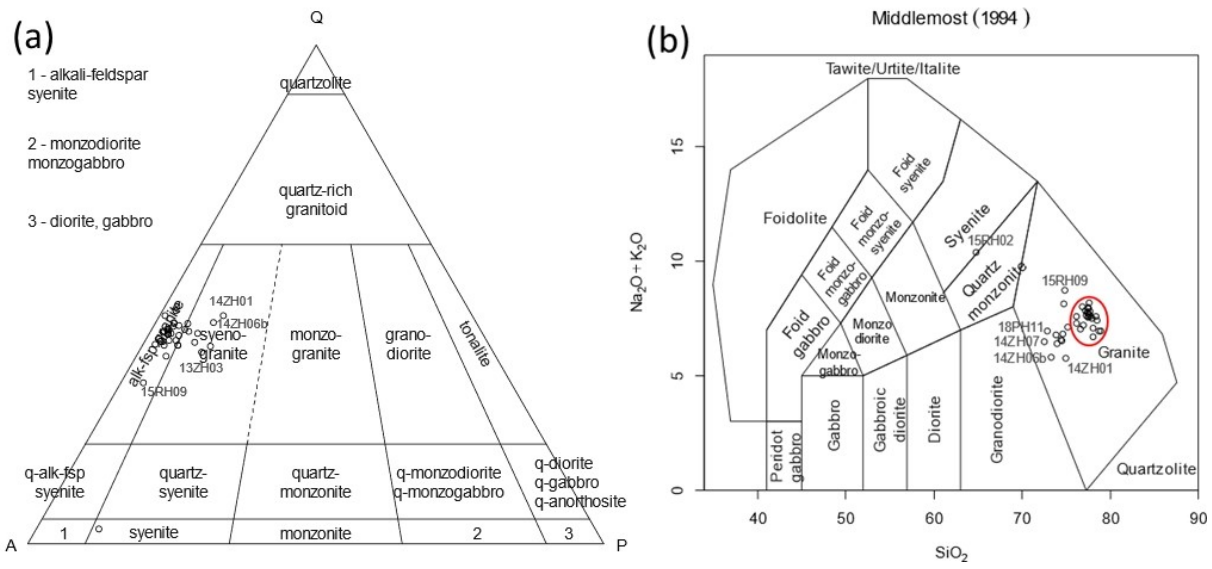

Figure 21: (a) Streckeisen diagram calculated with CIPW norm, (b) TAS diagram (Middlemost, 1994) of all samples measured with XRF

Figure 21 shows the normative classification of all 38 measured samples, following the TAS classification all of them except 15RH02 are granites. The cluster in the granite field marked with the red ellipse represents the aplitic granite samples. See chapter 5.1 for a discussion of the streckeisen diagram.

The aplites (Figure 23) show SiO_2 contents of 73-77%, below 1% CaO and 4-6% K_2O. The gneisses are lower in SiO_2 (mainly 70-73%, up to 77%) distinctly higher in CaO (1-3%) and lower in K_2O (3-4%).

The samples show differentiation trends for Ti, Al, Mg, Mn, Ca, P, Fe and K with rising SiO_2 content from the orthogneisses to the aplitic granite (Figures 23 and 25, the latter with samples from other sites for comparison). K shows a positive correlation, whereas all other elements show a pronounced negative correlation. For Na, no trend can be observed, and for Mn a negative correlation is likely. Amongst the trace elements (Cu, Ce, Nb, Zr, Y, Sr, Rb, Th, Pb, Ga, Zn, Ni, Co, V, La, Ba, Sc, Cr, Cs, Hf and Nd were measured) only V, Y, Zn and Zr showed a correlation with the SiO_2 content (Figure 22). Except for Y, all correlations are negative.

The data are similar to the data of the Felbertal scheelite deposit, but there are major differences to the Alpeinerscharte Mo deposit. This is particularly evident in the spider diagram (Figure 26), where the highest similarity of the Richterspitz data exists with the light colored K1-K3 gneisses and the aplites of the Felbertal deposit. However, both are significantly enriched in high field strength elements.

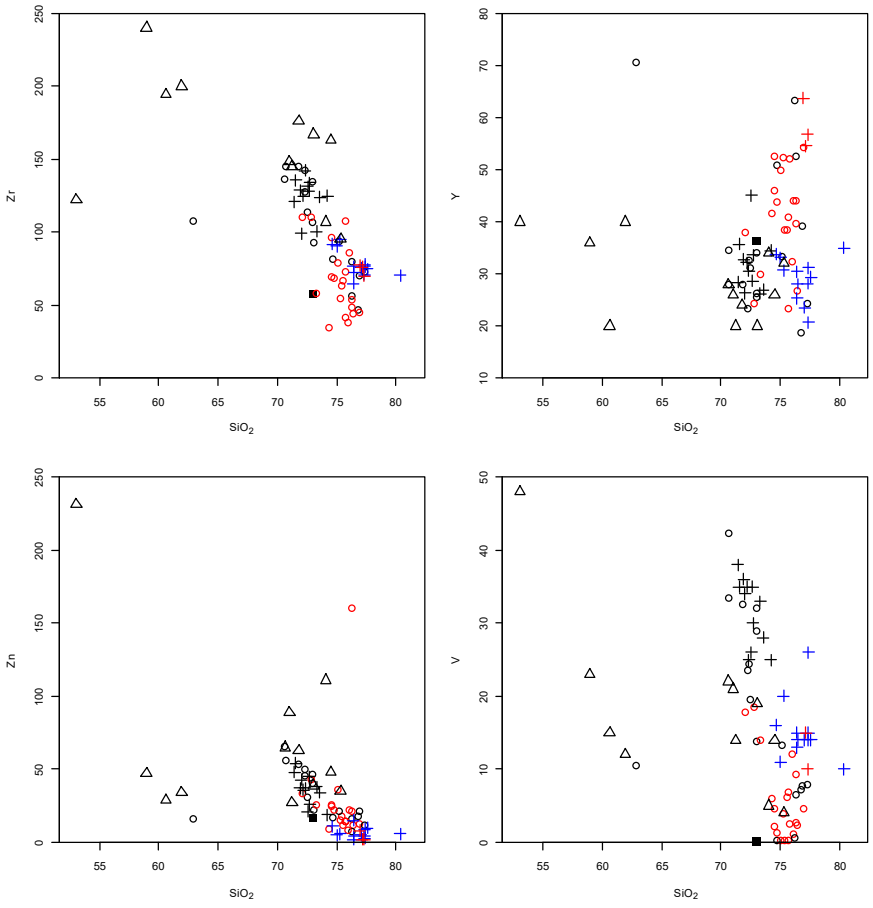

Figure 22: Trace elements showing a differentiation trend with SiO_2. See Figure 24 for symbology.

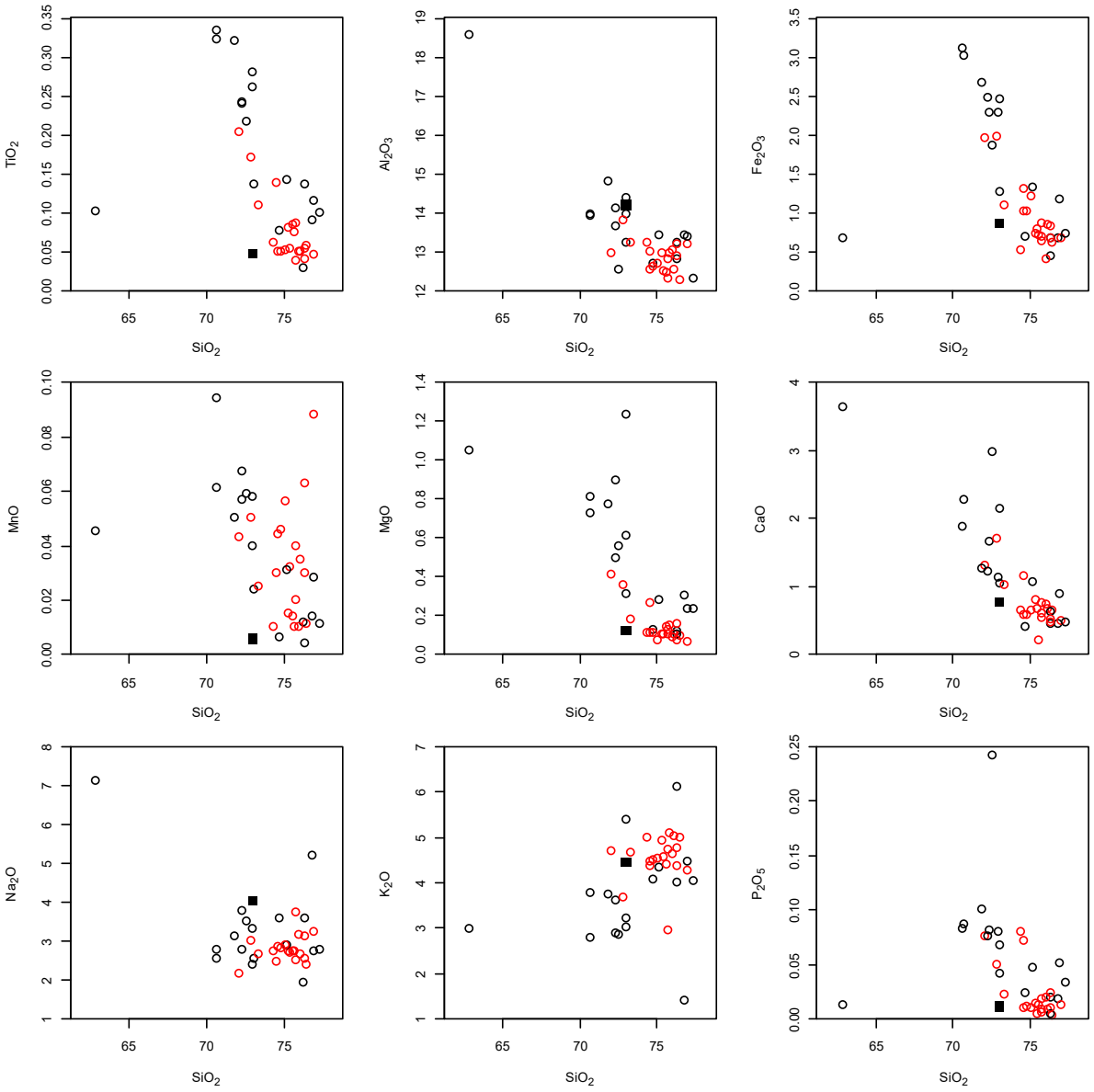

Figure 23: Harker diagrams of all samples of the major elements versus SiO_2. Red circles=aplites, black circles=gneisses, black square=Alpine vein.

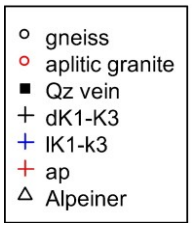

Figure 24: Symbols used in Figures 22 to 26. The first three categories are from this work, "Qz vein"= quartz vein. "dK1-K3" are dark colored K1-K3 gneisses, "lK1-K3" are light colored K1-K3 gneisses and "ap" are aplites, all from the scheelite deposit Felbertal (Kozlik, 2015). "Alpeiner" are samples from the Alpeiner Scharte Mo deposit (Melcher et al., 1996).

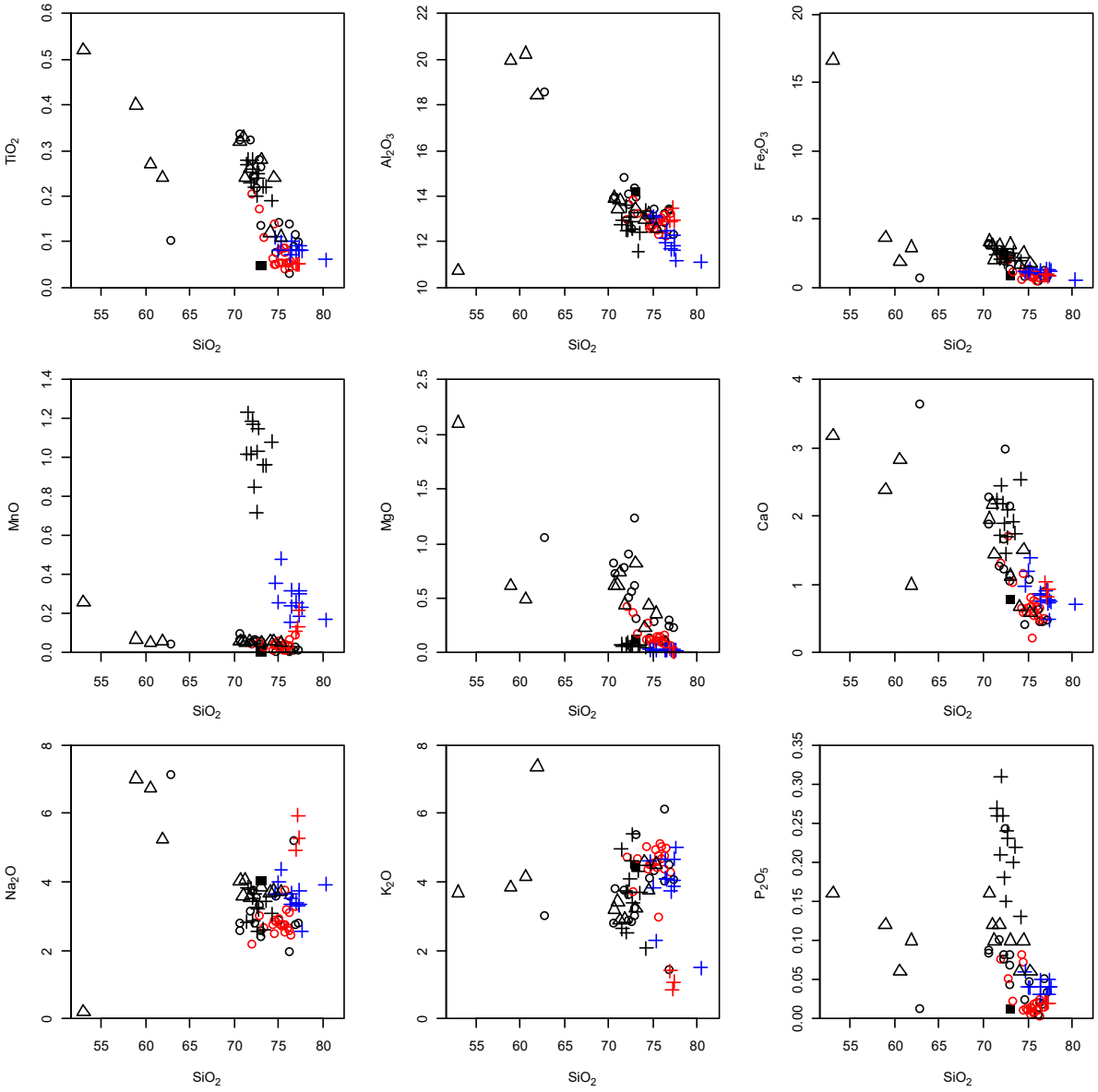

Figure 25: Harker diagrams of all samples and samples from the Alpeiner Scharte (Melcher et al., 1996) and the Felbertal scheelite deposit (Kozlik, 2015) of the major elements versus SiO_2. See Figure 24 for symbology.

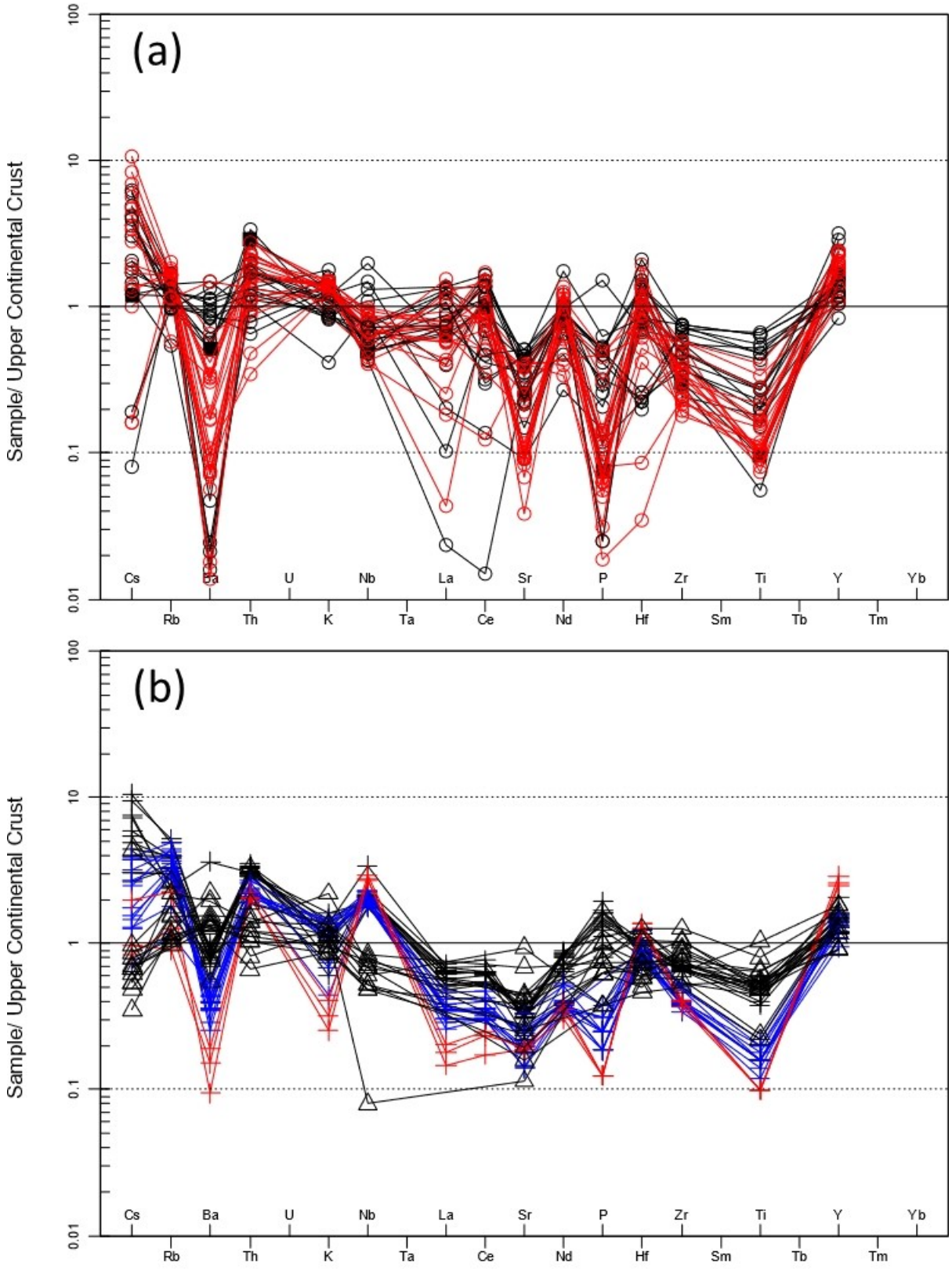

Figure 26: Spider diagrams of the samples (a) and reference samples (b) normalized to upper continental crust (Taylor and McLennan, 1995). See Figure 24 for symbology.

4.5 Mineralogy

All minerals described in this chapter were measured with the EDX detector of the SEM. Hence only the chemical composition and no crystallographic properties could be determined.

4.5.1 Feldspars

As mentioned in the petrography section (chapter 4.1), in most samples the majority of plagioclase is at least medium and often strong or completely saussuritisized. See chapter 5.1.1 for a discussion and an element mapping SEM image (Figure 58a) on that. Figures 6, 10 and 15 show typical appearances of plagioclase. As visible in Figure 27, most feldspars belong to the end members albite or orthoclase and solid solutions are quite rare.

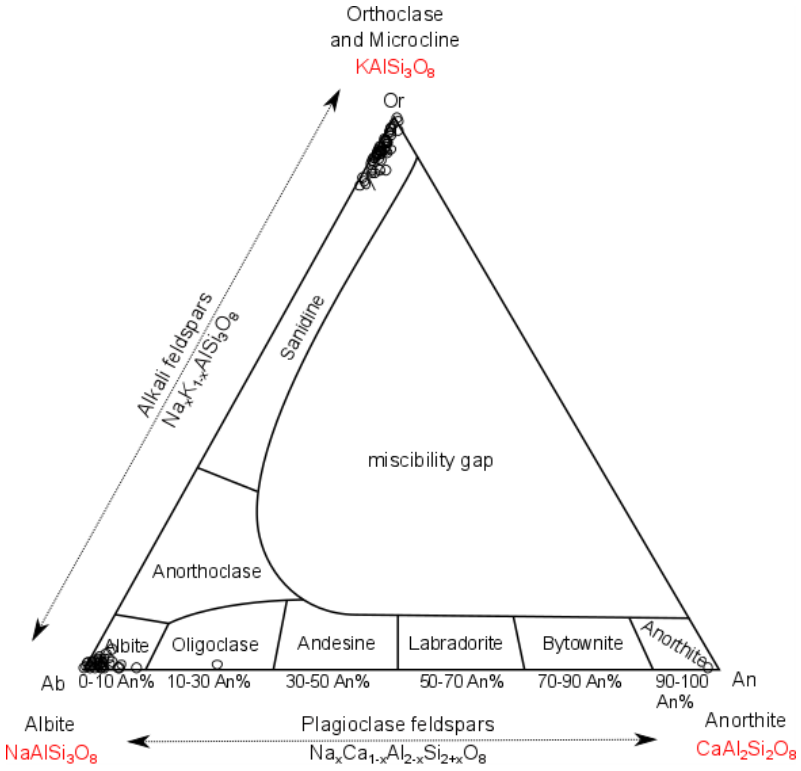

Figure 27: Feldspar composition triangle of 109 spot analyses (circles) with the SEM. Modified from (Muskid, 2018).

4.5.2 Garnet

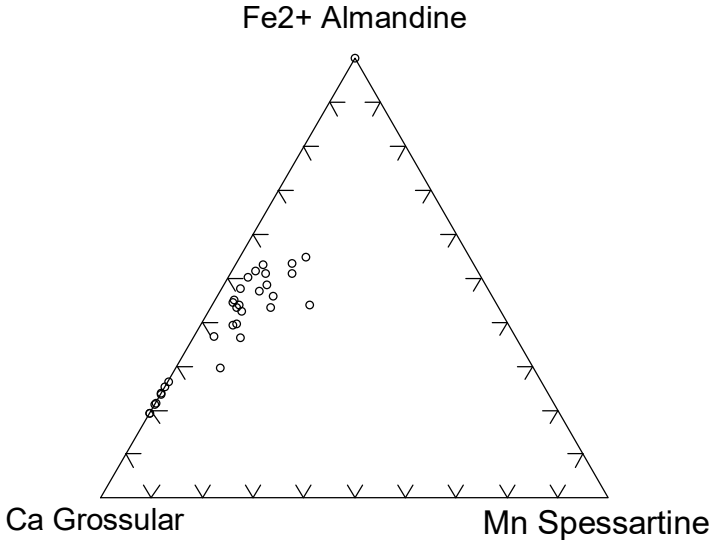

Figure 28: Ternary diagram of garnet compositions.

Garnet is present in the aplitic granites and the gneisses in various frequencies. In the mafic dykes and the alpine veins, no garnet was observed. From 32 SEM measurements, the chemical composition of the garnet grains was calculated. For this the atomic percent were converted in atoms per formula unit, then the tetrahedral Al substituting Si was removed ($Al_{non\text{-}tetrahedral}$ = Al-3 + Si). After this, the Al content was used to calculate the Fe^{3+} content (Fe^{3+} = 2 - $Al_{non\text{-}tetrahedral}$; Fe^{2+} = Fe - Fe^{3+}). As the Fe^{3+} content equivalent to the andradite end member is in most cases below 0.25 atoms per formula unit, it was not used for the classification. Plotting the Ca, Fe^{2+} and Mn contents of the garnet grains (Figure 28) yields that they are grossular-almandine solid solutions with a minor component of spessartine.

4.5.3 Silicates

In addition to the other minerals, also muscovite, biotite, titanite and quartz were observed. Muscovite appears as rock-forming mineral and in molybdenite-quartz veins as larger crystals. Biotite is often altered to chlorite, and in the aplitic granites, it frequently contains exsolution lamellae of rutile. In mineralized zones, the rutile lamellae in biotite are more abundant. Quartz appears as rock-forming mineral and as main constituent of quartz veins and contains in both cases micro fluid inclusions. Very rarely, crystals of halite and sylvite could be observed in/on quartz (Figure 29). As the preparation process uses water and 2 µm sized salt crystals would dissolve immediately, it is likely, that they grew after the preparation. Assuming they originate from the sample, it is possible that fluid inclusions were opened during polishing, leading to evaporation of the contained fluid with dissolved salt that spontaneously crystallized halite and sylvite. This is taken as evidence for high salinities in the fluid inclusions.

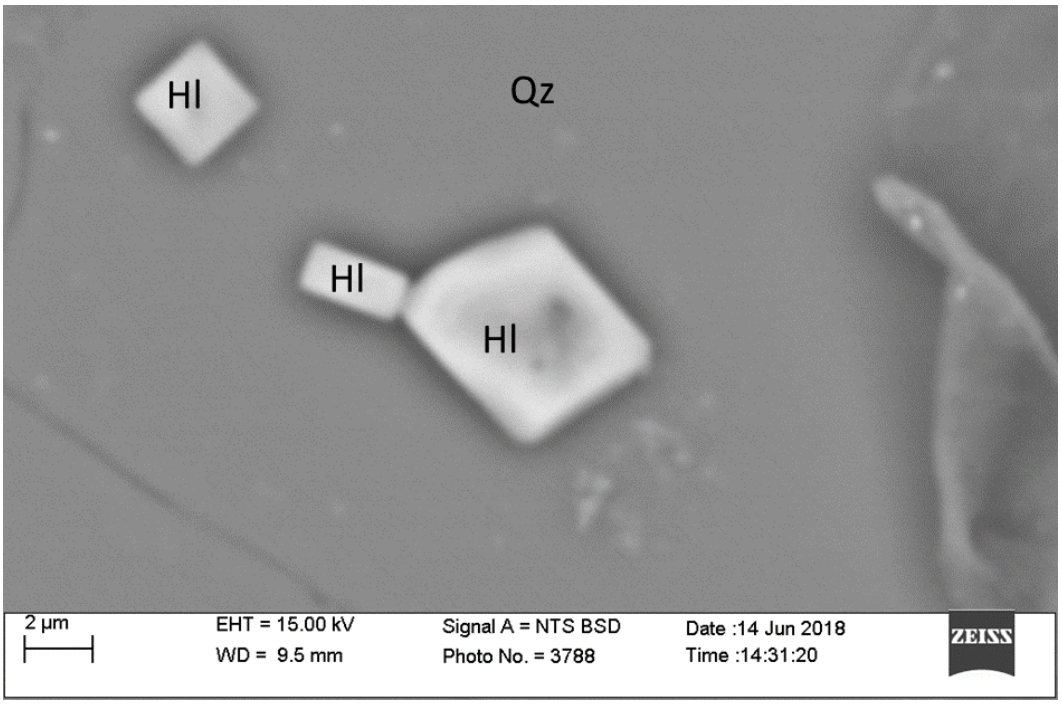

Figure 29: Sample 17RH26, analyses 87-91. Hl=halite, Qz=quartz.

4.5.4 Epidote

Throughout the aplitic granites and less abundant in the gneisses, various members of the epidote family were observed. If occurring together with zircon or U-Th minerals, often REE are incorporated in the epidote grains forming allanite. Y, La, Ce and Nd are the elements which reach the highest concentration with 12.5 atomic percent Y as the highest single value (Table 5).

4.5.5 Zircon

55 zircon grains were analyzed using the SEM (Table 1). Most zircons are isomorphic and frequently occur with U-Th minerals or REE-bearing phases. In rare cases (Figure 57) inclusions can be observed. The Hf contents range from 0 to 0.03 atoms per formula unit.

Sample	Host rock	O	Si	Ca	Zr	Ce	Hf	Th	U
17PH01 22	aplitic granite	4.00	1.01	0.00	0.99	0.00	0.000	0.000	0.000
17PH01_ 46	aplitic granite	4.00	1.03	0.00	0.95	0.00	0.018	0.000	0.000
17PH01_ 56	aplitic granite	3.98	0.98	0.05	0.89	0.02	0.000	0.070	0.013
17PH01_ 57	aplitic granite	4.00	1.00	0.01	0.99	0.00	0.000	0.000	0.005
17PH01_ 64	aplitic granite	4.00	1.02	0.00	0.97	0.00	0.014	0.000	0.000
17PH09	aplitic granite	4.00	0.99	0.00	0.99	0.00	0.020	0.000	0.000
17PH09	aplitic granite	4.00	0.98	0.00	1.01	0.00	0.008	0.000	0.005
17PH09	aplitic granite	4.00	1.01	0.00	0.98	0.00	0.012	0.000	0.000
17PH09	aplitic granite	4.00	1.00	0.00	0.98	0.00	0.012	0.001	0.000
17RH18 128	aplitic granite	4.00	0.98	0.00	1.01	0.00	0.009	0.000	0.000
17RH18 136	aplitic granite	4.00	0.96	0.00	1.03	0.00	0.005	0.000	0.000
17RH26	aplitic granite	4.00	0.99	0.00	1.00	0.00	0.014	0.000	0.000
17RH26	aplitic granite	4.00	0.96	0.00	1.04	0.00	0.000	0.000	0.000
17RH26	aplitic granite	4.00	1.00	0.00	0.98	0.00	0.019	0.000	0.000
17RH26	aplitic granite	4.00	1.05	0.00	0.94	0.00	0.015	0.000	0.000

Sample	Host rock	O	Si	Ca	Zr	Ce	Hf	Th	U
17RH26	aplitic granite	3.90	0.97	0.19	0.68	0.00	0.017	0.046	0.005
17RH37 177	aplitic granite	4.00	0.98	0.00	1.01	0.00	0.012	0.000	0.000
17RH37 178	aplitic granite	4.00	0.99	0.00	1.00	0.00	0.009	0.000	0.000
17RH37_ 19	aplitic granite	4.00	1.00	0.00	0.99	0.00	0.012	0.000	0.000
18PH4_ 11	gneiss	4.00	0.88	0.00	1.10	0.00	0.020	0.000	0.000
18PH4_ 14	gneiss	4.00	0.93	0.00	1.04	0.00	0.033	0.000	0.000
18PH4_ 20	gneiss	4.00	0.90	0.00	1.07	0.00	0.026	0.000	0.000
18PH4_ 26	gneiss	4.00	0.92	0.00	1.06	0.00	0.010	0.000	0.000
18PH4_ 31	gneiss	4.00	0.93	0.00	1.05	0.00	0.025	0.000	0.000
18PH4_ 36	gneiss	4.00	0.92	0.00	1.05	0.00	0.028	0.000	0.000
18PH4_ 41	gneiss	4.00	0.91	0.00	1.06	0.00	0.024	0.000	0.000
18PH4_ 42	gneiss	4.00	0.92	0.00	1.07	0.00	0.013	0.000	0.000
18PH4_ 6	gneiss	4.00	0.91	0.00	1.08	0.00	0.009	0.000	0.000
18PH5_ 19	gneiss	4.00	0.98	0.00	1.02	0.00	0.003	0.000	0.000
18PH5_ 20	gneiss	4.00	0.99	0.00	1.00	0.00	0.006	0.000	0.000
18PH5_ 21	gneiss	4.00	1.00	0.00	0.98	0.00	0.017	0.000	0.000
18PH5_ 26	gneiss	4.00	0.99	0.00	1.01	0.00	0.003	0.000	0.000
18PH5_ 49	gneiss	4.00	0.99	0.00	1.00	0.00	0.013	0.000	0.000
18PH5_ 57	gneiss	4.00	0.97	0.00	1.01	0.00	0.014	0.000	0.000
18PH5_ 64	gneiss	4.00	1.01	0.00	0.98	0.00	0.018	0.000	0.000
18ZT2_ 12	aplitic granite	4.00	0.98	0.00	0.99	0.00	0.025	0.000	0.000
18ZT2_ 16	aplitic granite	4.00	0.97	0.00	1.00	0.00	0.02	0.000	0.000
18ZT2_ 47	aplitic granite	4.00	0.91	0.00	1.06	0.00	0.02	0.000	0.000
18ZT2_ 49	aplitic granite	4.00	0.95	0.00	1.03	0.00	0.03	0.000	0.000
18ZT2_ 6	aplitic granite	4.00	0.97	0.00	0.99	0.00	0.04	0.000	0.000
18ZT2_ 69	aplitic granite	3.98	0.91	0.00	1.05	0.00	0.01	0.000	0.000
18ZT2_ 73	aplitic granite	4.00	0.94	0.00	1.04	0.00	0.02	0.000	0.000
18ZT2_ 8	aplitic granite	4.00	0.98	0.00	1.01	0.00	0.02	0.000	0.000
FM089	gneiss	4.00	0.98	0.00	0.99	0.00	0.03	0.001	0.001
FM089	gneiss	4.00	0.97	0.00	1.03	0.00	0.00	0.000	0.000
FM089	gneiss	4.00	0.97	0.00	1.03	0.00	0.00	0.000	0.000
FM089	gneiss	4.00	0.98	0.00	1.02	0.00	0.00	0.000	0.000
FM099 220	aplitic granite	4.00	0.99	0.00	0.98	0.00	0.02	0.000	0.000
FM099 221	aplitic granite	4.00	1.00	0.00	0.99	0.00	0.02	0.000	0.000
FM099_ 32	aplitic granite	4.00	0.99	0.00	0.97	0.00	0.05	0.000	0.000
FM099_ 33	aplitic granite	4.00	0.96	0.00	1.02	0.00	0.03	0.000	0.000
FM100 177	gneiss	4.00	0.99	0.00	1.01	0.00	0.01	0.000	0.000
FM089	gneiss	4.00	0.99	0.00	1.00	0.00	0.01	0.001	0.000
FM089	gneiss	4.00	0.97	0.00	0.99	0.00	0.03	0.007	0.001
FM100 24	gneiss	4.00	0.97	0.00	1.03	0.00	0.00	0.000	0.000

Table 1: Zircon analyses from the SEM, all numbers are atoms per formula unit.

4.5.6 Apatite

Apatites were observed in several aplitic granite samples and usually contain about 3-4 atomic percent F. In their vicinity REE-bearing phosphates such as xenotime, monazite and brabantite are frequently observed.

4.5.7 Carbonates

Calcite is a widespread, but rare alteration mineral in many samples and appears as pervasive alteration and replaces other grains (Figure 30).

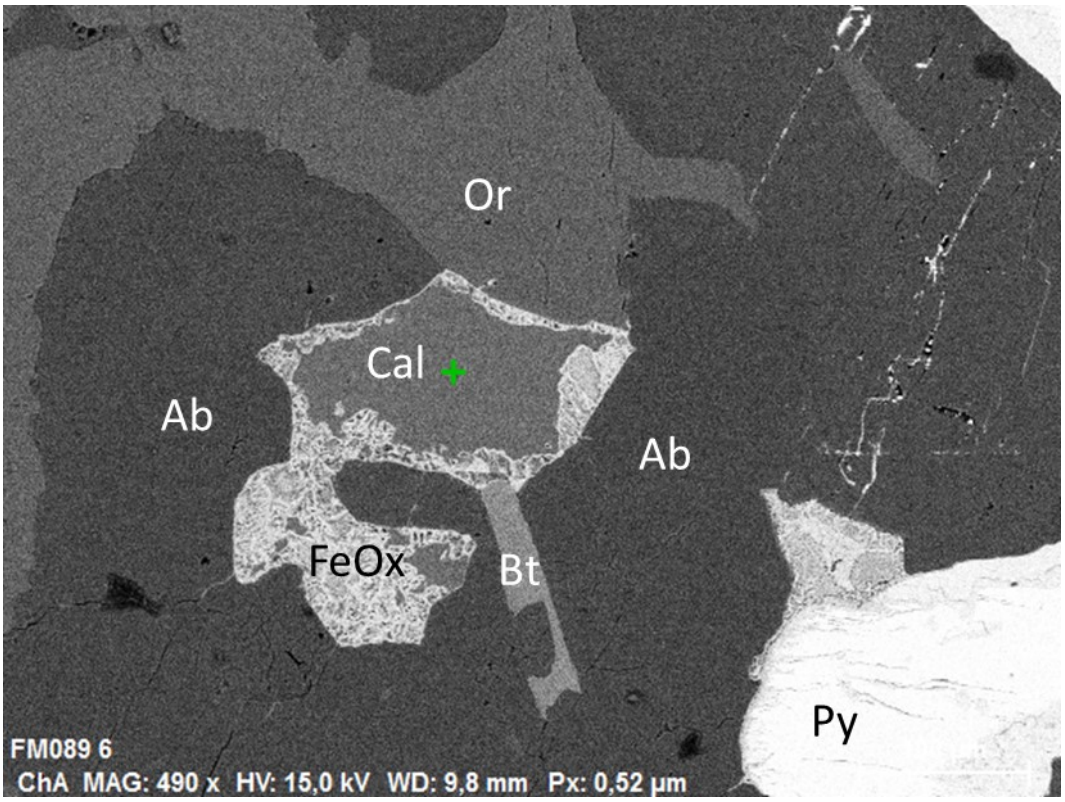

Figure 30: Sample 15RH05, analyses 1-6. Ab=albite, Bt=biotite, Cal=calcite, Or=orthoclase, Py=pyrite, FeOx=iron oxides

4.5.8 Oxides

As many samples have a rusty appearance in the field, this is also observable in thin sections. Primary Fe minerals are hematite, ilmenite and magnetite; they are often altered to various Fe oxides. The latter could not be determined accurately with the SEM. Therefore, they are pointed out as FeOx. The FeOx are often associated with molybdenite and form pseudomorphs after their predecessor minerals (Figure 34) as well as crack fillings (Figure 33). Figure 30 shows calcite with an alteration of FeOx. This is an alteration and no weathering, as weathering would dissolve calcite rather than precipitating Fe oxides. This was only observed near sulfides although calcite is distributed equally on this thin section. As the oxidation also affected galena, a Pb oxide or carbonate species was found.

In the gneiss sample 15RH05, an unusual large aggregate of pyrrhotite (Figure 31) with a cavity filled with Cr-Ni-magnetite was found. Cr contents are 6-7 atomic percent, Ni contents range from 3-4 atomic percent while the Fe content is about 33 atomic percent (Figure 32). The crystals seem to be of hydrothermal origin as they are in a cavity. The Ni source is probably pentlandite previously coexisting with the pyrrhotite. For the Cr source, only speculations are possible: 15RH05 is a loose block found in a moraine, it is possible that it was initially located near to a mafic dyke which may have served as a source for Cr.

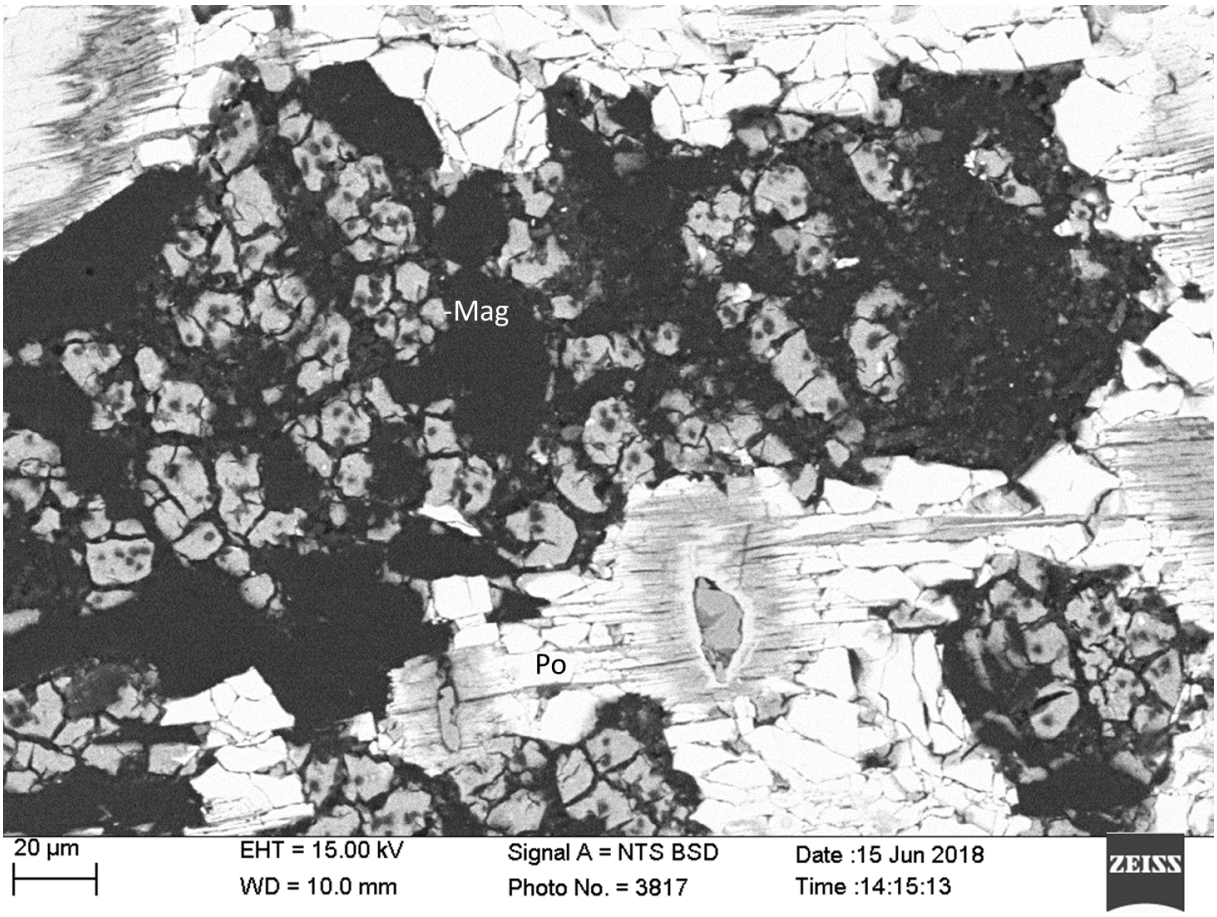

Figure 31: Sample 15RH05, analyses 29-31, the Mag is a Cr-Ni-magnetite. Mag=magnetite, Po=pyrrhotite.

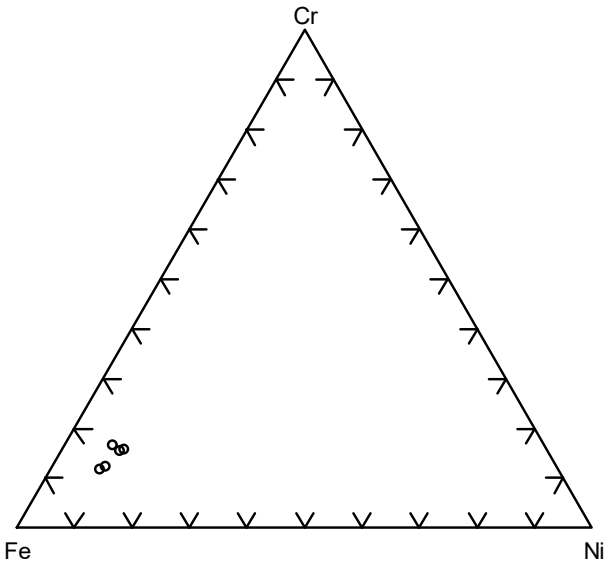

Figure 32: Atomic composition diagram of the measured Cr-Ni-magnetites, sample 15RH05.

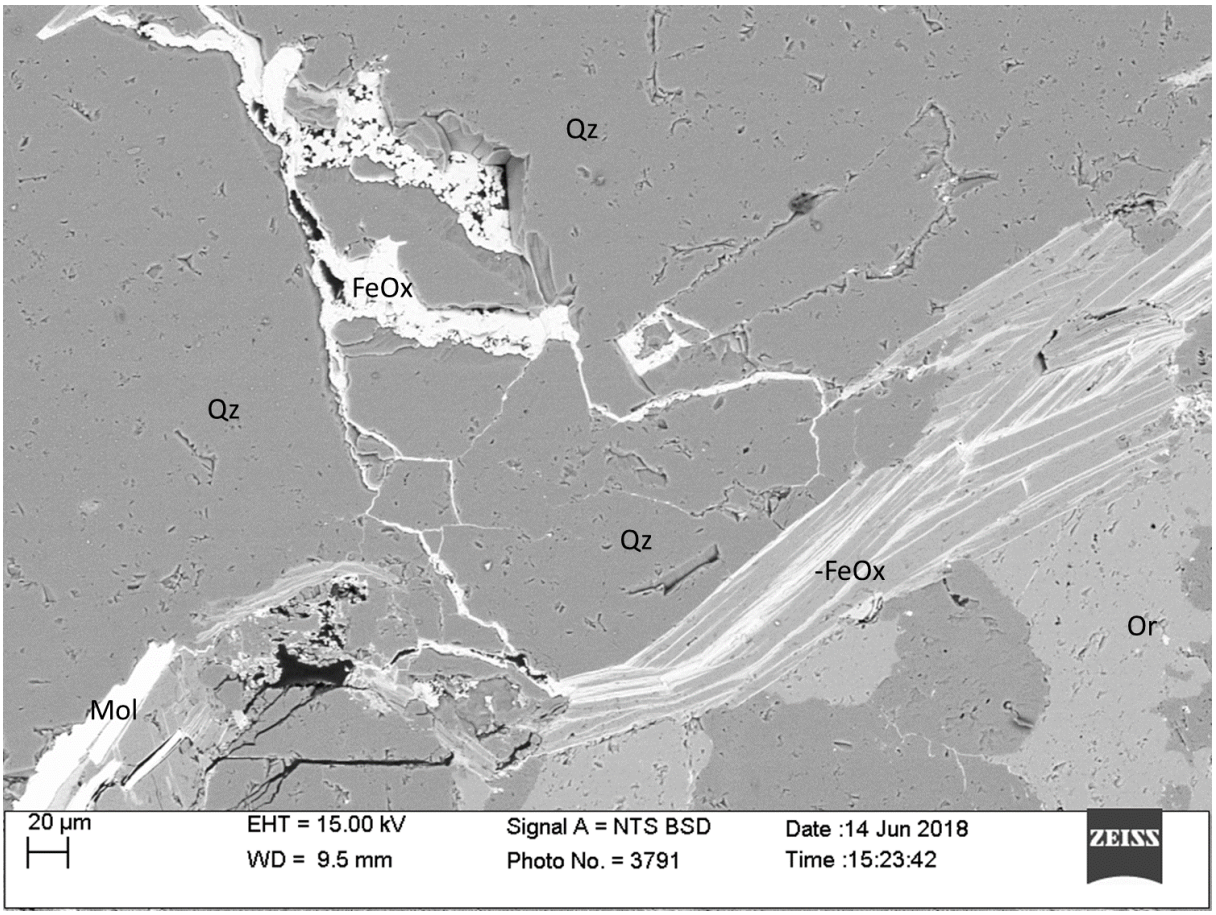

Figure 33: Sample 17RH18, analyses 98-101. Or=orthoclase, Qz=quartz.

4.5.9 Sulfides

Although the major part of the mineralization is molybdenite, there are also other sulfides present and associated with it. In order of frequency: pyrite, chalcopyrite, pyrrhotite (Fe_7S_8), galena and sphalerite. Pyrite also occurs solely. All of them but especially pyrite are often oxidized at the rims (Figure 34b) or pervasive (Figure 34a).

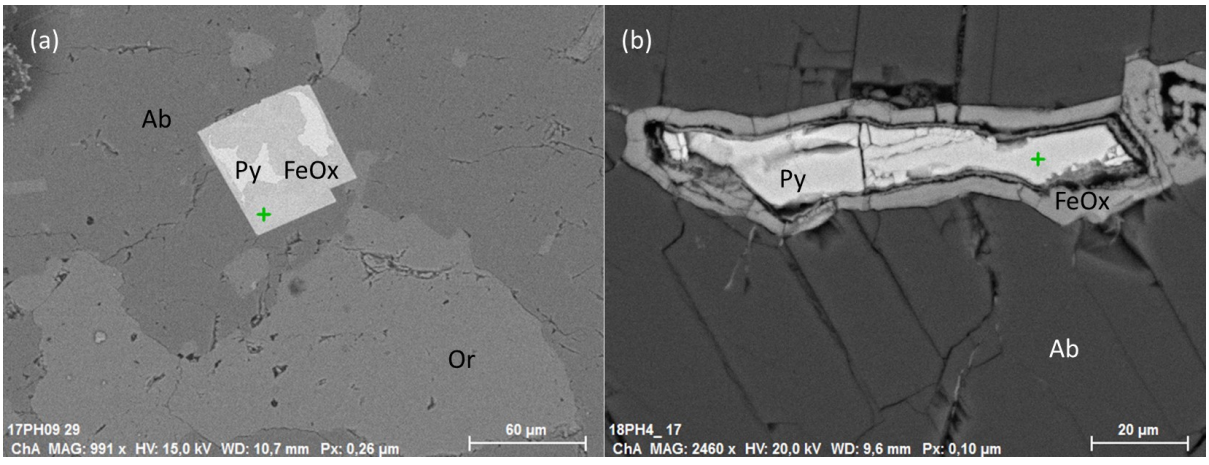

Figure 34: (a) sample 17PH09, analyses 7-9; (b) sample 18PH4, analyses 17-18. Ab=albite, Py=Pyrite.

4.5.10 Molybdenite

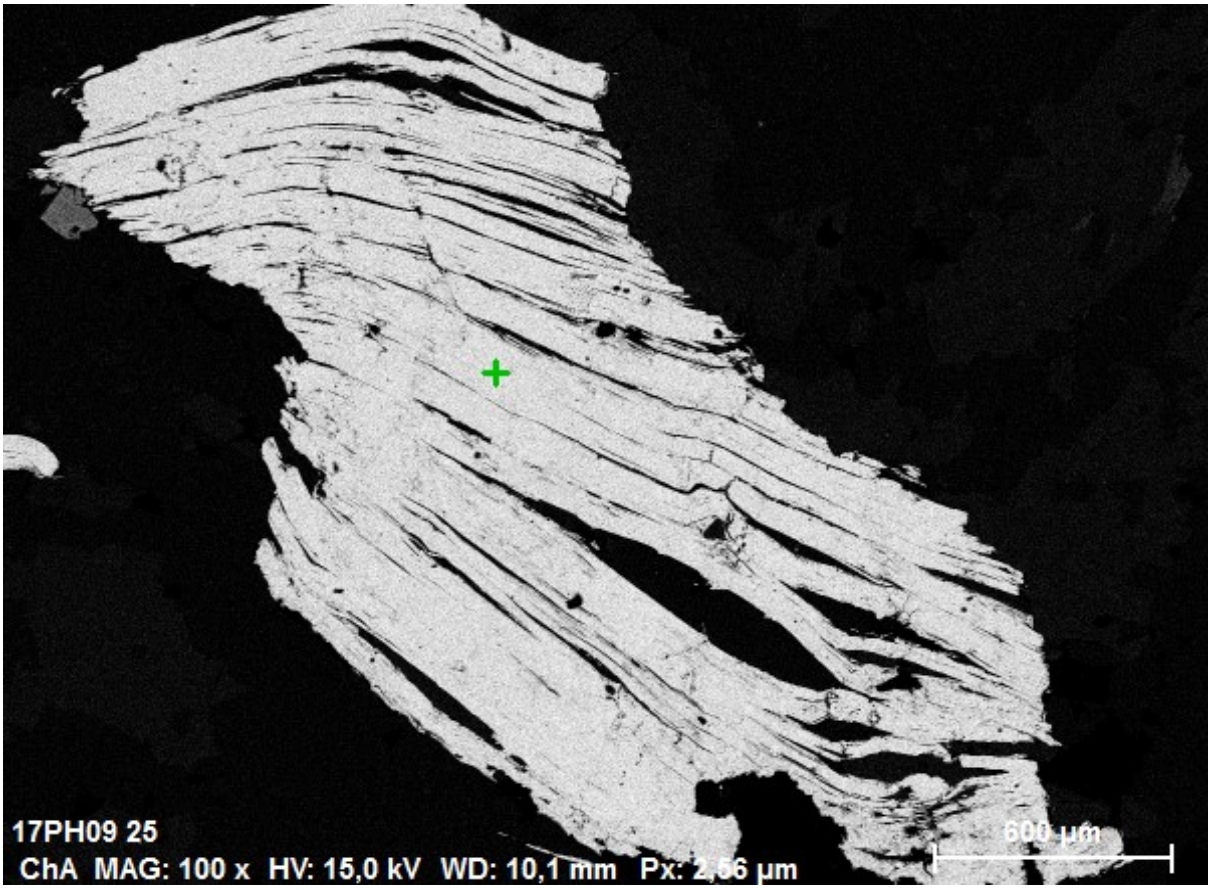

Figure 35: Molybdenite in sample 17PH09.

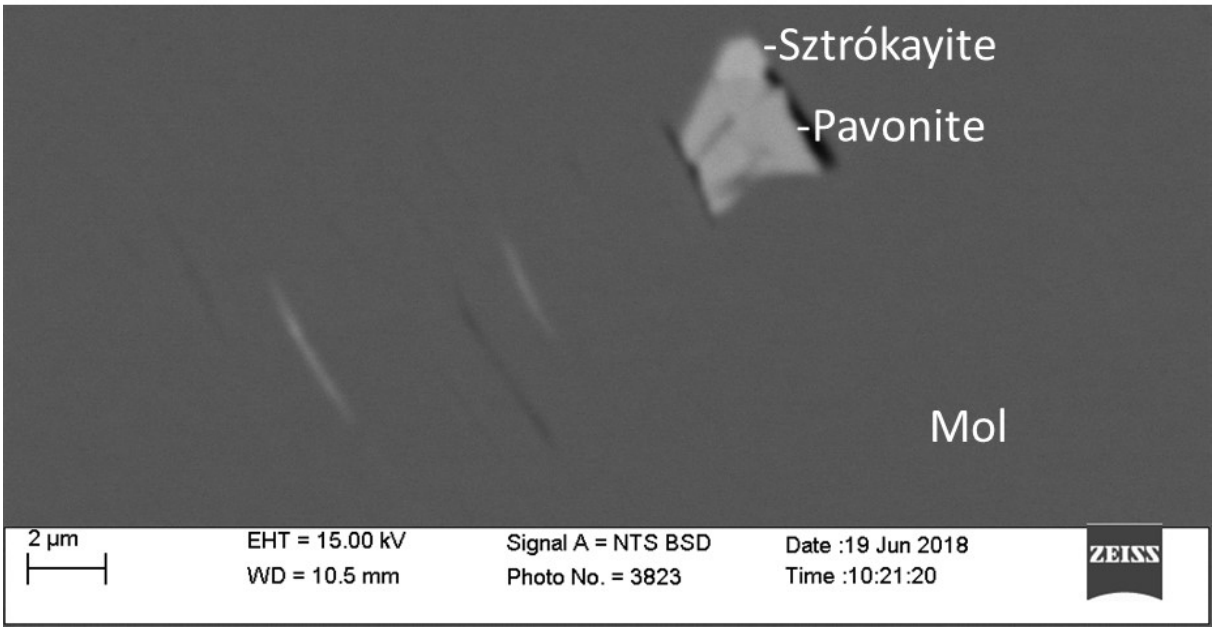

Figure 36: SEM image of Mol in sample 15RH05.

Molybdenite appears as platy, often deformed aggregates with no internal structure (Figures 15, 16 and 35) except the undulous anisotropy colors under X N and the strongly developed cleavage. This is also mainly true in chemical terms (Figure 36). Most molybdenite aggregates

consist over large homogeneous areas of pure molybdenite with sporadic cracks following the cleavage plains, very rarely there are small blebs of native Bi or Bi alloys.

4.5.11 Bismuth phases

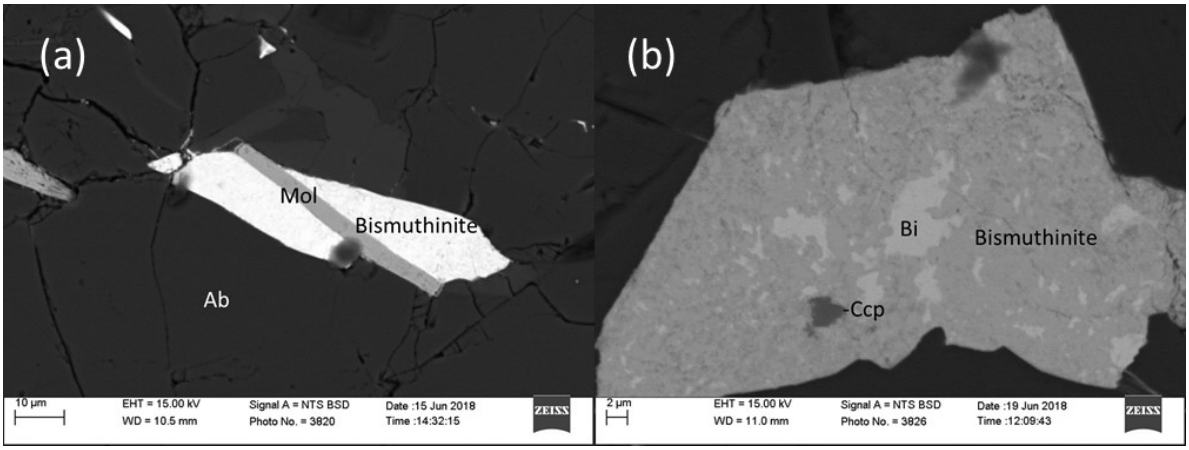

Figure 37: (a) Sample 15RH05, analyses 216-219; (b) S Sample 15RH05, analyses 23-25.

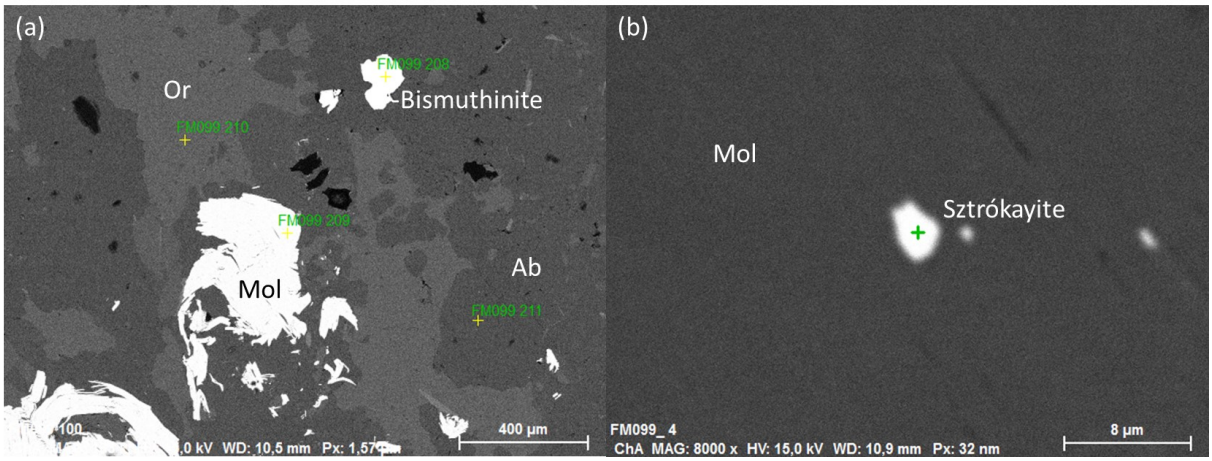

Figure 38: Sample 15RH05; a: analyses 208-211, b: analysis 4. Ab= albite, Mol = molybdenite, Or = orthoclase.

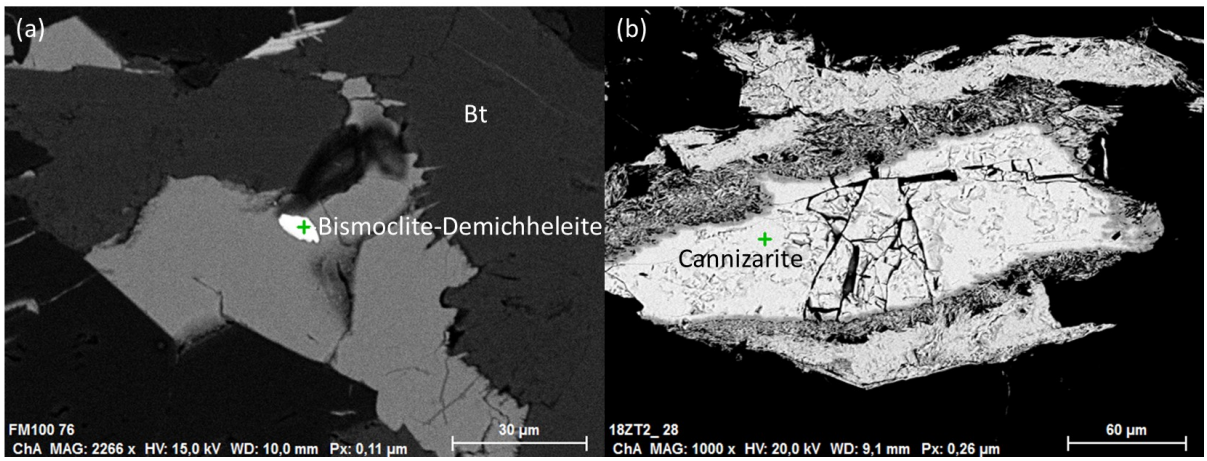

Figure 39: (a) Sample 15RH20, analysis 22, (b) sample 18ZT2 analysis 36. Bt=biotite.

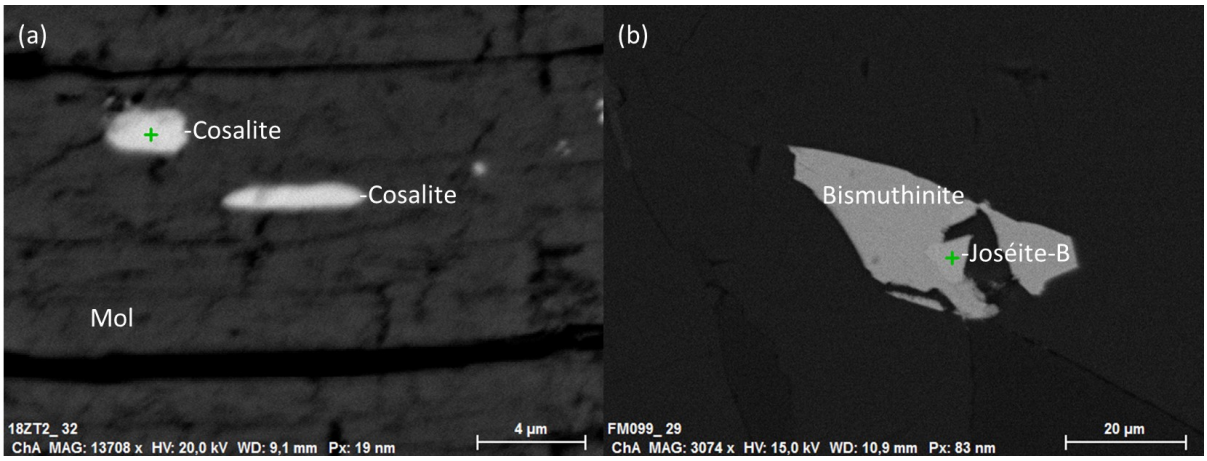

Figure 40: (a) Sample 18ZT2, analyses 40, 41; (b) sample 15RH05, analyses 26, 27.

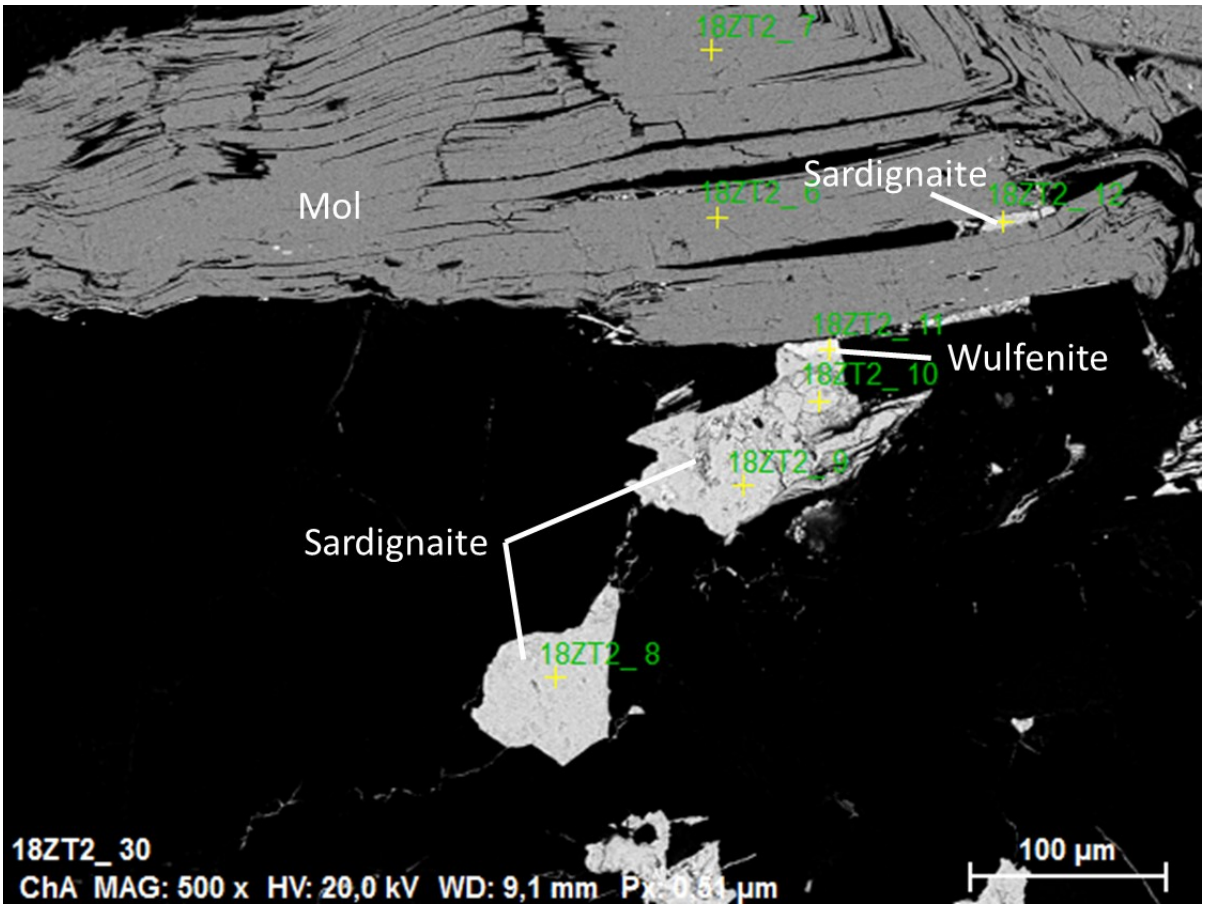

Figure 41: Sample 18ZT2, analyses 6-12. Mol=molybdenite.

Bi-Minerals are present in several thin sections. They occur completely enclosed in molybdenite and as free grains, but always near to molybdenite or other sulfides. Most frequent are bismuthinite (Bi_2S_3) and native bismuth. Bismuthinite (Figure 38a) yielded about 40 atomic percent Bi and 60 atomic percent S. Table 2 shows the results of the analyses of Bi-containing minerals.

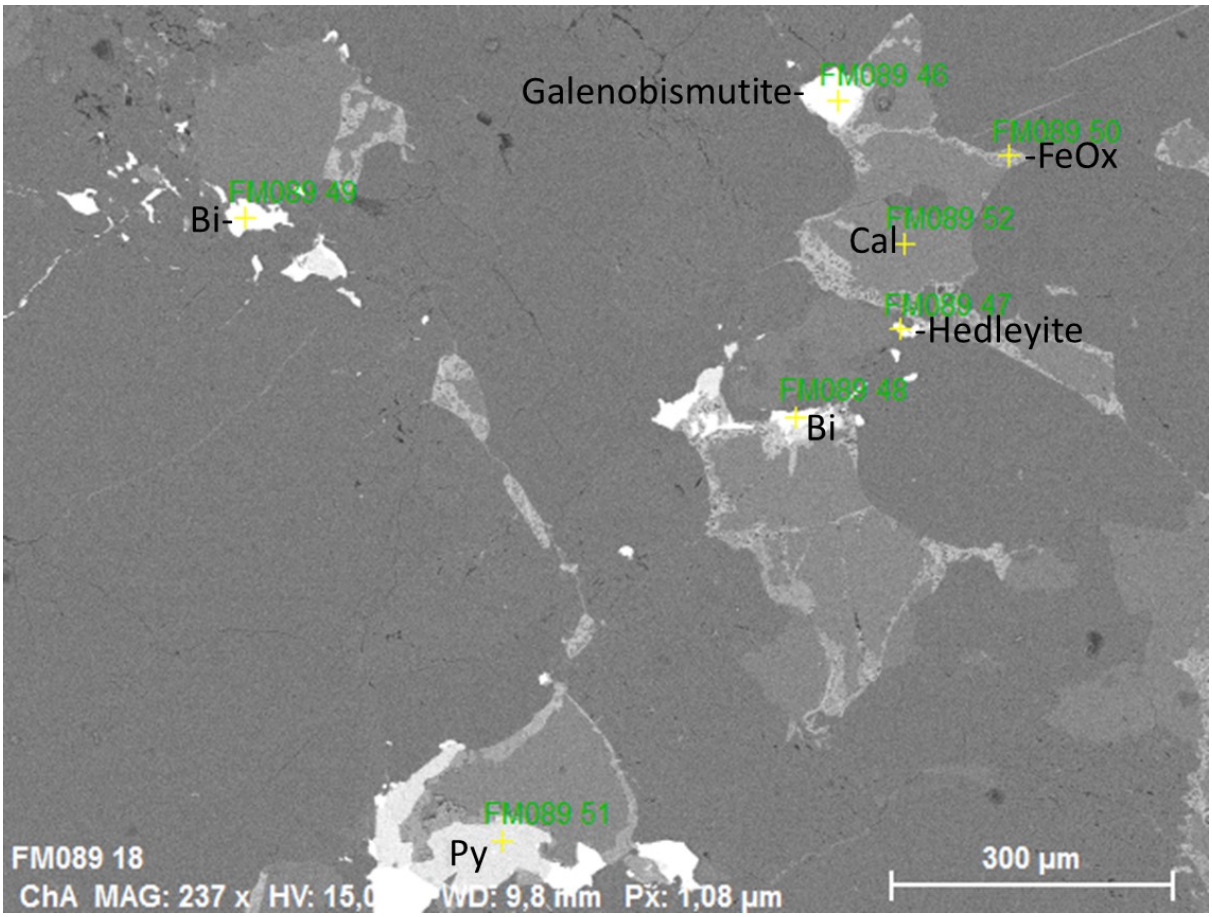

Figure 42: Sample 15RH05, analyses 46-52.

Bismuth tellurides are frequent amongst Bi containing minerals: A mineral similar to sztrókayite (Bi_3TeS_2, Figure 38b) yielded 45 atomic percent Bi, 17 atomic percent Te and 32 atomic percent S, which fits well with Bi_3TeS_2. This mineral was only found as inclusions in molybdenite, often associated with other Bi minerals. Similar are joséite-B (Bi_4Te_2S, 50 atomic percent Bi, 30 atomic percent Te, 10 atomic percent S) and hedleyite (Bi_7Te_3, 65 atomic percent Bi, 35 atomic percent Te), both are not exactly stoichiometric, but best fits.

Bismuth oxide phases (Figure 50) were frequently encountered and yielded 30-60% O in the analysis. As there is no exact calibration for O in such minerals available at the used SEM, it can be assumed, that at least some of them are bismite (Bi_2O_3) grains. However, they are clearly alteration phases.

Analysis FM100 22 (Figure 39a) yielded a chemical composition between bismoclite (BiOCl) and demicheleite (BiSCl). However, it is questionable how much O is really in the mineral.

A variety of Pb-Bi-S minerals was found, they were interpreted as cannizarite ($Pb_8Bi_{10}S_{23}$, Figure 39b), cosalite ($Pb_2Bi_2S_5$, Figure 40a) and galenobismutite ($PbBi_2S_4$, Figure 42) as best

fits. As the differences between cannizzarite and cosalite minerals are comparatively small, it can only be concluded, that at least one of them probably exists in the thin sections.

As the only observed sulfosalt and Ag bearing phase, probably pavonite ($AgBi_3S_5$, 30 atomic percent Bi, 5 atomic percent Ag and 65 atomic percent S, Figure 36) was found.

Molybdenum-containing Bi minerals, namely probably cannizzarite, koechlinite, sardignaite and suseinargiuite are described in chapter 4.5.13.

Interestingly, native Bi seems often to be a relict core (Figure 37b) but also forms complete crack fillings (Figure 43). This points to a multiphase evolution of the mineralization, but also to spatial differences within the mineralization. Inside molybdenite, only bismuthinite, Sztrókayite, cosalite and native Bi occur and are mostly pure (Figures 37a and 40a).

Outside molybdenite, complex intergrowths dominate (Figures 37b and 50). The assemblage in Figure 50 is of particular interest because it is the only occurrence of lillianite ($Pb_3Bi_2S_6$) and acanthite (Ag_2S) in the working area. In the direct surroundings (1 cm) of this complex are large molybdenite plates, accompanied by pyrite and chalcopyrite in the thin section.

Possible Mineral	Spektrum	Figure	O	Na	Al	Si	S	Cl	Fe	As	Mo	Ag	Te	Re	Pb	Bi
Bismuth	FM089	Figure 43	7.79	-	-	-	-	-	-	-	-	-	-	-	-	92.21
Bismuth	FM089		10.96	-	-	-	-	-	-	-	-	-	-	-	-	89.04
Bismuth	FM089		31.37	-	-	-	-	-	-	-	-	-	-	-	-	68.63
Bismuth	FM089		5.95	-	-	8.37	-	-	-	-	-	-	-	-	-	85.68
Bismuth	FM089		6.76	-	-	-	-	-	-	-	-	-	0.93	-	-	92.31
Bismuth	FM089		38.01	-	-	-	-	-	-	-	-	-	0.09	-	-	61.90
Bismuth	FM089		19.84	-	-	-	-	-	-	-	-	-	0.00	-	-	80.16
Bismuth	FM089		10.44	-	-	-	-	-	-	-	-	-	-	-	-	89.56
Bismuth	FM089		12.39	-	-	-	-	-	-	-	-	-	-	-	-	87.61
Bismuth	FM089		10.17	-	-	-	-	-	-	-	-	-	-	-	-	89.83
Bismuth	FM089		18.18	-	-	-	-	-	-	-	-	-	0.00	-	-	81.82
Bismuth	FM089		8.06	-	-	-	-	-	-	-	-	-	-	-	-	91.94
Bismuth	FM089		7.76	-	-	-	-	-	-	-	-	-	-	-	-	92.24
Bismuth	FM099_ 12		9.84				0.00				0.00		0.00			90.16
Bismuth	FM099_ 15		24.84									0.00	0.47			74.69
Bismuth	FM099_ 18		12.09				5.37					0.00	0.00			82.54
Bismuth	FM099_ 21		13.48				0.00						0.36			86.16
Bismuth	FM099_ 23		9.90				0.00									90.10
Bismite?	FM099 27		59.08	4.68	2.52	5.14	7.67									20.59
Bismite?	18ZT2_ 62		61.17			5.84										32.99
Bismite?	18ZT2_ 25	Figure 50	32.86				0.35						2.98			63.81
Bismite?	18ZT2_ 29		34.58				0.44				0.00	0.00	0.00			64.97
Bismite?	18ZT2_ 38		39.23				0.21					2.15			1.74	56.67
Bismite?	FM089		49.43	-	-	-	-	-	-	-	-	-	-	-	-	50.57
Bismite?	FM089		48.32	-	-	-	-	-	6.15	-	-	-	-	-	-	45.49
Bismite?	FM099_ 13		52.55				9.29						0.00			38.16
Bismoclite-Demicheleite	FM100 22	Figure 39a	18.39				9.61	30.18	13.68		0.00				0.00	28.14
Bismuthinite	FM099 33		4.27				66.30				5.35		2.87			21.21
Bismuthinite	18ZT2_ 23	Figure 37b					63.54				3.56			5.73		27.17
Bismuthinite	FM099 2		20.03				46.34					0.00	0.00			33.62
Bismuthinite	FM099 208	Figure 38a	3.54				57.07									39.39
Bismuthinite	FM099 212		4.55				58.35				0.00					37.10
Bismuthinite	FM099 217	Figure 37a	31.06				36.15									32.79
Bismuthinite	FM099 218	Figure 37a	27.88				38.92									33.19

Possible Mineral	Spektrum	Figure	O	Na	Al	Si	S	Cl	Fe	As	Mo	Ag	Te	Re	Pb	Bi
Bismuthinite	FM099 3		22.40				42.54				0.00		0.00			35.06
Bismuthinite	FM099 4		41.13				28.77				0.00		0.04			30.06
Bismuthinite	FM099_ 1		4.46				57.34				0.00		0.25			37.96
Bismuthinite	FM099_ 11		5.78				57.72				0.00		0.00			36.50
Bismuthinite	FM099_ 14						56.14				0.00	7.32	0.00	0.92		35.61
Bismuthinite	FM099_ 16		4.67				57.43					0.00	0.00			37.91
Bismuthinite	FM099_ 17		12.85				48.34					0.00	0.43			38.38
Bismuthinite	FM099_ 19		3.80				57.66					0.34	0.00			38.19
Bismuthinite	FM099_ 20		24.09				40.66						0.15			35.10
Bismuthinite	FM099_ 22		17.40				45.22						0.00			37.39
Bismuthinite	FM099_ 25		12.76				50.28						0.00			36.96
Bismuthinite	FM099_ 27	Figure 40b	5.80				57.26						0.00			36.94
Bismuthinite	FM099_ 7						61.27				3.78	0.00	2.67	0.00		32.27
Cannizarite	18ZT2_ 36	Figure 39b	5.66				50.69					2.96			17.01	23.67
Cannizarite	18ZT2_ 40		9.95				45.66				18.03	2.16			10.19	14.02
Cosalite	18ZT2_ 41	Figure 40a	8.82				55.40					2.68			16.92	16.18
Galenobismutite	FM089	Figure 42	46	0	2.04	-	53.01	-	-	-	-	-	-	-	16.62	28.32
Galenobismutite	FM089	Figure 42	46	0	2.04	-	53.01	-	-	-	-	-	-	-	16.62	28.32
Hedleyite	FM089	Figure 42	-	-	-	-	-	-	-	-	-	-	35.07	-	-	64.93
Joséite-B	FM099_ 26	Figure 40b	10.55				9.24						29.14			51.07
Koechlinite	18ZT2_ 10	Figure 41	59.34								25.12					15.54
Koechlinite	18ZT2_ 8	Figure 41	62.83								24.24					12.64
Koechlinite	18ZT2_ 9	Figure 41	69.71								17.28					12.96
Lillianite	18ZT2_ 26	Figure 50	6.07				51.85					3.38			17.19	21.50
Pavonite?	GR2_ 11 (FM099)	Figure 36					64.18				0.00	5.25	0.00			30.57
Sardignaite	18ZT2_ 12	Figure 41	62.57								23.97					13.43
Suseinargiuite	18ZT2_ 54	Figure 46b	67.53	5.68							16.95	0.92				8.92
Suseinargiuite	18ZT2_ 55	Figure 46b	68.89	4.20							18.31	1.05				7.55
Sztrókayite	FM099_ 4	Figure 38b	6.22				32.16						17.01			44.61
Sztrókayite	GR2_ 12 (FM099)	Figure 36					38.72				0.00	0.82	15.24	0.00		45.22

Table 2: SEM EDX analyses of Bi containing minerals. Note, that the mineral names are only proposed according to the approximate composition without H_2O, CO_2 and only roughly estimated O contents. All numbers are normalized atomic percent.

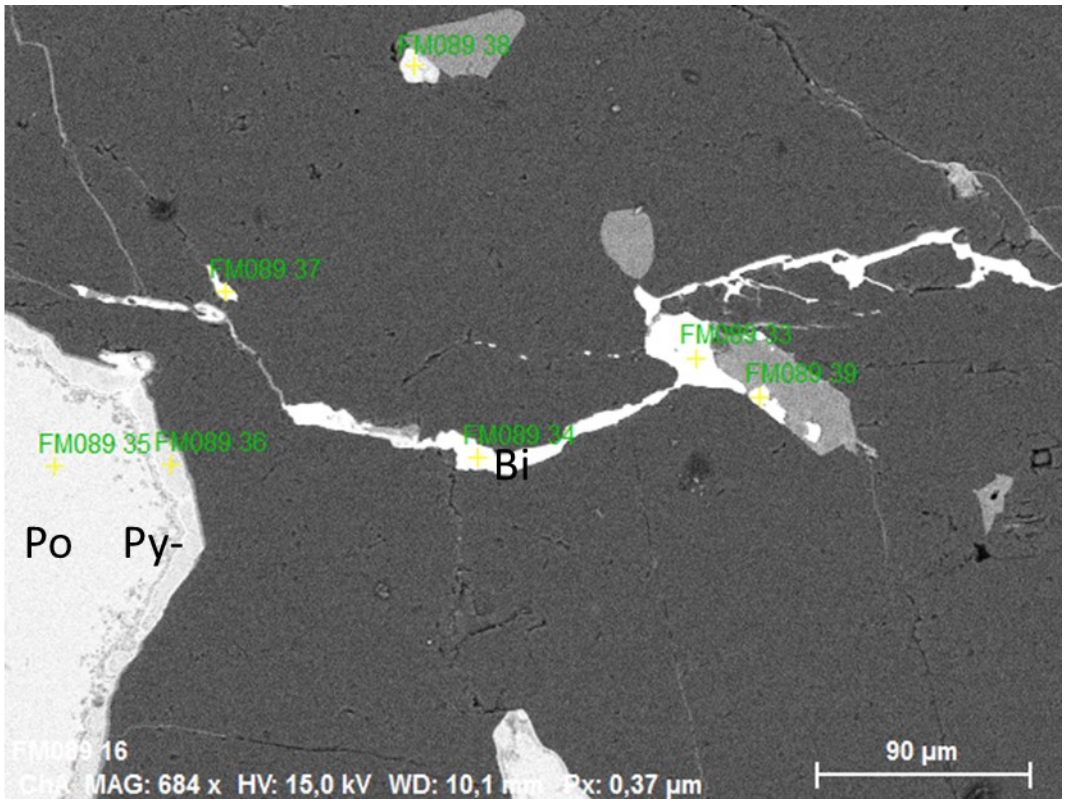

Figure 43: Sample 15RH05, analyses 33-39. Bi=native Bi, Po=pyrrhotite, Py=pyrite.

4.5.12 Uranium-Thorium phases

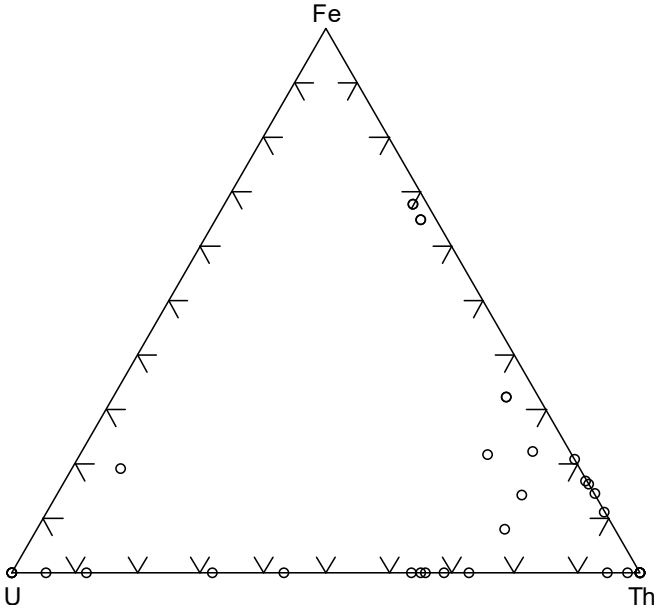

Figure 44: Uranium, Fe and Th contents in uraninite-thorite grains.

In most aplitic granites, U-Th minerals are present and often associated with zircon, allanite or phosphates (see Assemblages section 4.5.16). Most frequent are thorite and uraninite and solid solutions of them, often with a significant Fe content (Figure 44). In both minerals are often considerable Pb contents of several percents, see Table 3. In addition, also cheralite ($CaTh(PO_4)_2$) and calciothorite ($(Th,Ca_2)SiO_4 \cdot 3.5H_2O$) were found.

Mineral	sample	O	Al	Si	P	S	Ca	Fe	Pb	Th	U
Fe-Thr	18PH4_27	65.05		11.90				4.84		18.20	
Fe-Thr	FM100 191	61.37		8.06	2.37	1.71	2.47	16.30	0.00	7.18	0.53
Fe-Thr	FM100 192	63.76	3.60	11.01	1.98	1.01	4.08	4.65	0.19	8.98	0.74
Fe-Thr	FM100 196	60.95	4.76	9.45		1.23	1.88	14.11	0.00	7.07	0.54
Fe-Urn	18PH4_3	64.35						6.85	0.11	2.70	26.00
Thr	17PH01 23	66.67		16.72					0.00	15.75	0.87
Thr	17PH01_58	65.58	4.10	14.43	5.03		3.74			7.13	
Thr	17PH09	64.55	-	11.91				4.44	0.27	14.31	1.22
Thr	18PH4_10	65.43	0.69	11.89	1.46	0.19	0.98	3.29	0.00	16.03	0.04
Thr	18PH4_35	64.37		8.11	2.68		4.36	2.18		17.19	
Thr	18PH4_40	64.27	4.82	13.97			1.39	3.39		10.06	2.10
Thr	18PH5_31	64.78	4.69	10.78	4.30	1.29	2.63	1.49		8.70	
Thr	18ZT2_15	66.67		16.72						16.61	
Thr	FM089	64.83		16.03			1.72	1.13	0.21	10.55	2.50
Thr	FM089	63.92		11.41			2.73	3.00		15.27	2.41
Thr	FM099 19	66.90		15.70	1.43					15.96	
Thr	FM099_35	66.67		14.75						18.58	
Thr	FM099_36	66.67		16.62					0.00	16.71	
Thr	FM099_37	65.11	2.03	15.60			3.36		0.29	13.61	
Thr	FM100 193	66.43		16.67	1.01		1.00		0.20	14.40	0.29
Thr	FM100 197	65.51	2.44	14.23		1.78	1.68	2.36		12.01	
Thr	FM100 191	61.37		8.06	2.37	1.71	2.47	16.30	0.00	7.18	0.53
Thr	FM100 192	63.76	3.60	11.01	1.98	1.01	4.08	4.65	0.19	8.98	0.74
Thr	FM100 196	60.95	4.76	9.45		1.23	1.88	14.11	0.00	7.07	0.54
Urn	17RH18	66.73							0.27	0.00	32.69
Urn	17RH18	66.47							0.33	0.00	33.07
Urn	17RH18	66.45							0.29	0.00	33.08
Urn	18PH4_2	66.56							0.33	3.94	29.17
Urn	18PH4_21	66.67		13.11						0.39	6.86

Mineral	sample	O	Al	Si	P	S	Ca	Fe	Pb	Th	U
Urn	FM099 14	66.31		3.28							30.40
U-Thr	FM099 222	64.56		15.84					0.13	11.00	5.00
U-Thr	FM099 34	66.41		16.54			0.07		0.25	10.72	5.79
U-Thr	FM099_38	66.66		15.75					0.00	12.80	4.79
U-Thr	18PH4_15	66.69	1.14	14.84	0.95	0.30			0.12	10.50	5.46
U-Thr	18PH4_9	66.67		14.83					0.00	11.76	6.74
U-Thr	18PH5_58	66.67		7.48						6.53	14.03
U-Thr	18PH5_59	66.62		10.27	1.76					8.15	10.73

Table 3: SEM EDX analyses of U-Th minerals, all numbers are normalized atomic percent. Urn = uraninite, Thr thorite, Fe-Thr=Fe-thorite, U-Thr=U-Thr.

4.5.13 Molybdenum alteration phases

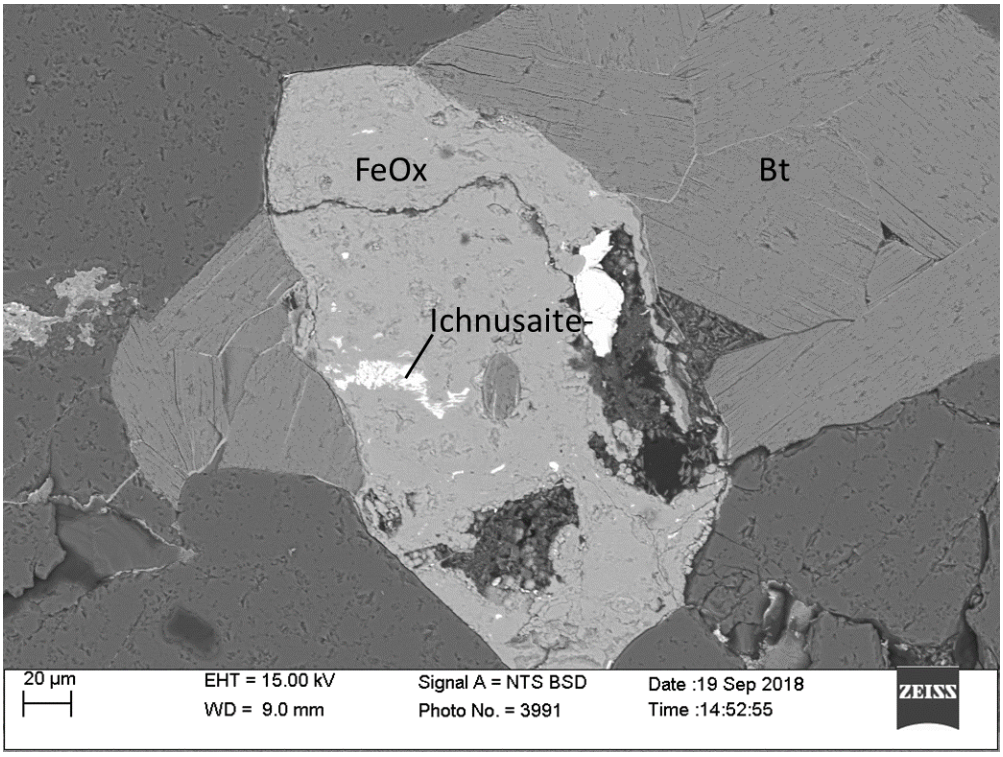

Figure 45: Sample 18ZT2, analyses 1-5. Bt=biotite.

In most thin sections, Mo occurs only in molybdenite, which is rather pure except some inclusions of Bi-minerals (see chapter 4.5.11) and a minor Re content. However, there is one thin section, 18ZT2, for which this is not true. This sample is one of the few, in which molybdenite-quartz veins with a surrounding alteration could be observed. With the SEM, the common alteration minerals wulfenite ($PbMoO_4$; Figure 41) and powellite ($Ca(MoO_4)$; Figure 48) could be identified. Table 4 shows all analyses of Mo containing minerals except molybdenite and possible corresponding mineral names fitting the chemistry.

Fine-grained “alteration phases” (Figure 46) which do not fit with which any known mineral were found frequently and are considered as the Mo bearing equivalent of FeOx. Besides Mo, they contain Pb, Fe, O and elements typical for silicates (Na, Al, Si and Ca) in various portions. In this category probably also the Mo-galena and the Mo-hematite should be included.

A mineral probably chemically similar to Betpakdalite-CaCa ($[Ca_2(H_2O)_{17}Ca(H_2O)_6][Mo^{6+}_8As^{5+}_2Fe^{3+}_3O_{36}(OH)]$) was only found in one analysis, unfortunately at an inappropriate zoom level (Figure 47) at the examination after the measuring.

Ichnusaite [$Th(MoO_4)_2 \cdot 3H_2O$, monoclinic (Orlandi et al., 2014)] and nuragheite [$Th(MoO_4)_2 \cdot H_2O$, no crystal structure known (Orlandi et al., 2015a)] differ only in their H_2O contents. As there are many similar measurements in adequate sized grains (Figure 45, right bright grain), which fit these minerals' chemistry it is sure that at least one of them was measured. In figures, this phase is referred to as ichnusaite.

Sardignaite [$BiMo_2O_7(OH) \cdot 2H_2O$, monoclinic, Figure 41 (Orlandi et al., 2010)] is also a mineral, which can be assumed to exist due to reasonable analyses in sample 18ZT2. However, it is to note, that sardignaite has a high content of O and H which could not be measured.

Although only present in one grain (Figure 46b), it is likely, that suseinargiuite [$(Na_{0.5}Bi_{0.5})(MoO_4)$, no crystal structure known (Orlandi et al., 2015b)] is present in sample 18ZT2, as the combination of Na, Bi and Mo is only present in suseinargiuite. However, it cannot be excluded, that new minerals with this composition will be described which fit the analysis or structure better.

Orlandi and coworkers described Ichnusaite/nuragheite, sardignaite and suseinargiuite from the Mo mineralization Su Seinargiu in Sardinia. Sardignaite is already known from the Reichenspitzgruppe at the Gabler (Burgsteiner, 2017; Walter et al., 2016), suseinargiuite and ichnusaite are not yet described outside the type locality. Unfortunately, this finding cannot contribute mineralogical data to the incomplete descriptions of suseinargiuite/nuragheite as the grains are very small as at the type locality.

Possible mineral	Spektrum	Figure	O	Na	Al	Si	S	Ca	Fe	As	Mo	Ag	Te	Re	Pb	Bi	Th
Alteration phase	18ZT2_ 46		67.71		2.18	0.29	0.54	0.98	23.23		4.62						
Alteration phase	18ZT2_ 48		63.93			0.77	0.00	1.45	19.64		13.68						
Alteration phase	18ZT2_ 59		29.22		6.35	38.86	0.00	1.63			11.94				12.01		
Alteration phase	18ZT2_ 60		28.97		6.69	39.47					11.26				13.61		
Alteration phase	18ZT2_ 61	Figure 46a	67.18							3.46	15.71				11.22	2.44	
Alteration phase	18ZT2_ 63		8.28				45.60				9.85				12.23	24.04	
Alteration phase	18ZT2_ 64		69.51	0.84							16.42					13.23	
Alteration phase	18ZT2_ 65		65.22				0.00				10.82				6.39	17.58	
Alteration phase	18ZT2_ 66		63.55								9.98	2.80			6.59	17.09	
Betpakdalite-CaCa	18ZT2_ 15	Figure 47	62.94		1.40	4.10	1.59	9.08	7.06	1.98	8.46				3.38		
Ichnusaite/ Nuragheite	18ZT2_ 1	Figure 45	65.84				1.22				19.46	0.00					13.48
Ichnusaite/ Nuragheite	18ZT2_ 14		73.72			0.75	1.40				13.74	0.00					10.40
Ichnusaite/ Nuragheite	18ZT2_ 21		68.10				0.78				19.75	0.00					11.37
Ichnusaite/ Nuragheite	18ZT2_ 3		59.90			0.46	0.66		7.09		19.73	0.00					12.17

Possible mineral	Spektrum	Figure	O	Na	Al	Si	S	Ca	Fe	As	Mo	Ag	Te	Re	Pb	Bi	Th
Ichnusaite/ Nuragheite	18ZT2_ 30		72.53								17.58						9.89
Ichnusaite/ Nuragheite	18ZT2_ 32		71.92				0.67		1.20		16.39				0.09		9.70
Ichnusaite/ Nuragheite	18ZT2_ 33		71.75				0.42		1.59		16.47				0.04		9.66
Ichnusaite/ Nuragheite	18ZT2_ 45		76.52				0.27		2.93		11.08	9.19			0.00		
Ichnusaite/ Nuragheite	18ZT2_ 50		73.89	0.09		0.31	0.00		1.89		14.17	9.59			0.06	0.00	
Ichnusaite/ Nuragheite	18ZT2_ 51		71.65				0.04		2.69		17.61						8.01
Ichnusaite/ Nuragheite	18ZT2_ 7		69.90			1.17			3.24		15.97	0.00					9.72
Ichnusaite/ Nuragheite	18ZT2_ 74		70.93				0.30		2.71		15.20	0.00					10.86
Ichnusaite/ Nuragheite	18ZT2_ 75		70.12		0.59	1.22	0.00	1.42	2.80		14.80						8.91
Ichnusaite/ Nuragheite	18ZT2_ 82		71.05				0.00		3.25		16.40	0.00					9.29
Mo-galena	FM099_ 28		9.06				30.03				3.23				57.69		
Mo-hematite	18ZT2_ 70		58.56		1.35	1.05	0.00		31.35		7.69						
Mo-hematite	18PH5_ 13		68.72				0.27		24.00		7.02						
Mo-hematite	18PH5_ 14		69.18			0.31	0.23		23.69		6.58						
Mo-hematite	18PH5_ 15		60.47				6.45		7.71		11.02				14.36		
Mo-hematite	18ZT2_ 9		61.71		1.93	0.38	0.45		28.47		7.04			0.02			
Powellite	18ZT2_ 13		66.30			0.46	0.00	17.17			16.05						
Powellite	18ZT2_ 14		64.21			0.47	0.00	18.39			14.96						
Powellite	18ZT2_ 16		65.02			0.20	1.05	16.12			15.08						
Powellite	18ZT2_ 68	Figure 48	66.32				0.00	18.19			15.49						
Sardignaite	18ZT2_ 12	Figure 41	62.57								23.97					13.43	
Sardignaite	18ZT2_ 10	Figure 41	59.34								25.12					15.54	
Sardignaite	18ZT2_ 8	Figure 41	62.83								24.24					12.64	
Sardignaite	18ZT2_ 9	Figure 41	69.71								17.28					12.96	
Suseinargiuite	18ZT2_ 54	Figure 46b	67.53	5.68							16.95	0.92				8.92	
Suseinargiuite	18ZT2_ 55	Figure 46b	68.89	4.20							18.31	1.05				7.55	
Wulfenite	18ZT2_ 11	Figure 41	68.40								16.34				15.26		
Wulfenite	18ZT2_ 11		63.30		1.06	3.02	0.00				14.67				17.95		
Wulfenite	18ZT2_ 19		57.26				0.00				18.89				23.85		
Wulfenite	18ZT2_ 20		66.09		1.60	2.66					12.93				16.72		
Wulfenite	18ZT2_ 35		68.57				0.00				18.57				12.85		
Wulfenite	18ZT2_ 39		66.47								16.47				17.07		
Wulfenite	18ZT2_ 42		62.23			6.42	0.00				12.89				18.46		
Wulfenite	18ZT2_ 43		60.60			9.31	0.00	5.82			11.23				13.04		
Wulfenite	18ZT2_ 44		70.47			3.00	0.00	5.84			10.48				10.21		
Wulfenite	18ZT2_ 83		64.31				0.00	1.11	5.13	4.13	13.28				12.04		
Wulfenite	FM099_ 34		68.53				0.00				13.11			0.00	18.36		

Table 4: SEM EDX analyses of Mo containing minerals. Note, that the mineral names are only proposed according to the approximate composition without H_2O, CO_2 and only roughly estimated O contents. All numbers are normalized atomic percent.

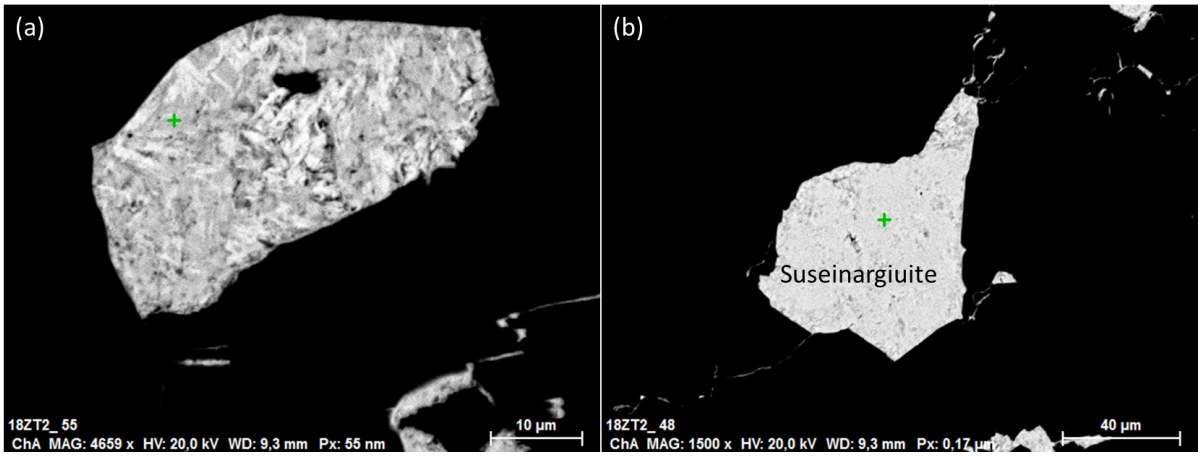

Figure 46: Sample 18ZT2, (a) analyses 61, 62 white is Bi oxide, grey is Mo-Pb-Bi-O alteration phase (analysis 18ZT2_61 in Table 4); (b) analyses 54, 55.

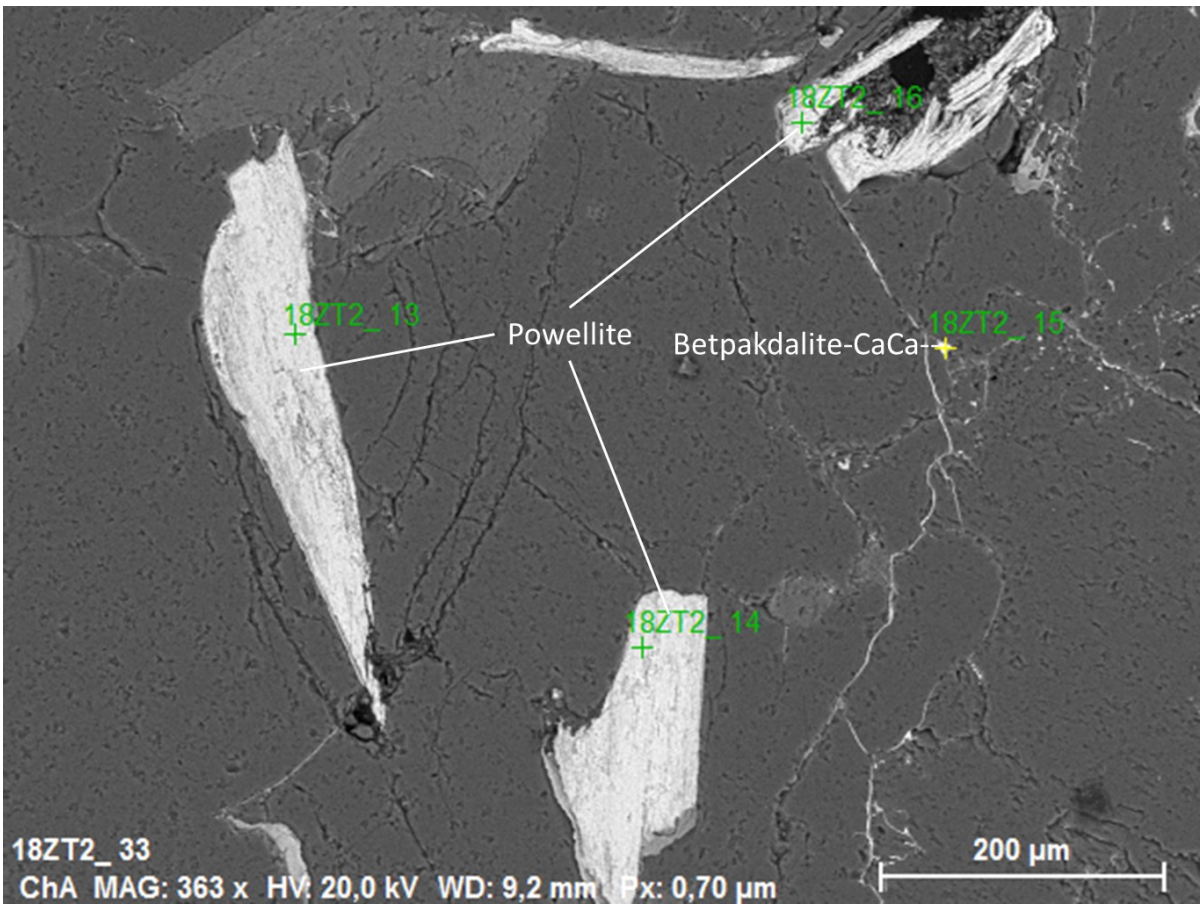

Figure 47: Sample 18ZT2, analyses 13-16.

Figure 45 shows two ichnusaite aggregates in a larger former crystal, which is now composed of FeOx. The most outstanding proof that these minerals formed during a later alteration is shown in Figure 48, where powellite pseudomorphous after molybdenite can be observed. Figure 47 is similar, although it can only be speculated, that the powellite is pseudomorphous after molybdenite, though the probable betpakdalite-CaCa in the cracks is a very distinct sign for the alteration present here.

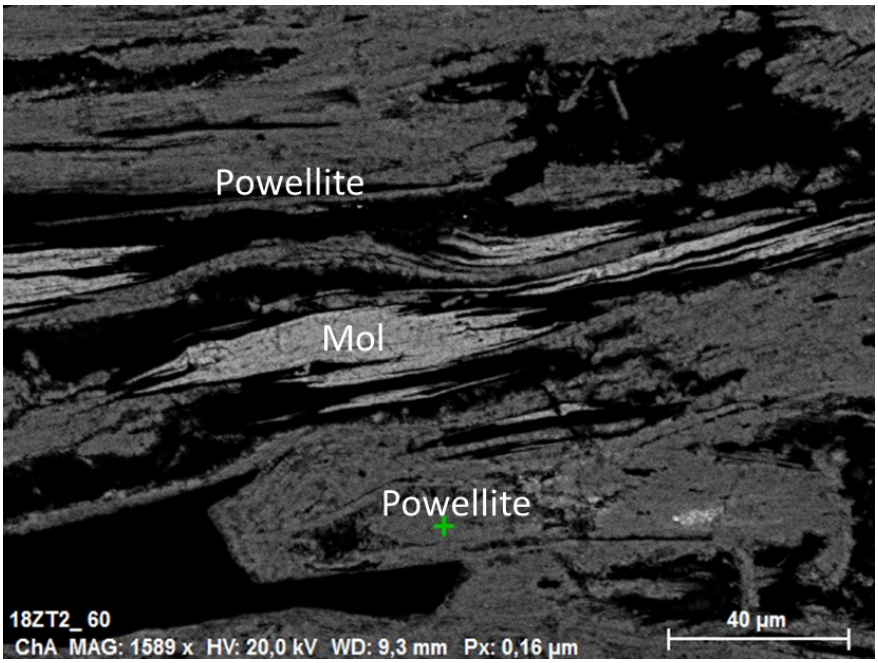

Figure 48: Sample 18ZT2, analyses 67, 68. Mol=molybdenite

4.5.14 REE phases

In the aplitic granites, REE-bearing minerals are common (see Table 5 for REE contents in the REE containing minerals). Allanite is most widespread and often zoned (Figure 49), but there are also numerous other phases: aeschynite-(Y) ($(Y,La,Ca,Th)(Ti,Nb)_2(O,OH)_6$), bastnäsite ($(Ce,La)(CO_3)F$), euxenite ($(Y,Ca,Ce,U,Th)(Nb,Ta,Ti)_2O_6$), monazite ($Ce(PO_4)$), monazite-apatite, synchysite-(Ce) ($CaCe(CO_3)_2F$) and xenotime ($Y(PO_4)$, Xtm). Those minerals rarely occur solitary but most often together with zircon or U-Th minerals (see Assemblages section 4.5.16).

Mineral	Spektrum	Y	Nb	La	Ce	Nd	Hf	Ta	Pr+Sm+Eu+Gd+Dy+Yb+Hf	Th
Aeschynite(Y)	FM100 167	7.22	8.88		0.00	0.09		1.07	0.64	
Aeschynite(Y)	FM100 168	4.44	5.15	0.91	0.07	0.11	2.07	1.42	2.88	0.11
Aeschynite(Y)	FM100 169	7.46	7.19	0.15	0.02	0.13	0.47	1.13	1.11	
Aeschynite(Y) U is missing	FM100 167	7.22	8.88		0.00	0.09		1.07	0.64	
Aeschynite(Y) U is missing	FM100 168	4.44	5.15	0.91	0.07	0.11	2.07	1.42	2.88	0.11
Aeschynite(Y) U is missing	FM100 169	7.46	7.19	0.15	0.02	0.13	0.47	1.13	1.11	
Allanite	17PH01 21				2.96				0.00	
Allanite	17PH01_ 47	11.94	0.00		0.07				1.41	
Allanite	17PH01_ 48	12.48	0.00		0.00				0.65	
Allanite	17PH01_ 49	8.99	0.25		0.17				0.40	
Allanite	17PH01_ 52	0.38							0.00	
Allanite	17PH01_ 53	11.11							0.00	
Allanite	17PH01_ 65			0.01	0.05				0.00	
Allanite	17RH18	1.49		6.08	10.21	2.66	0.00		0.30	0.83
Allanite	17RH18			3.39	5.97	1.43	0.07		0.07	0.92
Allanite	17RH18	1.20		1.81	3.94	1.26	0.05		0.82	0.27
Allanite	17RH18	1.01		2.97	5.61	1.51	0.00		0.15	0.29
Allanite	17RH18			3.95	7.10	2.39			0.00	0.59
Allanite	17RH18	1.29		5.31	9.62	2.80			0.14	1.04
Allanite	17RH18	1.67		2.33	4.48	1.80			0.11	0.37
Allanite	17RH18			2.88	5.32	1.58			0.32	0.92
Allanite	17RH18 127	1.50		3.60	6.45	2.61			0.60	0.00
Allanite	17RH18 133			3.06	4.54	1.34			0.00	5.41

Mineral	Spektrum	Y	Nb	La	Ce	Nd	Hf	Ta	Pr+Sm+Eu+Gd+Dy+Yb+Hf	Th
Allanite	17RH18 134			1.55	2.68	0.95			0.89	4.16
Allanite	17RH18 141			3.96	7.38	3.11			1.66	0.73
Allanite	17RH18 143			2.97	5.84	1.86			0.65	0.57
Allanite	17RH18 146	1.57		3.47	5.85	2.18			2.47	0.08
Allanite	17RH18 147	1.84		3.59	6.52	2.56			0.97	0.13
Allanite	17RH26			0.95	2.04	0.99			0.00	0.11
Allanite	17RH26			1.12	2.17	0.73			0.00	0.06
Allanite	17RH26			0.76	1.41	0.00			0.00	0.00
Allanite	17RH26			0.55	1.27	0.40			0.00	0.13
Allanite	17RH26			0.81	1.59	0.53			0.00	0.11
Allanite	17RH26			1.05	2.40	0.77			0.00	0.14
Allanite	17RH26			0.50	1.02	0.10			0.00	0.01
Allanite	17RH37 182				1.22				0.16	
Allanite	17RH37_ 1				2.04				1.31	
Allanite	17RH37_ 7			1.04	1.65	0.50			0.64	
Allanite	17RH37_ 8			0.01	0.03	0.00			0.01	
Allanite	18PH4_ 16	0.00			0.08				0.00	
Allanite	18PH4_ 22	0.74			0.05				0.00	
Allanite	18PH4_ 28	0.34			0.01				0.00	0.03
Allanite	18PH4_ 30	0.06			0.04				0.00	0.05
Allanite	18ZT2_ 18	1.51							0.00	
Allanite	18ZT2_ 76	1.80			0.05				0.00	
Allanite	18ZT2_ 77	2.05			0.04				0.00	
Allanite	FM099 10								0.00	0.81
Allanite	FM099 17				2.07	0.83			1.08	
Allanite	FM099 18			3.19	6.18	3.40			0.00	
Allanite	FM099 223				0.04				0.00	0.84
Allanite	FM100 173			0.31	0.82	0.42			0.51	0.04
Allanite	FM100 174			0.09	0.38	0.11			0.09	
Allanite	FM100 182			0.41	1.02	0.44			0.37	4.15
Allanite	FM100 184			0.62	1.47	0.49			0.51	0.69
Bastnäsit	17RH18			5.62	9.99	2.82			1.17	1.14
Euxenite	17PH01_ 39	13.44	17.93		0.19	0.00			0.73	
Euxenite	17PH01_ 43	14.60	17.85		0.17	0.06			0.36	
Monazite	18PH5_ 22			2.67	5.61	2.08			0.00	6.80
Monazite	18PH5_ 25			3.18	5.89	2.62			0.00	
Monazite	18PH5_ 38	0.00		4.75	7.97	2.45	0.26		0.26	0.11
Monazite	18PH5_ 40			3.33	6.58	2.74			0.00	
Monazite	18PH5_ 46			3.74	7.23	2.80			0.00	
Monazite	18PH5_ 48			3.42	6.93	3.15			0.00	
Monazite	18PH5_ 60			4.24	8.37	3.33			0.00	0.27
Monazite	18PH5_ 62			3.69	7.14	2.92			0.00	0.64
Monazite-Apatite	18PH5_ 41			2.78	5.88	2.19			0.00	2.16
Monazite-Apatite	18PH5_ 42			3.34	6.62	2.22			0.00	0.97
Monazite-Apatite	18PH5_ 43			3.17	6.32	2.71			0.00	1.98
Synchisite	17RH18 129	2.53		3.13	5.84	3.30			0.00	0.70
Synchisite	17RH18 129	2.53		3.13	5.84	3.30			0.00	0.70
Xenotime	17PH01 26	13.40							0.92	
Xenotime	17PH01 27	13.67							0.79	
Xenotime	17PH01_ 55	12.96			0.00				0.06	
Xenotime	17PH01_ 66	12.57							0.00	
Xenotime	18PH4_ 34	10.70							0.00	
Xenotime	18PH4_ 44	13.69			0.00				1.78	0.14
Xenotime	18PH5_ 44	12.57	0.00					0.62	1.52	0.32
Xenotime	18PH5_ 50	12.81							1.01	
Y-Allanite	18PH4_ 13	9.41			0.07				0.00	
Y-Allanite	18PH4_ 23	12.77			0.06				1.61	
Y-Allanite	18PH4_ 25	12.81			0.00				0.00	0.14

Table 5: SEM EDX analyses of REE contents in REE containing minerals. Note, that the mineral names are only proposed according to the approximate composition without H_2O, CO_2 and only roughly estimated O contents. All numbers are normalized atomic percent. The complete analyses are in the appendix.

4.5.15 Very rare accessories

In sample 18ZT2, which contains many rather exotic phases also acanthite/argentite (Ag_2S) and lillianite ($Pb_{3-2x}Ag_xBi_{2+x}S_6$) were found. Ag is known from the area as a component in electrum

(Burgsteiner, 2017; Walter et al., 2016), but not yet as sulfide. In sample 17PH01 tiemannite (HgSe; 48 atomic percent Se, 40 atomic percent Hg, 8 atomic percent O and 2 atomic percent Si, the latter two are probably from the surrounding quartz) was found as an inclusion in quartz.

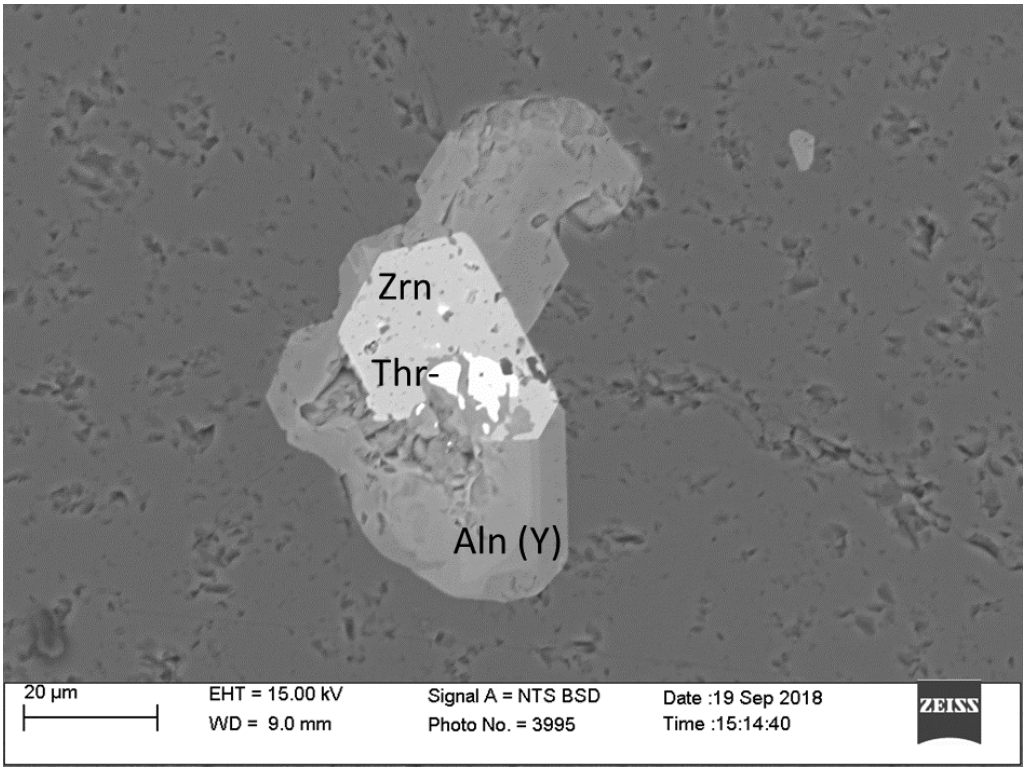

Figure 49: Sample 18ZT2, analyses 15-18. Note the visible zoning of the allanite in the lower part visible due to an enrichment of REE (mainly Y) in the core. Aln (Y)=allanite (Y), Thr=thorite, Zrn=zircon.

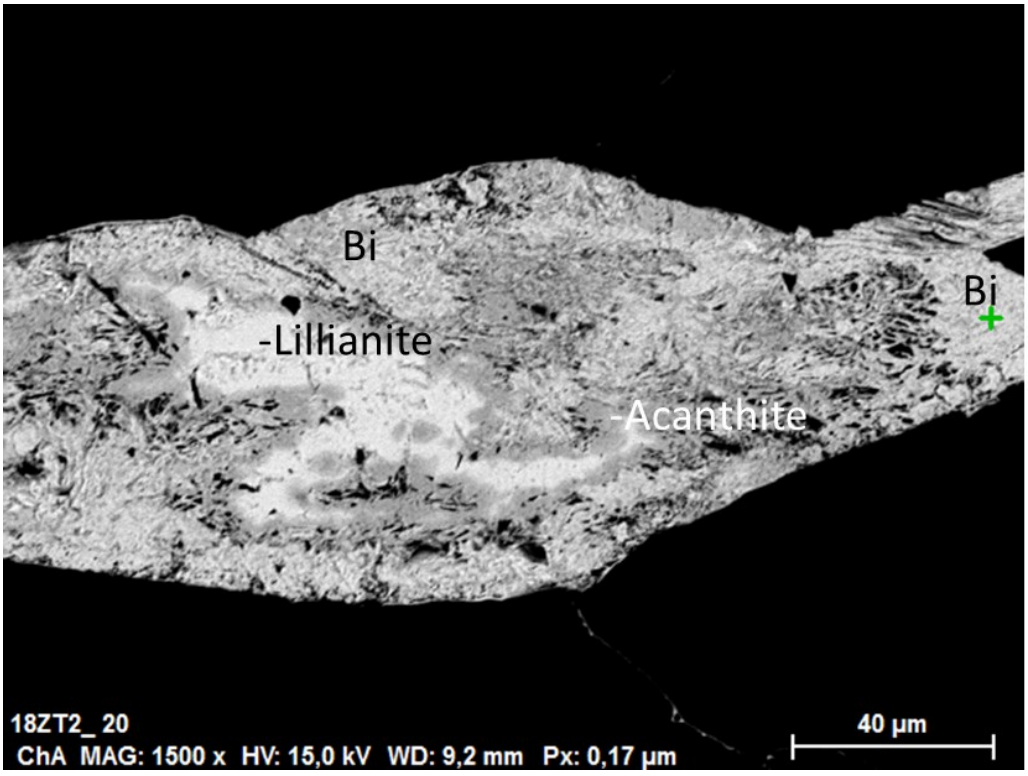

Figure 50: Sample 18ZT2, analyses 25-29. Bi=Bismuth oxide (bismite?)

4.5.16 Assemblages

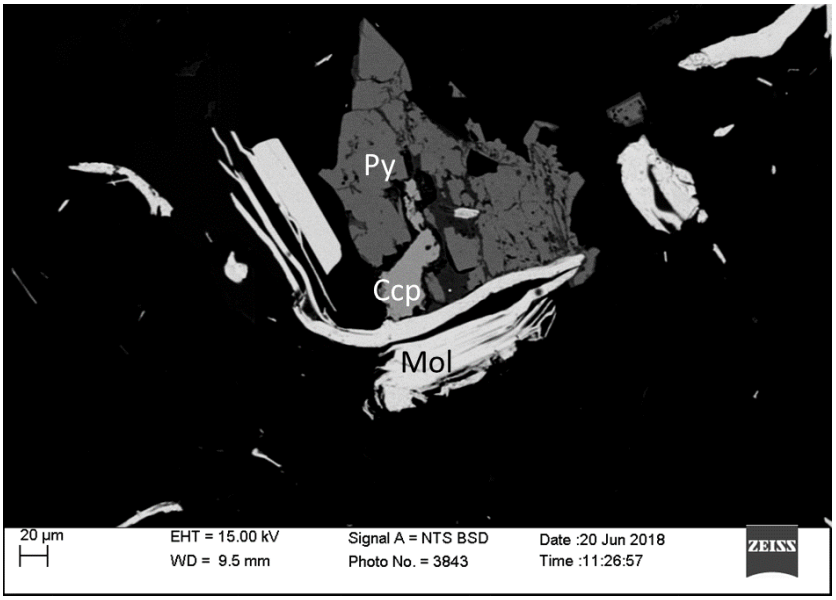

Figure 51: Sample 17RH37, analyses 9-10. Ccp=chalcopyrite, Mol= molybdenite, Py=pyrite.

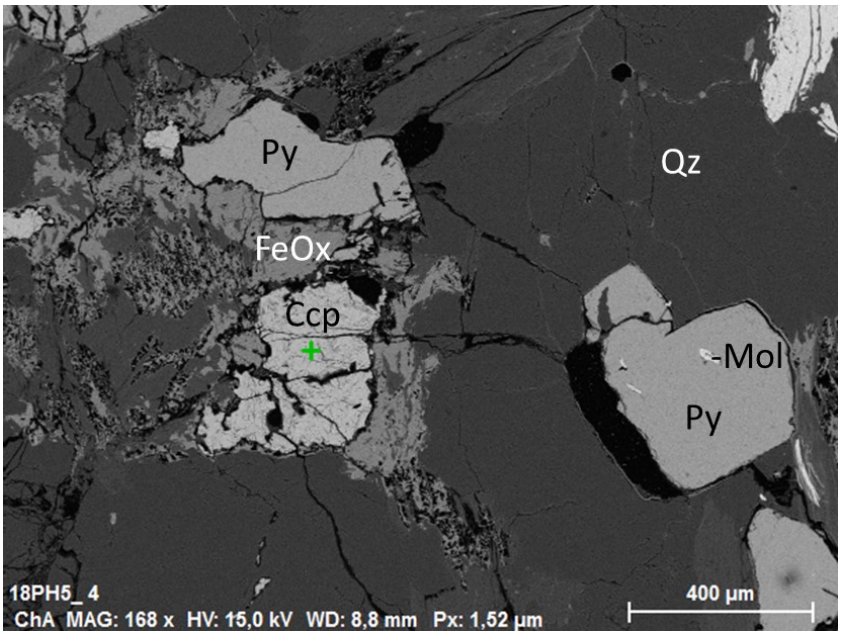

Figure 52: Sample 18PH5, analyses 5-8. Ccp=chalcopyrite, Mol=molybdenite, Py=pyrite, Qz=quartz.

This chapter deals with assemblages, that frequently occur throughout the examined thin sections, although all presented minerals were also observed alone. Figure 51 shows an assemblage typical for porphyry deposits including molybdenite, chalcopyrite and pyrite. This assemblage is very rare in the Reichenspitze area. Most (~90%) of the molybdenite are without additional ore minerals. Few are associated with pyrite, and chalcopyrite is even less abundant. Figure 52 is even more special, as it shows molybdenite inclusions in pyrite, a clear proof, that they formed contemporaneously.

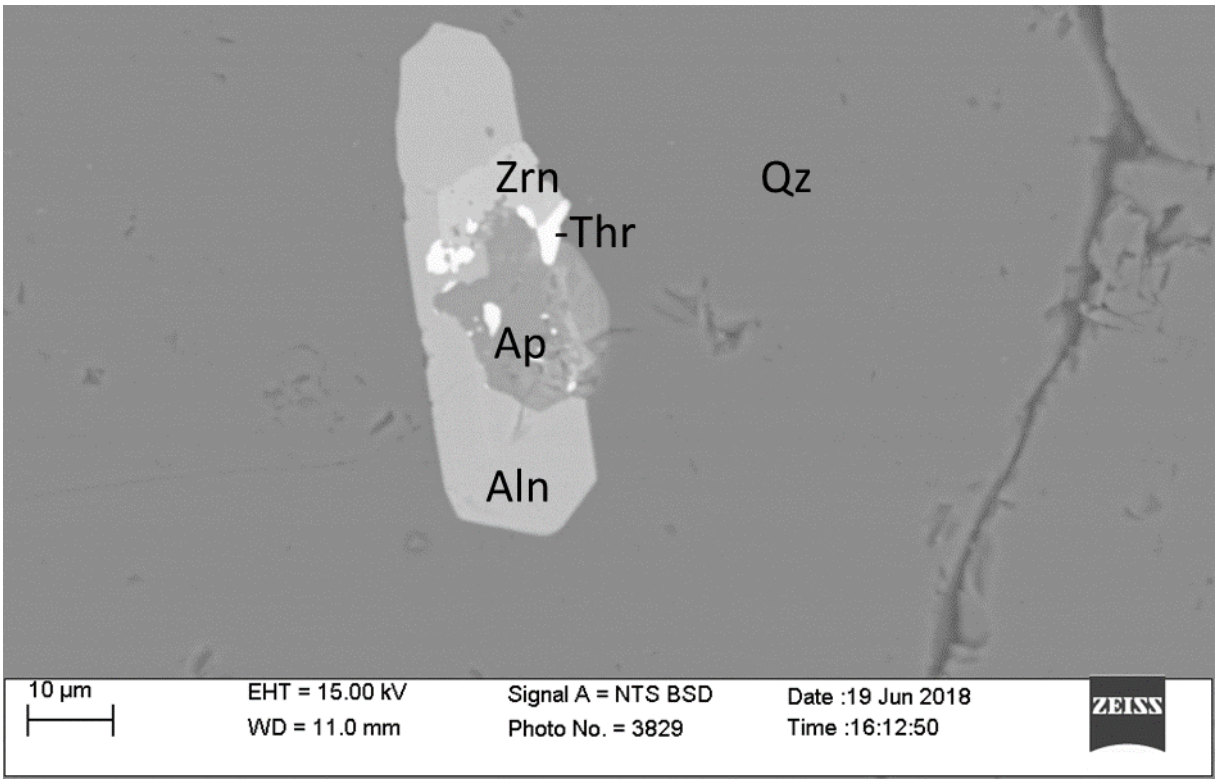

Figure 53: Sample 17PH01, analyses 20-24.Aln=allanite, Ap=apatite, Thr=thorite, Zrn=zircon.

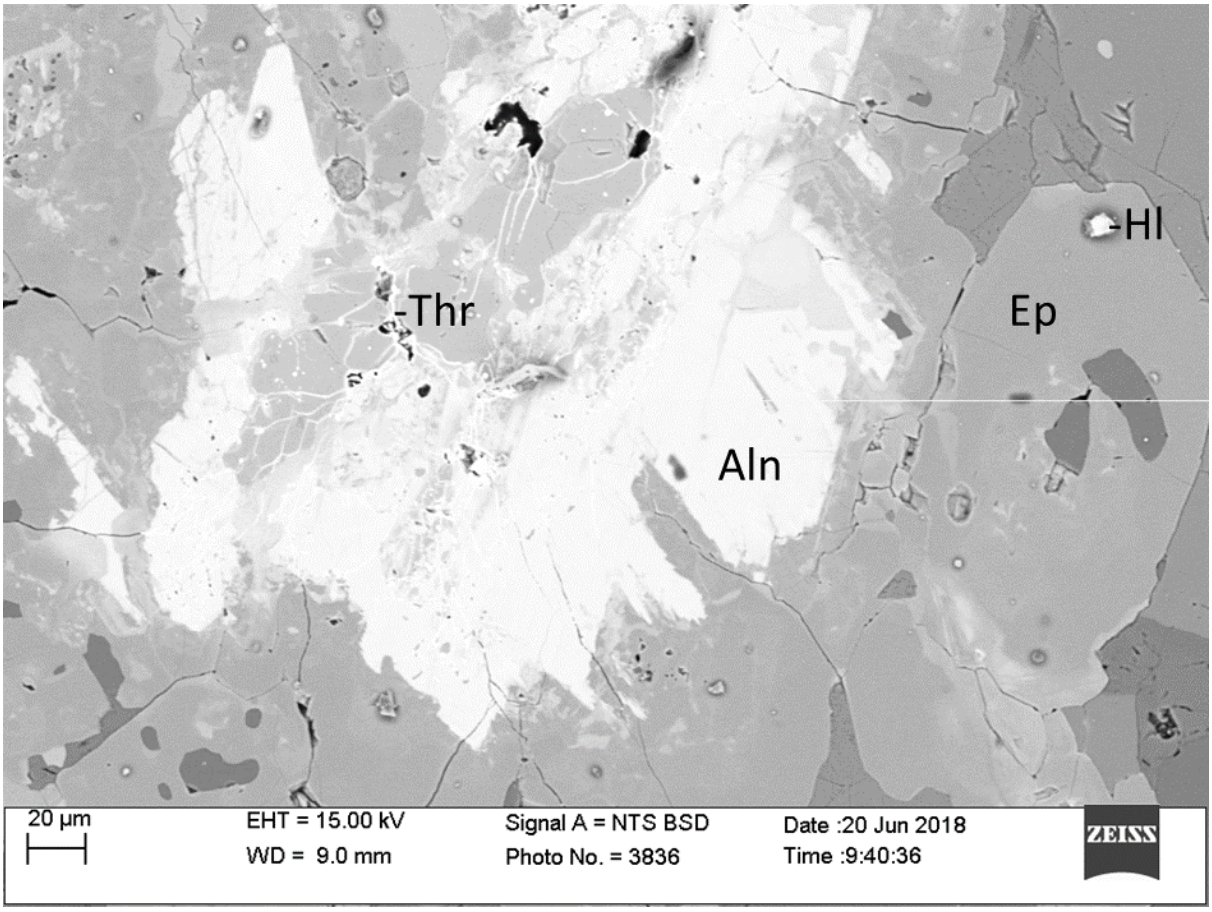

Figure 54: Sample 17RH37, analyses 1-6. Aln=allanite, Ep=epidote, Hl=halite, Thr=thorite.

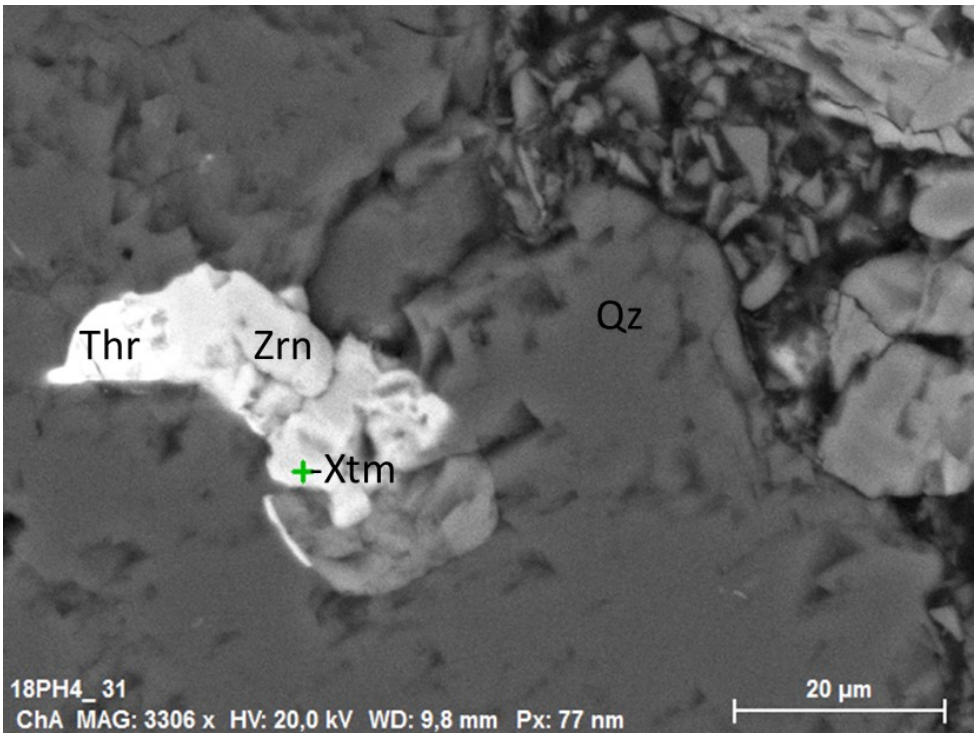

Figure 55: Sample 18PH4, analyses 34-38. Qz=quartz, Thr=thorite, Xtm=xenotime, Zrn=zircon.

Figures 53 to 56 show variations of the very common allanite/epidote-zircon-thorite assemblage also often including phosphates (apatite, xenotime, monazite) and biotite. Note in Figures 53 and 49, that the allocation of REE is dependent on the availability of P. If P is present, REE-bearing phosphates are formed, else the REE with Y as the most common element are incorporated in allanite. Most REE-bearing allanites (Figures 49, 54 and 56) are zoned, this can be well observed on the backscatter SEM images as REE have a high atomic mass and appear brighter than the surroundings.

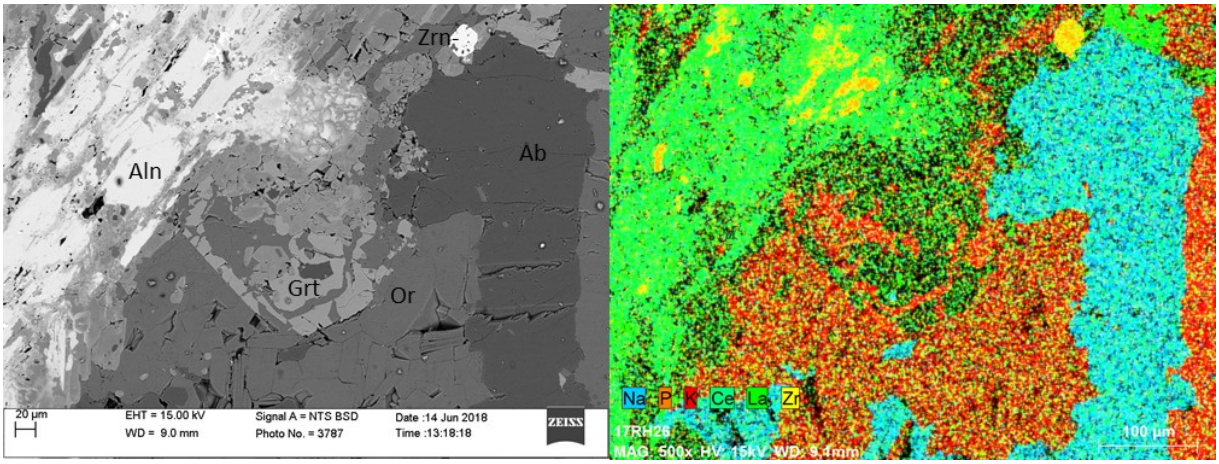

Figure 56: Sample 17RH26, analyses 75-81. Ab=albite, Aln=allanite, Grt=garnet, Or=orthoclase.

A special case of the allanite/epidote-zircon-thorite assemblage is shown in Figure 56. This is very typical for the molybdenite bearing aplitic granite, as it also includes skeletal garnet. Some

of these garnets together with biotite could be used for geothermometry (chapter 5.1.3). Another exceptional case of this assemblage is shown in Figure 57, where zircon contains Th bearing uraninite inclusions.

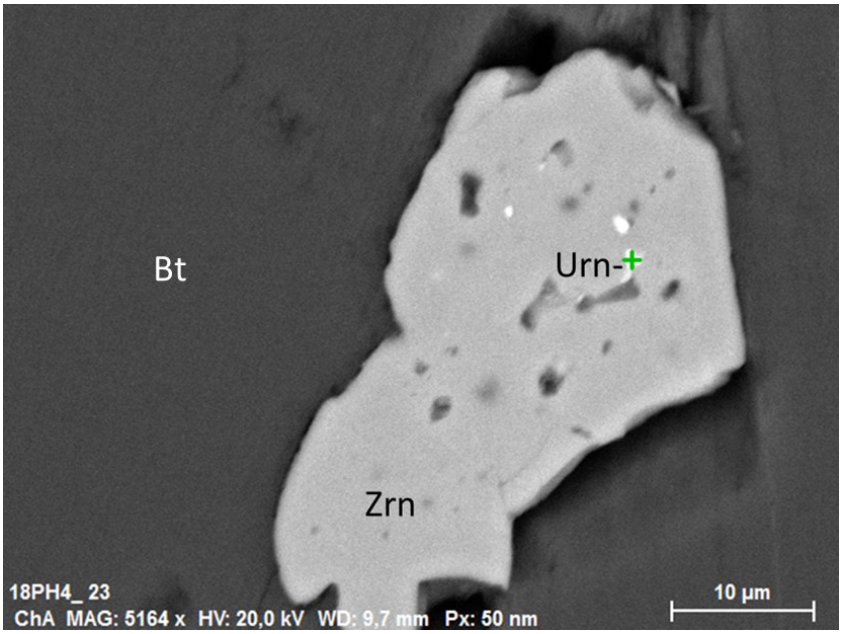

Figure 57: Sample 18PH4, analyses 20, 21. Bt=biotite, Urn=uraninite, Zrn=zircon.

5 Discussion

5.1 Petrology

5.1.1 Saussuritization

The chemical analyses yield normative compositions on the far left side of the Streckeisen diagram (Figure 21a), which accord neither with the TAS classification, nor with the modal composition, nor with what can be expected from the literature (Schermaier, 1993 and references therein). The classification after Streckeisen (1976) was initially designed for use with modal compositions, although being widespreadly used also with the normative composition calculated with the CIPW norm (in this work using the GCDkit in R). The CIPW norm assigns minerals to major elements and calculates a theoretical composition with standard minerals.

In the Streckeisen triangle, the A (alkali feldspar) component is defined as the sum of orthoclase and albite, the P component is defined as the anorthite content (Streckeisen, 1976). In terms of chemistry, this means that nearly the whole K and Na content is accounted for the A component and the Ca content for the P component. As plagioclase is a solid solution of anorthite and albite, this can lead to problems. Therefore Streckeisen and Le Maitre (1979) invented a slightly

different calculation (Figure 58b), that is indeed better, but still not what can be expected from microscopy. The strong saussuritisation of the plagioclase to saussurite is the problem. Figure 58a shows an element map produced with the SEM. The large pink (Na = albite component) crystal in the left part is a saussurite with microliths. Under the microscope with X N still polysynthetic twinning is recognizable. Chemically, this is albite and hence counts for the A component, but mineralogically this would count as anorthite for the P component.

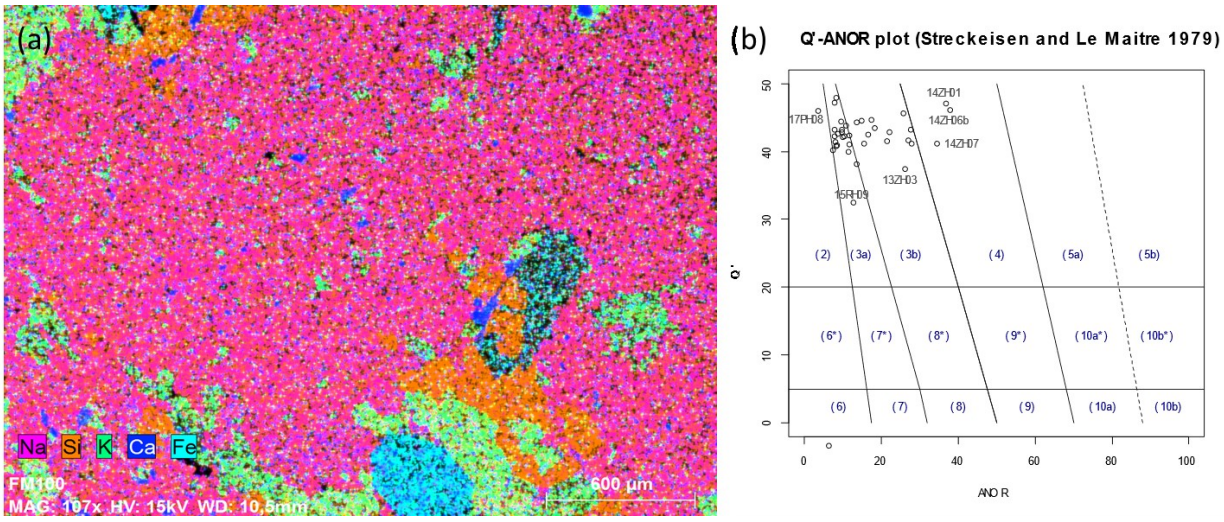

Figure 58: (a): SEM image of 13ZH09; (b): Q'-ANOR plot after Streckeisen and Le Maitre (1979) with all 38 measured samples, field names: 2 alkali feldspar granite 3 granite 4 granodiorite 5 tonalite 6 quartz alkali feldspar syenite 7* quartz syenite 8* quartz monzonite 9* quartz monzodiorite/quartz monzogabbro 10* quartz diorite/quartz gabbro 6 alkali feldspar syenite 7 syenite 8 monzonite 9 monzodiorite/monzogabbro 10 diorite/gabbro*

Following Exner and Faupl (1970), anorthite contents of 20-30% in plagioclase can be expected in the studied area. However, the SEM data indicate systematically lower anorthite contents, producing the biased classification with the Streckeisen diagram. Karl (1962) suggested an alkali metasomatism from field evidence. However, this is not likely as not only plagioclase would be affected. As a N-S gradient was observed with strongest saussuritization in the N, it can be assumed, that this is an effect of the Miocene metamorphic event which yielded a N-S gradient from greenschist to amphibolite facies (Schuster et al., 2004).

5.1.2 Zircon analysis

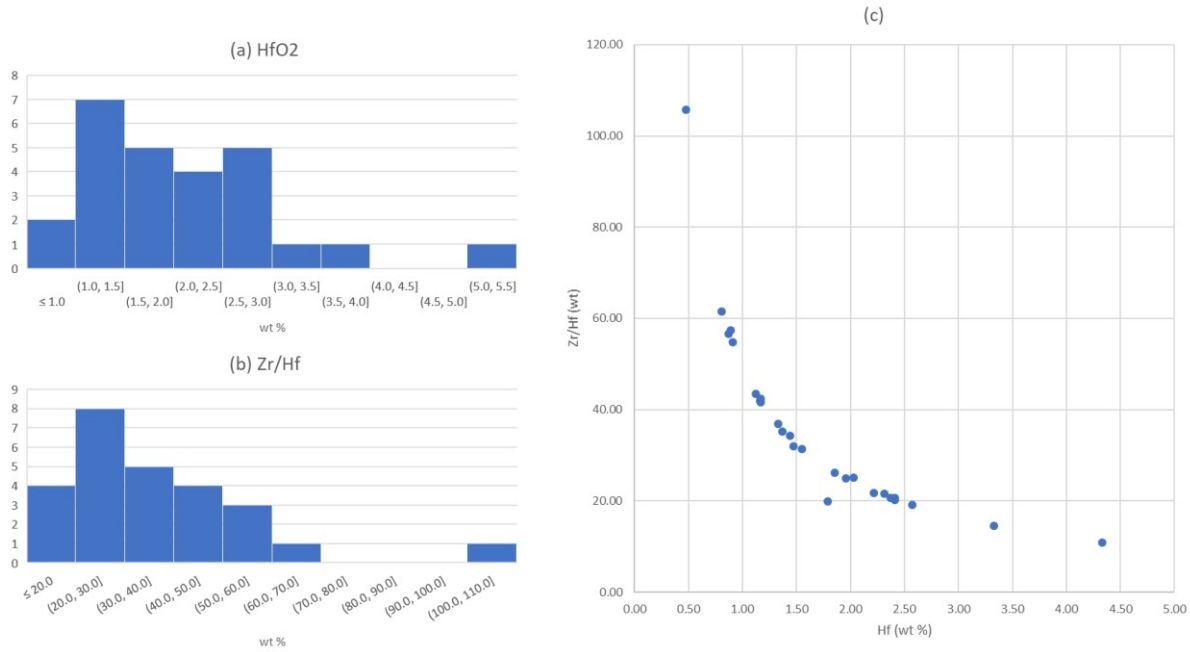

Figure 59: Zircon analyses of aplitic granites; (a) Histogram of HfO_2 contents; (b) Histogram of of Zr/Hf ratios; (c) Zr/Hf-Hf plot. All numbers are normalized weight percent.

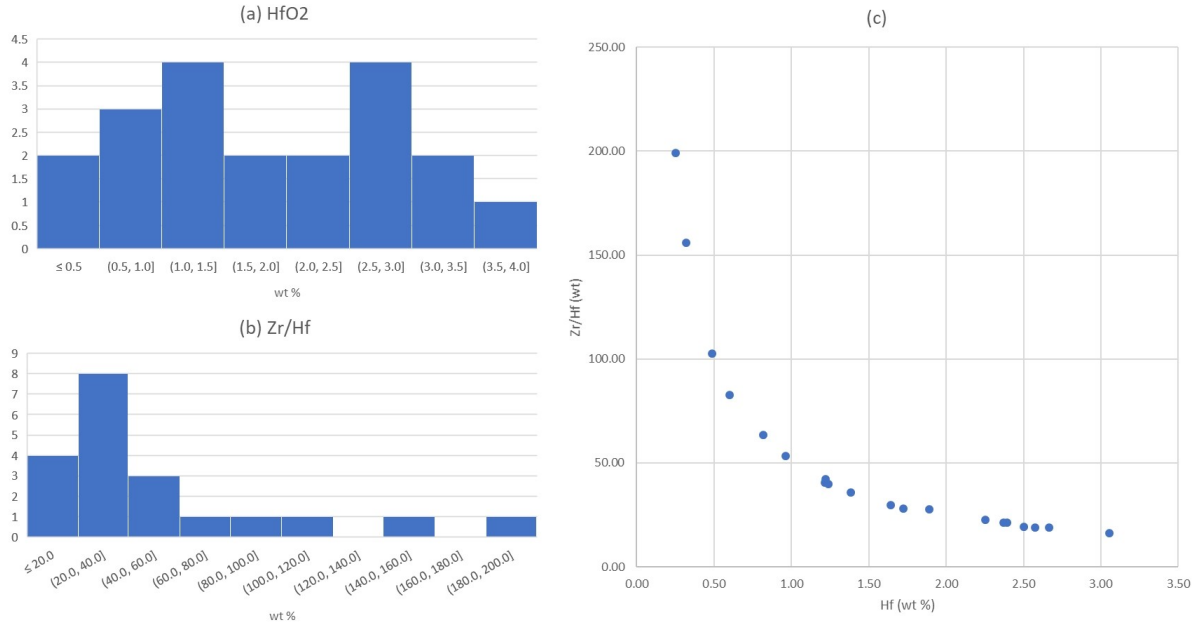

Figure 60: Zircon analyses of gneiss samples; (a) Histogram of HfO_2 contents; (b) Histogram of Zr/Hf ratios; (c) Zr/Hf-Hf plot. All numbers are normalized weight percent.

Using the SEM, 55 zircon grains were analyzed (Table 1). The data was interpreted following Wang et al. (2010). Hf = 0 values were excluded to avoid division by 0. The data show trends of exponentially decreasing Zr/Hf with rising Hf for the aplitic granites (Figure 59) and the gneisses (Figure 60). For the aplitic granites, the median value for Zr/Hf is 31.7 and for HfO_2 1.78. For the gneisses, the median value for Zr/Hf is 32.7 and for HfO_2 1.63. The numbers of Wang et al. (2010) for granitic zircon are somewhat higher with 38.5 respectively 1.43. As the

observed trends and distributions are very similar to those of Wang et al. (2010), it can be concluded from a comparison of the diagrams, that the majority of zircon in the samples is of early magmatic origin with some evolution towards late magmatic origin by fractionation. This suggests a rather slow initial cooling of the aplitic granite which allowed most zircon to crystallize and a low fractionation of the magmas (Wang et al., 2010).

5.1.3 Garnet-Biotite thermometry

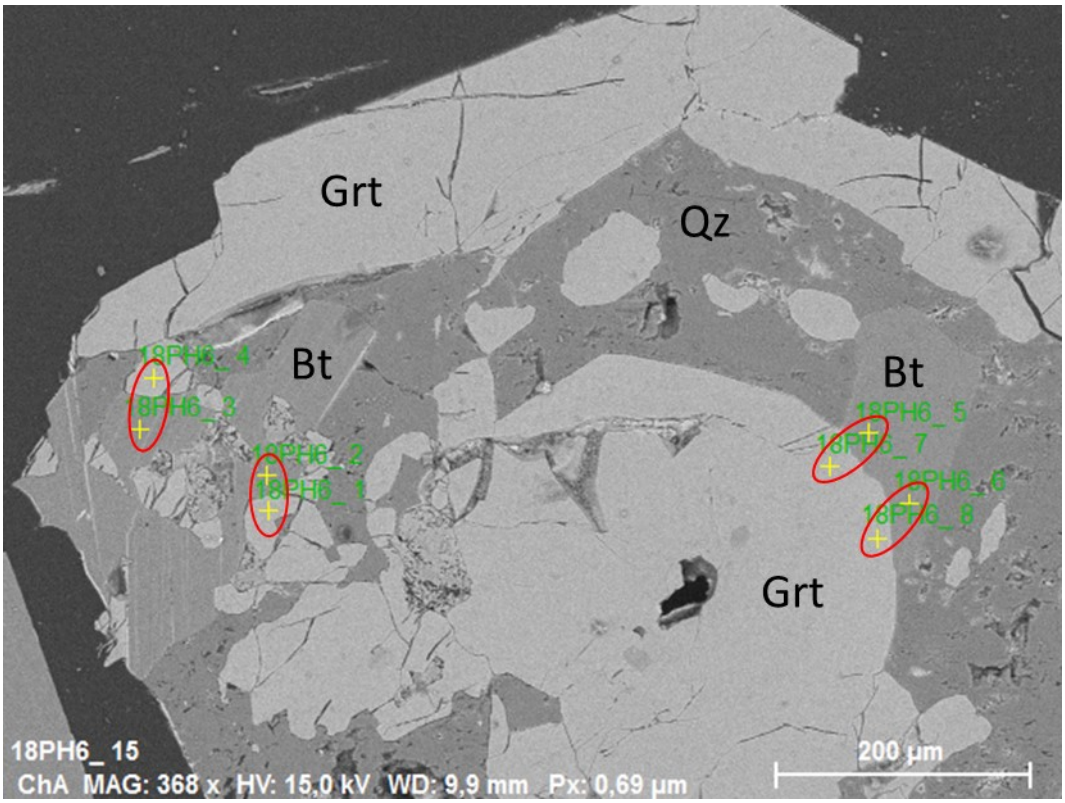

Figure 61: Red circles mark pairs of SEM point analyses (yellow crosses), sample 18PH6. Bt=biotite, Grt=garnet, Qz=quartz.

In one of the samples, 18PH6, direct contacts of garnet and biotite were found, see Figure 61 for a typical example of this section. The compositions of garnet and biotite at the rims were measured to carry out geothermometry. The Mg and Fe contents in garnet and biotite in contact vary according to a temperature dependent dynamic equilibrium. The formula of Bhattacharya et al. (1992) uses an updated formula for grossular-pyrope-almandine equilibria and is therefore well suited for this work:

$$T(HW) = [20286 + 0.0193P - \{2080(X_{GtMg})^2 - 6350(X_{GtFe})^2 - 13807(X_{GtCa})(1 - X_{GtMn}) + 8540(X_{GtFe})(X_{GtMg})(1 - X_{GtMn}) + 4215(X_{GtCa})(X_{GtMg} - X_{GtFe})\} + 4441(2X_{BtMg} - 1)]/[13.138 + 8.3143\ InK_D + 6.276(X_{GtCa})(1 - X_{GtMn})]$$ (Bhattacharya et al., 1992)

"HW" means that the thermodynamic model is based on Hackler and Wood (1989) (Bhattacharya et al., 1992). Figure 62 shows the results of the calculation with 6 kbar for the 9

analysis points at 3 sites of the section. 6 kbar were chosen following Schuster et al. (2004) for the greenschist to amphibolite facies conditions of the Miocene metamorphic event. It is to note that in total 12 pairs of points were measured, but at three of them the values for Mg in biotite respectively in garnet were 0, so the formula could not be used to avoid division by 0. The data show a clear plateau at 400°, which is also near the median (398 °C) and the mean value (390 °C). This corresponds to greenschist facies conditions and is significantly lower than the 550-600 °C and 6.5-10.3 kbar reported from the Alpeiner Scharte (Langthaler et al., 2004; Melcher et al., 1996). This difference could be explained by a more S position of the Alpeinerscharte, as the metamorphic gradient is N-S directed from greenschist to amphibolite facies (Schuster et al., 2004). Another explanation are the low Mg contents of garnet rarely exceeding 0.2 atoms per formula unit. At such low values, the relative error is large resulting in a high uncertainty of the temperature mainly dependent on the Mg content. To conclude, at least upper greenschist facies conditions were reached by the last thermal event forming the examined garnets.

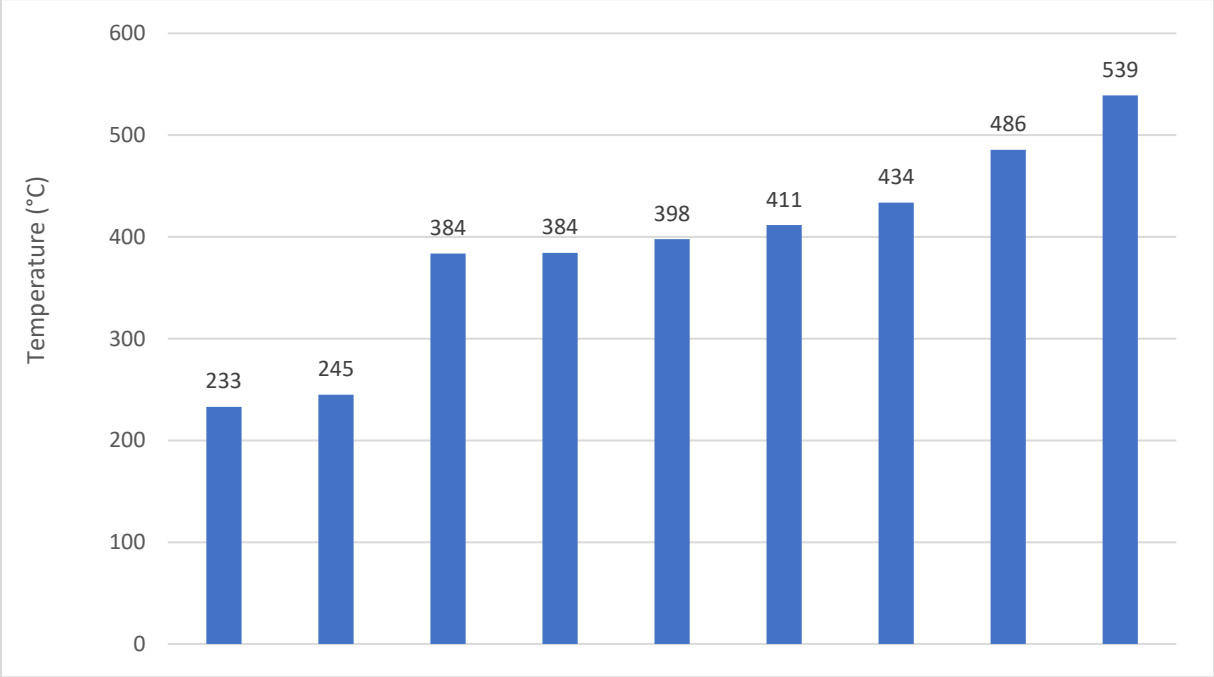

Figure 62: Diagram of yielded temperatures in the order of the temperature.

5.2 Geotectonic setting

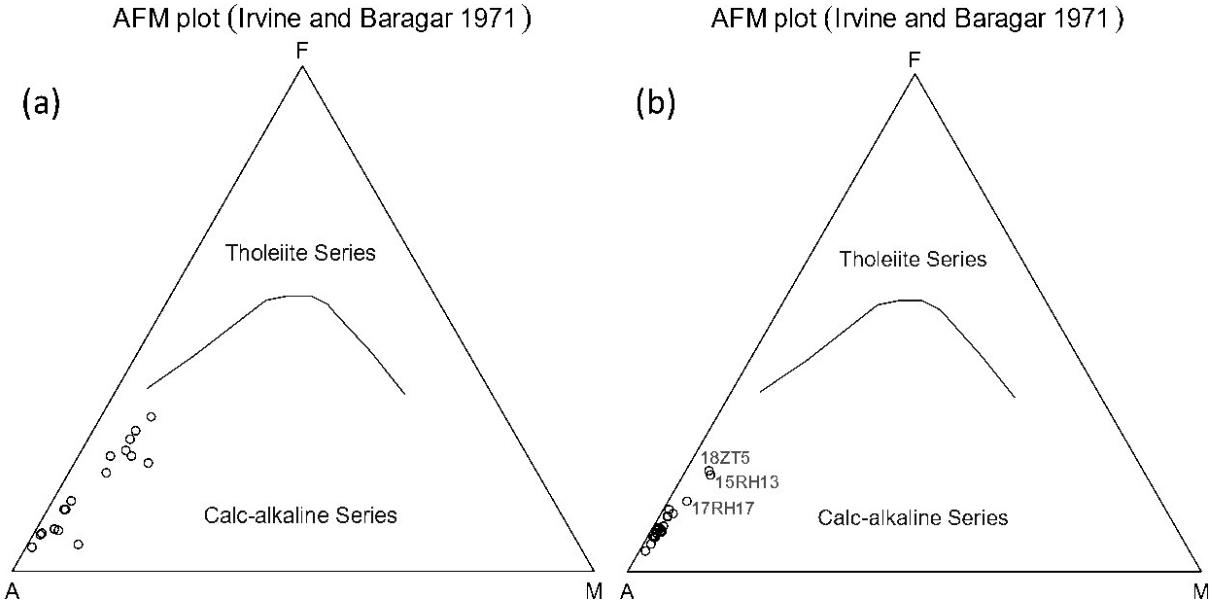

Figure 63: AFM diagrams; a: gneisses, b: aplitic granites (Irvine and Baragar, 1971).

The gneisses are calk-alkaline to high-K-calc-alkaline (Figures 63a and 65a) and mostly peraluminous (Figure 64a). The frequent mafic enclaves point to magma mingling with M-type melts (Vigneresse, 2004) and assimilation of wall-rocks (Lammerer, 1986). However, the enclaves have not been analyzed. The aplitic granites are high-K-calc-alkaline (Figures 63b and 65b), peraluminous (Figure 64b) and show a noticeably smaller scatter than the gneisses for all data. The aplitic granites were classified as A-type (Schermaier, 1993).

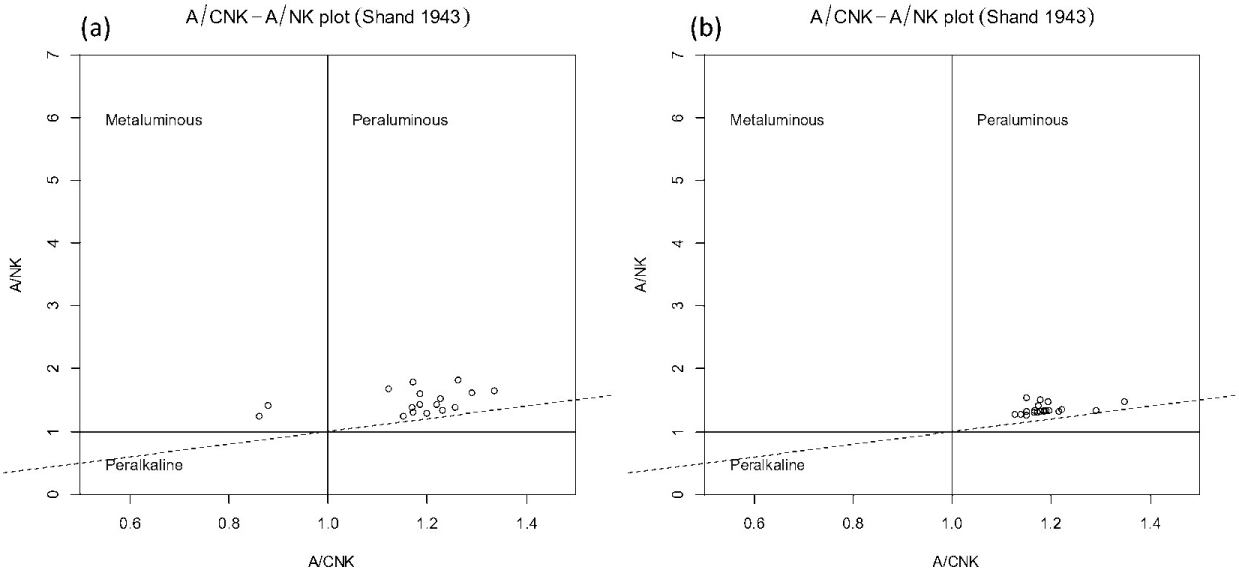

Figure 64: Classification after Shand (1943); a: gneisses, b: aplitic granites.

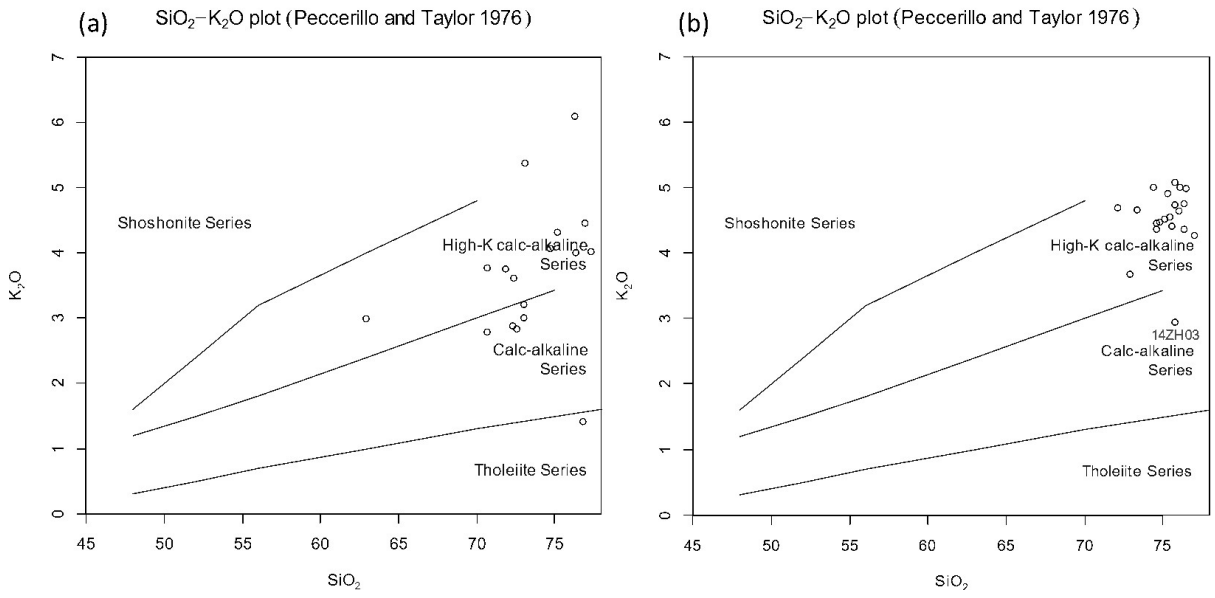

Figure 65: Classification after Peccerillo and Taylor (1976); a: gneisses, b: aplitic granites.

Following the classification after Batchelor and Bowden (1985), the gneisses are classified as mantle fractionates (Figure 66a) and the aplitic granites as post-orogenic melts (Figure 66b). Hence the gneisses could be classified as former I-type granites in accordance with other workers (Finger et al., 1997, 1993; Schermaier, 1993). On the other hand, the gneisses are classified following Chappell and White (2001, 1974) and Shand (1943) as S-type, or at least mixed with S-type melts. The best explanation, also brought up by Finger et al. (1993) with other arguments and supported by the review of Barbarin (1999), is magma mixing. In this model, the major part of the magma volume would have an igneous origin, which is modified by small batches of S-type magmas. This is also a suitable explanation for observed lateral changes within the gneisses, which were not significant enough to map. The classification of the aplitic granites as post-orogenic calc-alkaline is confirmed by the plot after Harris et al. (1986) shown in Figure 67a (Group 3 = post-orogenic calc-alkaline). Two samples, 17PH01 and 17PH10, are close to the border of the field with syn-orogenic melts (Group 2).

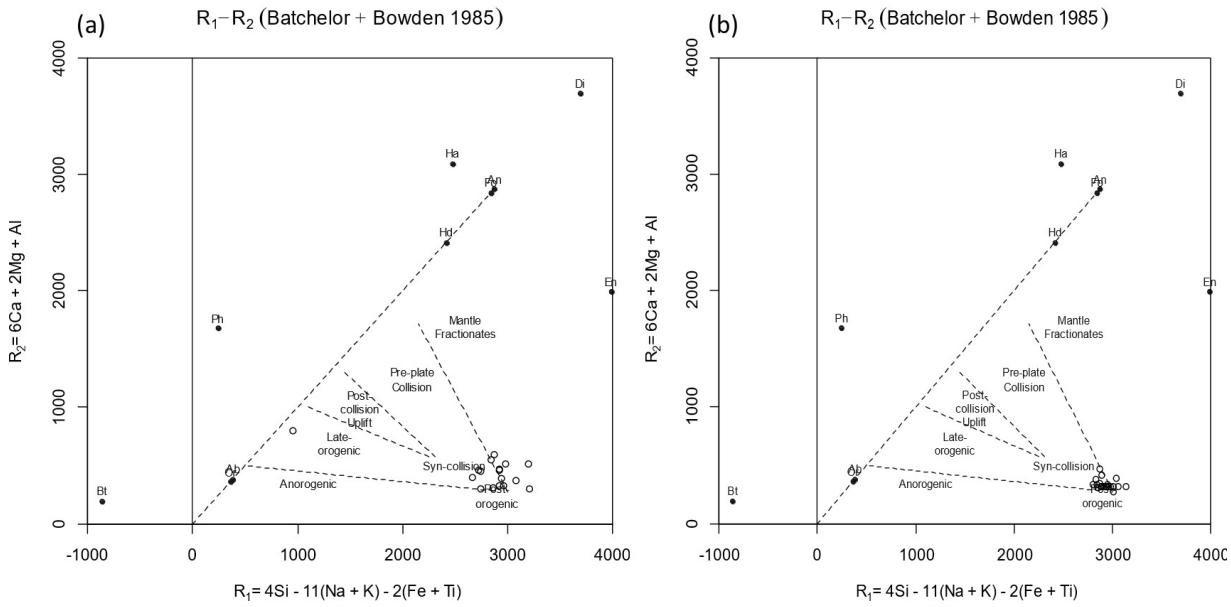

Figure 66: (a) R_1-R_2 plot (Batchelor and Bowden, 1985); a: gneisses, b: aplitic granites.

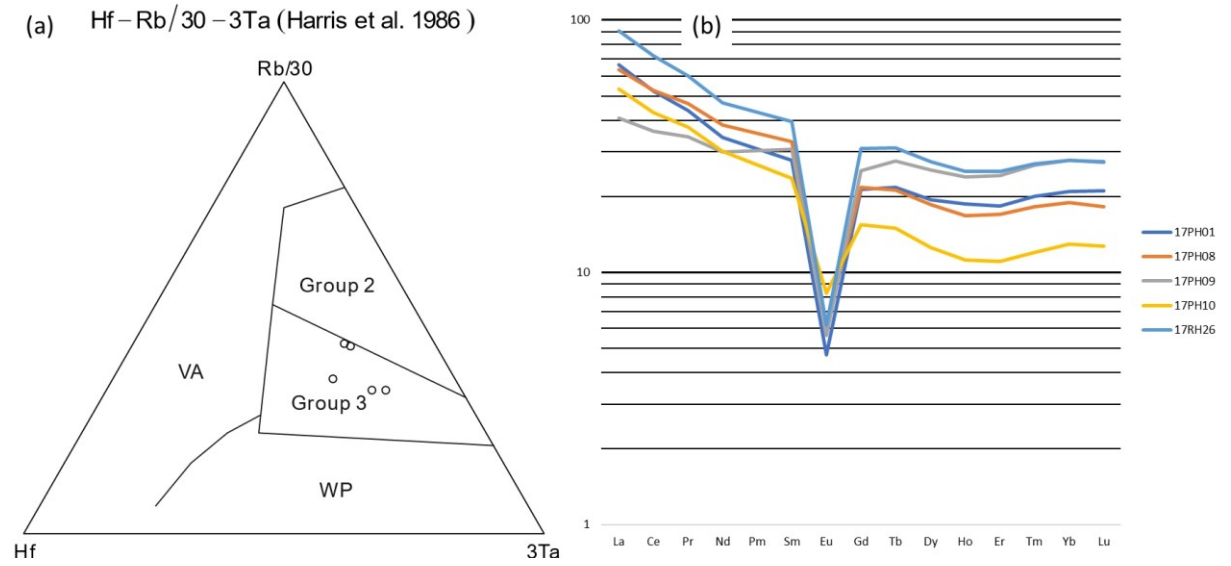

Figure 67: (a) Geotectonic classification after Harris et al. (1986); (b) Chondrite-normalized REE pattern of the five samples measured with ICP-MS

Figure 68 shows a diagram used by Haunschmid et al. (1991). They describe the A-type granites in the Hohe Tauern Batholith as having "much higher Rb/Sr rations than the felsic I-type granites (>1.4; <0.5)" and "significantly higher in Y (30-60; <20 ppm)". Generally, this can also be observed in this sample set. Examining the REE patterns of the aplitic granites (Figure 67b) also yields the same result since they are very similar to the ones published by Haunschmid et al. (1991). They are characterized by an enrichment of light REE and distinctive negative Eu anomaly, the latter indicating an early crystallization in a magma chamber with a subsequent plagioclase loss. To conclude, the gneiss can be classified as contaminated I-type and the aplitic granite as A-type. Having a strongly calc-alkaline character, the mineralization belongs to the calc-alkaline stockwork molybdenum deposit type of (Westra and Keith, 1981).

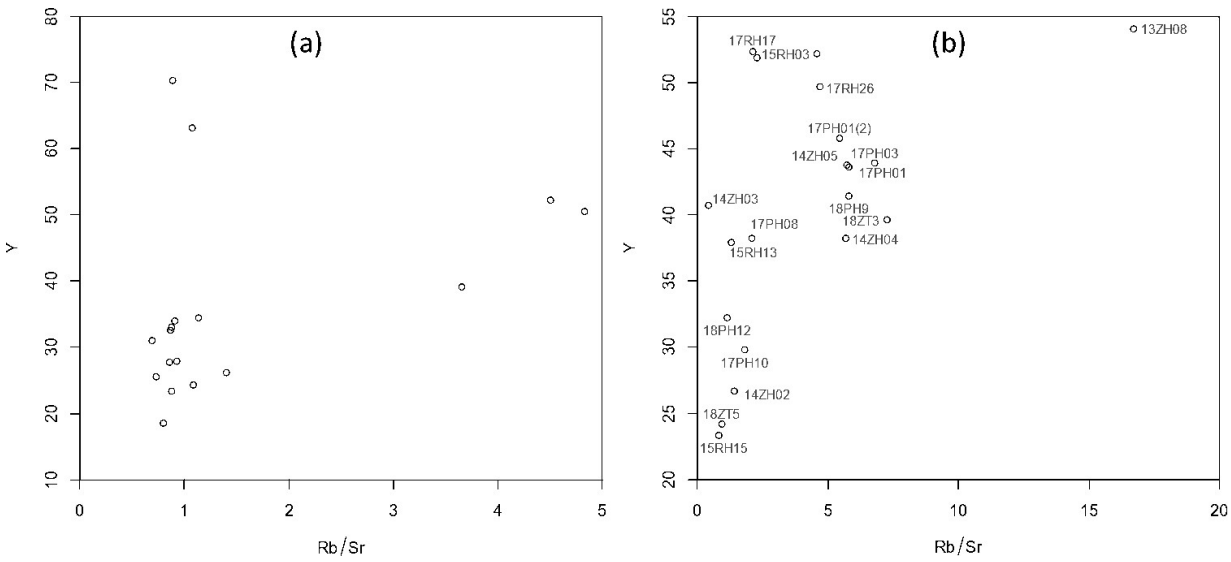

Figure 68: Rb-Sr-Y diagram; a: a: gneisses, b: aplitic granites. Note different axis labeling.

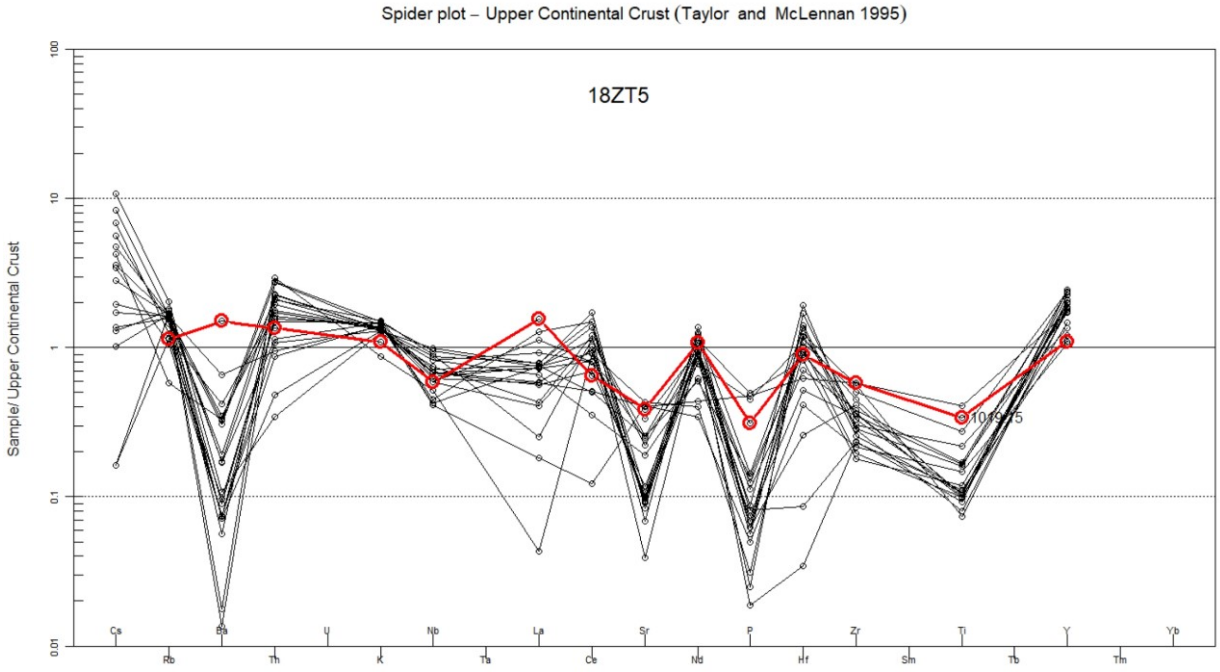

Figure 69: Spider diagram of the aplitic granites normalized to upper continental crust (Taylor and McLennan, 1995). The red marked sample is 18ZT5.

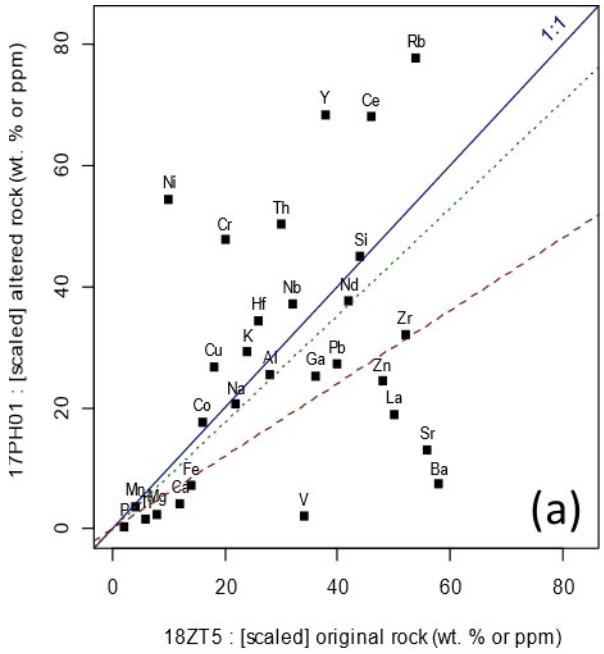
17PH01 : [scaled] altered rock (wt. % or ppm)
18ZT5 : [scaled] original rock (wt. % or ppm)
1:1
(a)
Rb
Y
Ce
Ni
Th
Cr
Si
Nb
Nd
Hf
Zr
K
Cu
Al
Ga
Pb
Zn
Na
La
Co
Sr
Fe
Ba
V
Mn
Ca
Mg
Ti
P

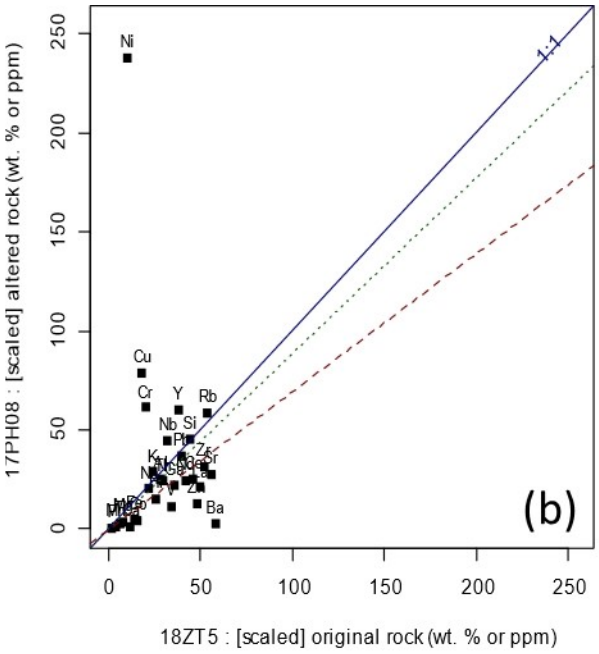
17PH08 : [scaled] altered rock (wt. % or ppm)
18ZT5 : [scaled] original rock (wt. % or ppm)
1:1
(b)
Ni
Cu
Cr
Y
Rb
Nb
Si
Pb
Ba

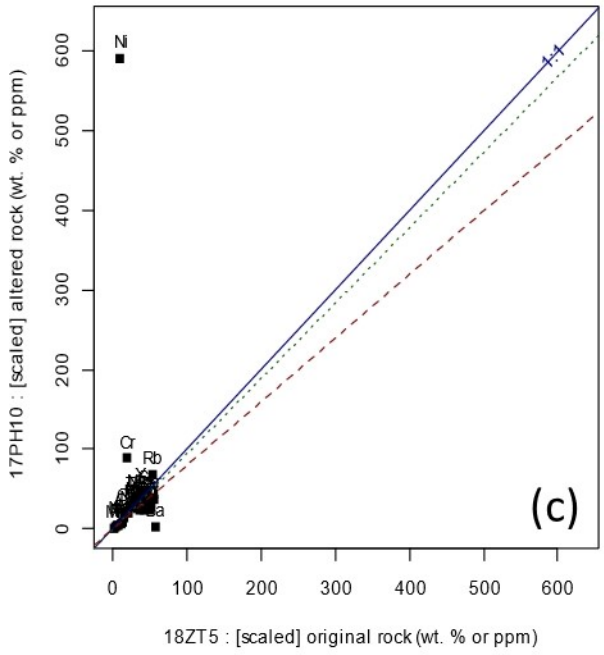
17PH10 : [scaled] altered rock (wt. % or ppm)
18ZT5 : [scaled] original rock (wt. % or ppm)
1:1
(c)
Ni
Cr
Rb
Ga

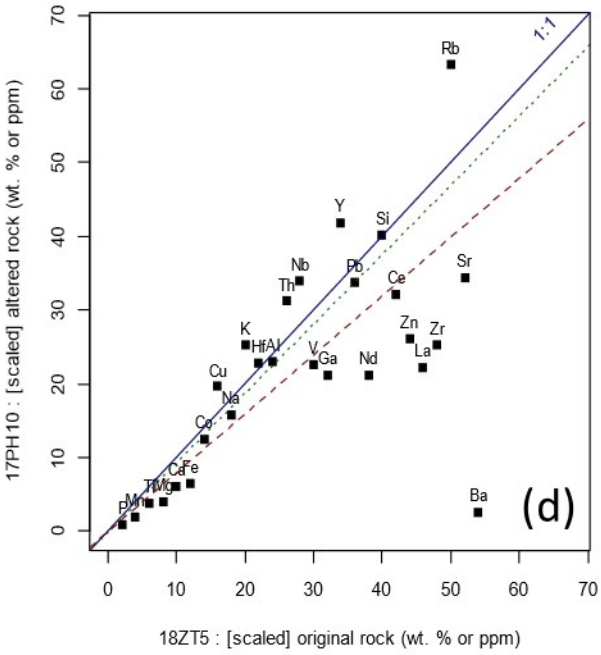
17PH10 : [scaled] altered rock (wt. % or ppm)
18ZT5 : [scaled] original rock (wt. % or ppm)
1:1
(d)
Rb
Y
Si
Nb
Pb
Sr
Th
Ce
K
Zn
Zr
Hf
Al
V
Ga
La
Nd
Cu
Na
Co
Ca
Fe
Ba
Mn
Ti
Mg
P

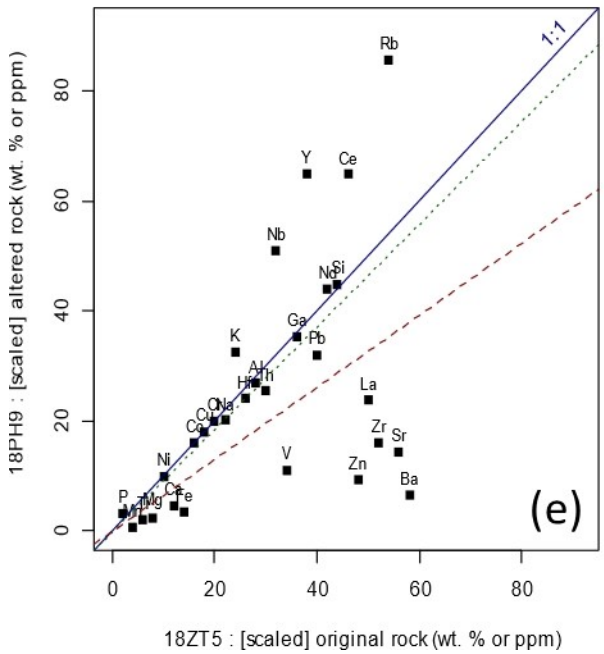
18PH9 : [scaled] altered rock (wt. % or ppm)
18ZT5 : [scaled] original rock (wt. % or ppm)
1:1
(e)
Rb
Y
Ce
Nb
Si
Nd
Ga
K
Pb
Al
Th
Hf
La
Na
Cu
Co
Zr
Sr
Ni
V
Zn
Ba
Ce
Fe
Mg
P

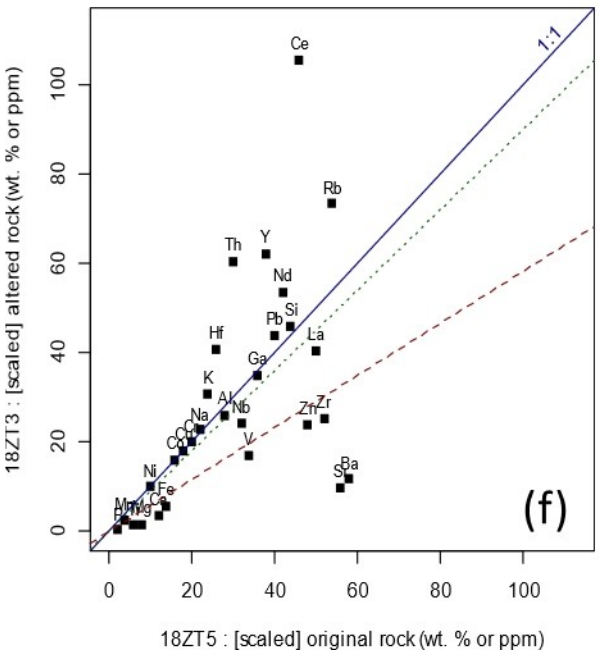
18ZT3 : [scaled] altered rock (wt. % or ppm)
18ZT5 : [scaled] original rock (wt. % or ppm)
1:1
(f)
Ce
Rb
Th
Y
Nd
Si
Pb
Hf
La
Ga
K
Al
Na
Nb
Zn
Zr
V
Ni
Ba
Fe
Mn
Mg

Figure 70 (previous page): Isocon diagrams of 17PH01 (a), 17PH08 (b), 17PH10 (c), 17PH10 without Ni and Cr (d), 18PH9 (e) and 18ZT3 (f). Plotted elements: SiO2, Al2O3, Fe2O3, CaO, MgO, Na2O, K2O, TiO2, MnO, P2O5, Sc, V, Cr, Co, Ni, Cu, Zn, Ga, Rb, Sr, Y, Zr, Nb, Cs, Ba, La, Ce, Nd, Hf, Pb and Th. Green lines are Al = constant isocons, red lines are Ti = constant isocons.

5.3 Mineralization geochemistry

Of the aplitic granites, 18ZT5 is least evolved (Figures 69, 68b and 63b) and therefore suited as a reference sample to study the mineralization and the magmatic evolution of the aplitic granites. Isocon diagrams are well suited for this purpose, as they provide a graphic inter-sample comparison without modifying the data (Grant, 1986). An isocon is a line of equal mass or volume, everything that plots above is enriched and vice versa (Grant, 1986). Al and Ti were chosen to form the reference isocon as no data on rock densities are available. Figure 70 shows isocon diagrams with the reference sample 18ZT5. 17PH10 was plotted twice to avoid extreme scaling caused by a comparatively high Ni content. All chosen samples contained molybdenite, which was excluded from the isocon plots for a better visibility of the other elements. Together with Mo, the elements Ni, Cu, Y, Rb, K, Th, Ce and Nb are enriched, while Ba, Sr and La are depleted in the mineralized samples. Note, that 18ZT5 has a very low Ni content resulting in an apparent Ni enrichment in the other samples. There is no depletion of Ca as this is not part of the mineralization but an effect of the Alpine metamorphism. Mo, Cu, Y, Ce, Th and Nb bearing minerals were identified in the mineralogy section. Those are incompatible elements. For comparison also isocon diagrams within an already highly fractionated zone were made (Figure 71) to characterize the mineralization. At the N-Zillerscharte three samples were taken within 20 m from unaltered aplitic granite to a mineralized shear zone. 17PH10 is the unaltered sample, 17PH08 is directly in the shear zone and 17PH09 is in between. The diagrams show an enrichment of REE, U and Ni, while V, Ca, Pb and Li are depleted. This fits with the microscopic evidence, as the enriched elements correspond to the frequently observed allanite/epidote-zircon-thorite assemblage (Chapter 4.5.16), which is associated with the mineralization. Elevated Ni could have been mobilized from Ni-bearing pyrrhotite or pentlandite. As Li is an incompatible element, it is likely, that it was removed by a high fluid flow in the shear zone. Vanadium loss can be explained by rutile breakdown in the shear zone. The enrichment patterns are similar to those observed during magmatic fractionation as REE and high field strength elements – incompatible elements – are enriched.

To conclude, it is likely, that the mineralization formed during a late cooling stage of the intrusion of the aplitic granites. This is supported by the fractionation trend pointing towards the mineralization and the enrichment of REE and U in the mineralized zones in comparison with the direct surroundings.

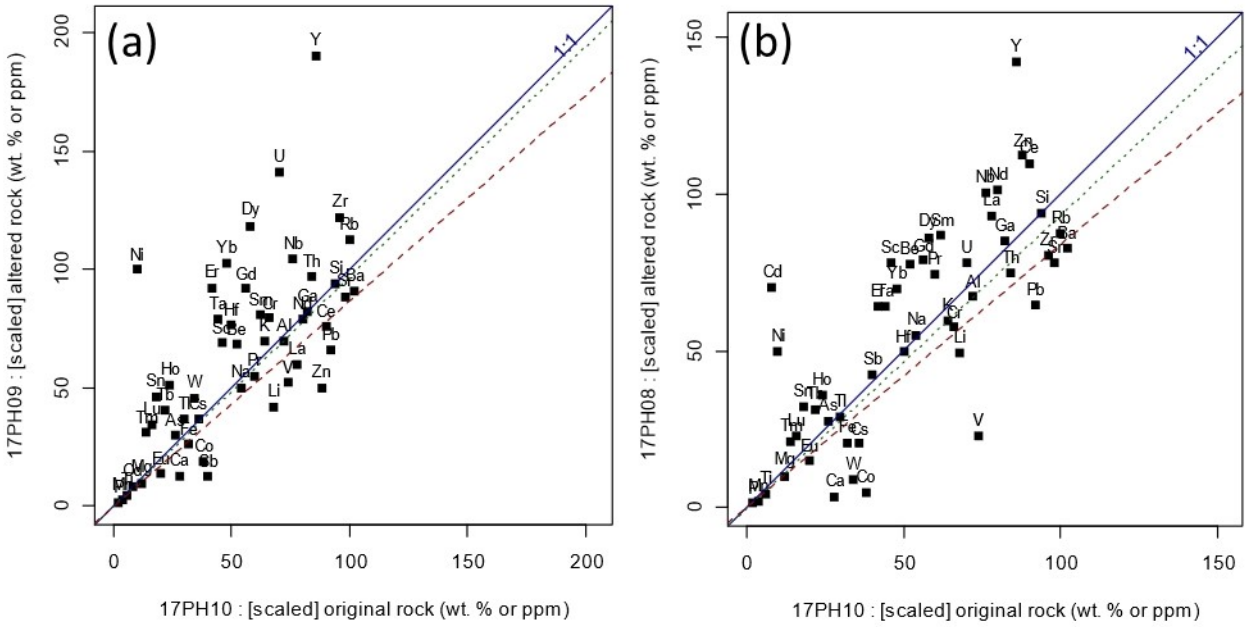

Figure 71: Isocon diagrams of 17PH09 (a) and 17PH08 (b) compared with 17PH10. Plotted elements are: SiO_2, Al_2O_3, Fe_2O_3, CaO, MgO, Na2O, K2O, TiO_2, MnO, P_2O_5, LOI, Li, Be, Sc, V, Cr, Co, Ni, Zn, Ga, As, Rb, Sr, Y, Zr, Nb, Cd, Sn, Sb, Cs, Ba, La, Ce, Pr, Nd, Sm, Eu, Gd, Tb, Dy, Ho, Er, Tm, Yb, Lu, Hf, Ta, W, Tl, Pb, Th and U. All samples contained Mo and Cu, which were excluded to enhance visibility of the other elements. Green lines are Al = constant isocons, red lines are Ti = constant isocons.

5.4 Comparison with the Alpeiner Scharte Mo deposit

The Alpeiner Scharte Mo deposit is located 30 km W of the Reichenspitzgruppe, also in the Tux core (Melcher et al., 1996). It is one of several Variscan vein type Mo deposits in the Alpine realm, another well-known is in the Aar massif (Steck and Hügi, 1970). The host rocks are I-type granites with an S-type affinity but have not been classified as A-type granites (Melcher et al., 1996). Even the enriched elements are very similar to the results of the present study: Mo, Cu, Cr, Nd, MgO, MnO, Fe_2O_3, Zn, Sc, Ce, Co, Cs, W, Th, and most of the REEs with the first three extremely enriched and a depletion of Pb, Sr, Ba and Na_2O (Melcher et al., 1996). Garnet found in the gneisses by Melcher et al. (1996) yields similar compositions as in the Reichenspitzgruppe, but higher formation conditions when coexisting with biotite in quartz vein selvages (550-600°C, Langthaler et al., 2004). Re-Os dating of molybdenite at the Alpeiner Scharte yielded 306.8 ± 3.1 Ma (Upper Carboniferous, Langthaler et al., 2004).

Molybdenite is restricted to quartz veins in this gneiss (Langthaler et al., 2004; Melcher et al., 1996). The quartz veins comprise of mainly quartz with biotite and garnet at the rims and molybdenite flakes (Melcher et al., 1996). In the Reichenspitz area, the veins contain quartz, molybdenite and muscovite, and molybdenite occurs also disseminated in the gneiss and aplite.

The origin of the Reichenspitz mineralization and the Alpeiner Scharte deposit is in both cases related to late Variscan extension leading to intrusions. However, a genetic link between the A-

type granites and the calc-alkaline rocks was excluded by Schermaier (1993), and the geochemical data show pronounced differences. Therefore, a common magma source is unlikely. The similar garnet compositions are explained by thermodynamic equilibria and similar whole rock chemistry. The similar enrichment patterns of incompatible elements seem to be typical for porphyries (Westra and Keith, 1981).

5.5 Comparison with other Molybdenum deposits

Most magmatic Mo deposits are classical porphyries with pyrite and chalcopyrite being major ore minerals. Therefore, the interpretation of the Reichenspitze mineralization as porphyry style is problematic. However, there is Su Seinargiu in Sardinia to compare. Su Seinargiu is the type locality of ichnusaite (Orlandi et al., 2014) and suseinargiuite (Orlandi et al., 2015b) and still the only published occurrence, of many minerals that were also observed in this study. Su Seinargiu is a late Variscan intrusion with a porphyry style Mo mineralization with molybdenite as sole ore mineral and only little pyrite (Boni et al., 2003; Caboi et al., 1978; Orlandi et al., 2014). Boni et al. (2003) compare the Su Seinargiu deposit with Climax-type Mo-porphyry deposits. Even though Schermaier (1993) reported fluorite in the aplitic granites, their F content is far too low to consider the Reichenspitz mineralization as Climax-type (Ludington and Plumlee, 2009). Similar to the Climax-type, but with lower contents of F, Sn and W are low fluorine porphyry molybdenum deposits with Endako (British Columbia, Canada) as a typical example (Selby et al., 2000; Selby and Creaser, 2001). Endako is also classified as calc-alkaline molybdenum stockwork deposit (Westra and Keith, 1981). These porphyry deposits are hosted by granites to aplitic granites and yield a pervasive alkali metasomatism expressed as K-feldspar veins in the orebody and the surroundings (Selby et al., 2000; Selby and Creaser, 2001). This is not observed at the Reichenspitze mineralization, but ore grades seem to be much lower there pointing to less initial alteration which was also overprinted by several metamorphic events. Therefore it is not surprising, that there are no obvious signs of an alkali metasomatism, although it is to note, that Karl (1962) suggested an alkali metasomatism originating from the Reichenspitze aplitic granite. Ore mineralogy, mainly molybdenite with some pyrite and traces of bismuthinite, scheelite, beryl, specularite and galena (Selby et al., 2000), is very similar to the observations in the Reichenspitz area.

The occurrence of molybdenite as impregnations rather than veinlets in many cases makes the Reichenspitze mineralization unique amongst other Mo deposits in the Tauern Window. This can be explained by the rather small grade of the mineralization. The polymetamorphic history of the mineralization can explain the occurrence of many exotic Bi and Mo minerals. Therefore,

it can be concluded, that the Reichenspitze Mo mineralization is a polymetamorphic low-grade, low fluorine calc-alkaline Molybdenum porphyry. With these characteristics, it is classified in this thesis as aplite hosted Reichenspitz-type molybdenite mineralization. It is to be questioned, if this type can also produce economic deposits, but Su Seinargiu and Endako would be well-suited candidates for further studies.

5.6 Conclusions

Mainly based on the results of the fieldwork, microscopic and SEM analysis the following order of events is proposed:

1. Variscan orogeny: Metamorphism of pre-Variscan sediments and intrusion of the Tauern Batholith, which is present as granitic orthogneiss in the working area.
2. Late- to post Variscan orogeny: Intrusion of the aplitic granite at 282±6 Ma (Rb/Sr age, Besang et al., 1968) and subsequent formation of the molybdenite (+pyrite+chalcopyrite+Bi-minerals+REE bearing minerals as minor components) assemblage in the pneumatolytic stage of the intrusion. Most zircon present in the samples crystallized during the cooling of the magma including U and Th.
3. Intrusion of mafic dykes: unknown timing, the intruded crust was already brittle.
4. Triassic extension: Crystallization of uraninite (Finger et al., 2017).
5. Tauernkristallisation: Metamorphism reaching at least upper greenschist facies with remobilization leading to the formation of the allanite/epidote-zircon-thorite assemblage (Chapter 4.5.16). Zircon and thorite were probably not remobilized and acted as a geochemical trap for the other minerals. Remobilization of minor molybdenite, U-Th and Bi at few places leading to the formation of molybdenite-quartz veins, Mo-minerals and sulfosalts. This is probably related to extension with enhanced fluid flow and faulting. Hence, it can be concluded, that this happened at an early stage of the exhumation of the Tauern Window. As a result of the N-S directed metamorphic gradient, plagioclase experienced intense saussuritisation following this gradient.
6. Late Alpine orogeny: Regional extension with the formation of the Alpine mineralized veins, due to already low temperatures no molybdenite, but only minor hydrothermal pyrrhotite and pyrite formed. At this stage, the REE minerals were overprinted (Uher et al., 2015) leading to the formation of calcite. Even later, oxidized fluids caused pervasive oxidation along existing paths – as the Alpine mineralized joints are comparatively resistant to alteration, this affected mainly the fluid paths related to the

molybdenite mineralization resulting in the formation of FeOx rims of calcite and the sulfides.

6 Summary and Outlook

The aplite hosted Reichenspitz-type Mo mineralization at the Reichenspitze is a low-grade, low fluorine calc-alkaline molybdenum porphyry with special mineralogy and unique structures. As in other similar porphyries, it is likely, that similar mineralized intrusions occur nearby. In this context, particularly the Alpeiner Scharte, and the area to the W of the working area should be mentioned. In the former, some slope debris rocks with a polymetallic assemblage are known (Mostler et al., 1982). From the latter, one sample (18PH12) containing molybdenite in an aplitic dyke was collected. The aplitic granites were dated with Rb/Sr, a method sensitive to metamorphic overprinting. Hence they and the hosting gneisses should be redated with a more robust method. As Finger et al. (2017) only believed to date the same aplitic granite as present at the Reichenspitze (Reichenspitzgranit; Schermaier, 1993), follow up work should date uraninite present in the samples examined by the SEM. Also, it is necessary to date molybdenite and possibly also secondary Mo minerals to confirm the metallogenetic model. From the currently available data, it cannot be recommended to conduct exploration work on the Reichenspitz mineralization as it is located in the Nationalpark Hohe Tauern, in rugged high-alpine terrain and total resources seem to be rather small as outcrops with a high molybdenite abundance are scarce.

7 References

Allmendinger, R.W., Cardozo, N., Fisher, D.M., 2011. Structural geology algorithms: Vectors and tensors. Cambridge University Press.

Anonymus, 1943. Betriebsplan des Bergbaues Alpeinerscharte der Tiroler Erzbergbaugesellschaft mbH., ST.JODOK.

Barbarin, B., 1999. A review of the relationships between granitoid types, their origins and their geodynamic environments. Lithos 46, 605–626. https://doi.org/10.1016/S0024-4937(98)00085-1

Batchelor, R.A., Bowden, P., 1985. Petrogenetic interpretation of granitoid rock series using multicationic parameters. Chemical Geology 48, 43–55. https://doi.org/10.1016/0009-2541(85)90034-8

Besang, C., Harre, W., Karl, F., Kreuzer, H., Lenz, H., Müller, P., Wendt, I., 1968. Radiometrische Altersbestimmungen (Rb/Sr und K/Ar) an Gesteinen des Venediger-Gebietes (Hohe Tauern, Österreich). Geol. Jb 86, 835–844.

Bhattacharya, A., Mohanty, L., Maji, A., Sen, S.K., Raith, M., 1992. Non-ideal mixing in the phlogopite-annite binary: constraints from experimental data on Mg−Fe partitioning and a reformulation of the biotite-garnet geothermometer. Contrib Mineral Petrol 111, 87–93. https://doi.org/10.1007/BF00296580

Boni, M., Stein, H.J., Zimmerman, A., Villa, I.M., 2003. Re-Os age for molybdenite from SW Sardinia (Italy): A comparison with 40Ar/39Ar dating of Variscan granitoids. Mineral exploration and sustainable development. Millpress, Rotterdam 247–250.

Burgsteiner, E., 2017. Sardignait - Erstfund für Österreich! Der Aufschluss 155–157.

Caboi, R., Massoli-Novelli, R., Sanna, G., 1978. La mineralizzazione a molibdenite di P.ta de Su Seinargiu (Sarroch – Sardegna meridionale). Rendiconti della Società Italiana di Mineralogia e Petrologia 34, 167–186.

Cardozo, N., Allmendinger, R.W., 2013. Spherical projections with OSXStereonet. Computers & Geosciences 51, 193–205. https://doi.org/10.1016/j.cageo.2012.07.021

Chappell, B.W., White, A.J., 2001. Two contrasting granite types: 25 years later. Australian Journal of Earth Sciences 48, 489–499.

Chappell, B.W., White, A.J.R., 1974. Two contrasting granite types. Pacif. Geol. 8, 173–174.

Christensen, J.N., Selverstone, J., Rosenfeld, J.L., DePaolo, D.J., 1994. Correlation by Rb-Sr geochronology of garnet growth histories from different structural levels within the Tauern Window, Eastern Alps. Contributions to Mineralogy and Petrology 118, 1–12.

Eichhorn, R., Loth, G., Höll, R., Finger, F., Schermaier, A., Kennedy, A., 2000. Multistage Variscan magmatism in the central Tauern Window (Austria) unveiled by U/Pb SHRIMP zircon data. Contributions to Mineralogy and Petrology 139, 418–435.

Exner, C., Faupl, P., 1970. Die Anorthitgehalte der Plagioklase in einigen Gesteinsgruppen der zentralen Ostalpen. Verh. Geol. BA 245–266.

Finger, F., Frasl, G., Haunschmid, B., Lettner, H., von Quadt, A., Schermaier, A., Schindlmayr, A.O., Steyrer, H.P., 1993. The Zentralgneise of the Tauern Window (eastern Alps): insight into an intra-Alpine Variscan batholith, in: Pre-Mesozoic Geology in the Alps. Springer, pp. 375–391.

Finger, F., Roberts, M.P., Haunschmid, B., Schermaier, A., Steyrer, H.P., 1997. Variscan granitoids of central Europe: their typology, potential sources and tectonothermal relations. Mineralogy and Petrology 61, 67–96.

Finger, F., Waitzinger, M., Förster, H.J., Kozlik, M., Raith, J.G., 2017. Identification of discrete low-temperature thermal events in polymetamorphic basement rocks using high spatial resolution FE-SEM-EDX U-Th-Pb dating of uraninite microcrystals. Geology 45, 991–994.

GBA: IRIS - Interaktives RohstoffInformationsSystem [WWW Document], 2018. URL https://www.geologie.ac.at/services/webapplikationen/iris-interaktives-rohstoffinformationssystem/ (accessed 10.19.18).

Grant, J.A., 1986. The isocon diagram; a simple solution to Gresens' equation for metasomatic alteration. Economic Geology 81, 1976–1982. https://doi.org/10.2113/gsecongeo.81.8.1976

Hackler, R., Wood, B., 1989. Experimental-determination of Fe and Mg exchange between garnet and olivine and estimation of Fe-Mg mixing properties in garnet. American Mineralogist 74, 994–999.

Harris, N.B.W., Pearce, J.A., Tindle, A.G., 1986. Geochemical characteristics of collision-zone magmatism. Geological Society, London, Special Publications 19, 67–81. https://doi.org/10.1144/GSL.SP.1986.019.01.04

Haunschmid, B., Schermaier, A., Finger, F., 1991. Late-stage A-type granite intrusions in the Variscan Hohe Tauern I-type batholite (Eastern Alps, Austria). Berichte der deutschen mineralogischen Gesellschaft.

Höll, R., Eichhorn, R., 2000. Tungsten mineralization and metamorphic remobilization in the Felbertal scheelite deposit, Central Alps, Austria. Chapter 11, 233–264.

Irvine, T.N., Baragar, W.R.A., 1971. A Guide to the Chemical Classification of the Common Volcanic Rocks. Can. J. Earth Sci. 8, 523–548. https://doi.org/10.1139/e71-055

Janoušek, V., Farrow, C.M., Erban, V., 2006. Interpretation of Whole-rock Geochemical Data in Igneous Geochemistry: Introducing Geochemical Data Toolkit (GCDkit). J Petrology 47, 1255–1259. https://doi.org/10.1093/petrology/egl013

Karl, F., 1964. Bericht 1963 über Aufnahmen auf Blatt Krimml (151/1) und Blatt Rötspitze (151/3). Verhandlungen der Geologischen Bundesanstalt.

Karl, F., 1963. Bericht 1962 über Aufnahmen auf Blatt Fürlegg (152/1), Wald (151/2) Rötspitze (151/3), Blatt Krimml (151). Verhandlungen der Geologischen Bundesanstalt.

Karl, F., 1962. Bericht 1961 über Aufnahmen auf dem Blatt Krimml (151). Verhandlungen der Geologischen Bundesanstalt.

Karl, F., 1961. Bericht 1960 über Aufnahmen auf dem Blatt Krimml (151). Verhandlungen der Geologischen Bundesanstalt.

Karl, F., Schmidegg, O., 1979. Geologische Karte der Republik Österreich 1:50.000 151 Krimml.

Kozlik, M., 2015. Mineralogical, petrological and (isotope-) geochemical studies on the Felbertal scheelite deposit, Austria: Development of an epigenetic model for W mineralization in the context of Variscan magmatism in the Tauern Window. Montanuniversität Leoben, Leoben.

Kozlik, M., Raith, J.G., Gerdes, A., 2016b. U–Pb, Lu–Hf and trace element characteristics of zircon from the Felbertal scheelite deposit (Austria): New constraints on timing and source of W mineralization. Chemical Geology 421, 112–126.

Lammerer, B., 1986. Das Autochthon im westlichen Tauernfenster. Jahrbuch der Geologischen Bundesanstalt 129, 51–67.

Langthaler, K.J., Raith, J.G., Cornell, D.H., Stein, H.J., Melcher, F., 2004. Molybdenum mineralization at Alpeiner Scharte, Tyrol (Austria): results of in-situ U–Pb zircon and Re–Os molybdenite dating. Mineralogy and Petrology 82, 33–64.

Ludington, S., Plumlee, G.S., 2009. Climax-Type Porphyry Molybdenum Deposits (USGS Numbered Series No. 2009–1215), Open-File Report. U.S. Geological Survey.

Meixner, H., 1952. Über einige typomorphe Minerale aus den Ostalpen. Geologie 1, 197–200.

Melcher, F., Prochaska, W., Raith, J.G., Saini-Eidukat, B., 1996. The metamorphosed molybdenum vein-type deposit of the Alpeinerscharte, Tyrol (Austria) and its relation to Variscan granitoids. Mineralium Deposita 31, 277–289.

Middlemost, E.A.K., 1994. Naming materials in the magma/igneous rock system. Earth-Science Reviews 37, 215–224. https://doi.org/10.1016/0012-8252(94)90029-9

Mostler, H., Heissel, G., Gasser, G., 1982. Untersuchung von Erzlagerstätten im Innsbrucker Quarzphyllit und auf der Alpeiner Scharte. Archiv für Lagerstättenforschung der geologischen Bundesanstalt 1, 77–83.

Muskid, 2018. CC BY-SA 4.0, https://commons.wikimedia.org/w/index.php?curid=46491727 visited 20.10.2018, 20:40.

Orlandi, P., Biagioni, C., Bindi, L., Merlino, S., 2015a. Nuragheite, Th(MoO4)2·H2O, the second natural thorium molybdate and its relationships to ichnusaite and synthetic Th(MoO4)2. American Mineralogist 100, 267–273. https://doi.org/10.2138/am-2015-5024

Orlandi, P., Biagioni, C., Bindi, L., Nestola, F., 2014. Ichnusaite, Th(MoO4)2·3H2O, the first natural thorium molybdate: Occurrence, description, and crystal structure. American Mineralogist 99, 2089–2094. https://doi.org/10.2138/am-2014-4844

Orlandi, P., Biagioni, C., Moëlo, Y., Langlade, J., Faulques, E., 2015b. Suseinargiuite, (Na0.5Bi0.5)MoO4, the Na-Bi analogue of wulfenite, from Su Seinargiu, Sardinia, Italy. European Journal of Mineralogy 27, 695–699. https://doi.org/10.1127/ejm/2015/0027-2463

Orlandi, P., Pasero, M., Bigi, S., 2010. Sardignaite, a new mineral, the second known bismuth molybdate: description and crystal structure. Miner Petrol 100, 17–22. https://doi.org/10.1007/s00710-010-0111-0

Paar, W.H., Günther, W., Gruber, F., 2006. Das Buch vom Tauerngold. Pustet.

Peccerillo, A., Taylor, S.R., 1976. Geochemistry of Eocene calc-alkaline volcanic rocks from the Kastamonu area, northern Turkey. Contributions to mineralogy and petrology 58, 63–81.

Schermaier, A., 1993. Gliederung der ´Zentralgneise im mittleren und westlichen Tauernfenster Geologie - Petrographie - Zirkontypologie - Geochemie. Salzburg, Salzburg.

Schmid, S.M., Fügenschuh, B., Kissling, E., Schuster, R., 2004. Tectonic map and overall architecture of the Alpine orogen. Eclogae geol. Helv. S.93–117.

Schmid, S.M., Scharf, A., Handy, M.R., Rosenberg, C.L., 2013. The Tauern Window (Eastern Alps, Austria): a new tectonic map, with cross-sections and a tectonometamorphic synthesis. Swiss J Geosci 106, 1–32. https://doi.org/10.1007/s00015-013-0123-y

Schmidegg, O., 1964. Geologische Aufnahmen 1963 auf Blatt Krimml 151 und Zell a. Z. 150. Verhandlungen der Geologischen Bundesanstalt.

Schuster, R., Koller, F., Hoeck, V., Hoinkes, G., Bousquet, R., 2004. Explanatory notes to the map: metamorphic structure of the Alps—metamorphic evolution of the Eastern Alps. Mitteilungen der Österreichischen Mineralogischen Gesellschaft 149, 175–199.

Selby, D., Creaser, R.A., 2001. Re-Os geochronology and systematics in molybdenite from the Endako porphyry molybdenum deposit, British Columbia, Canada. Economic Geology 96, 197–204.

Selby, D., Nesbitt, B.E., Muehlenbachs, K., Prochaska, W., 2000. Hydrothermal Alteration and Fluid Chemistry of the Endako Porphyry Molybdenum Deposit, British Columbia. Economic Geology 95, 183–202. https://doi.org/10.2113/gsecongeo.95.1.183

Shand, S.J., 1943. Eruptive rocks: their genesis, composition, classification, and their relation to ore deposits with a chaper on meteorites. London.

Steck, A., Hügi, T., 1970. Das Auftreten des Molybdänglanzes im westlichen Aarmassiv und Molybdängehalte von Gesteinen der gleichen Region. Schweizerische Mineralogische und Petrographische Mitteilungen 50, 257–265.

Streckeisen, A., 1976. To each plutonic rock its proper name. Earth-Science Reviews 12, 1–33. https://doi.org/10.1016/0012-8252(76)90052-0

Streckeisen, A., Le Maitre, R.W., 1979. A chemical approximation to the modal QAPF classification of the igneous rocks. Neues Jahrbuch für Mineralogie, Abhandlungen 136, 169–206.

Taylor, S.R., McLennan, S.M., 1995. The geochemical evolution of the continental crust. Reviews of Geophysics 33, 241–265.

Uher, P., Ondrejka, M., Bačík, P., Broska, I., Konečný, P., 2015. Britholite, monazite, REE carbonates, and calcite: Products of hydrothermal alteration of allanite and apatite in A-type granite from Stupné, Western Carpathians, Slovakia. Lithos 236–237, 212–225. https://doi.org/10.1016/j.lithos.2015.09.005

Veselá, P., Söllner, F., Finger, F., Gerdes, A., 2011. Magmato-sedimentary Carboniferous to Jurassic evolution of the western Tauern window, Eastern Alps (constraints from U-Pb zircon dating and geochemistry). International Journal of Earth Sciences 100, 993–1027.

Vigneresse, J.L., 2004. A new paradigm for granite generation. Earth and Environmental Science Transactions of the Royal Society of Edinburgh 95, 11–22.

Walter, F., Auer, C., Bernhard, F., Bojar, H.-P., Brandstätter, F., Habel, M., Hollerer, C.E., Kolitsch, U., Lamatsch, P., Leikauf, B., Löffler, E., Niedermayr, E., Postl, W., Putz, H., Reicht, M., Schachinger, T., Schillhammer, H., Taucher, J., 2016. Neue Mineralfunde aus Österreich LXV. Carinthia II 203–250.

Wang, X., Griffin, W.L., Chen, J., 2010. Hf contents and Zr/Hf ratios in granitic zircons. Geochem. J. 44, 65–72. https://doi.org/10.2343/geochemj.1.0043
Westra, G., Keith, S.B., 1981. Classification and genesis of stockwork molybdenum deposits. Economic Geology 76, 844–873.

Appendix

In this printed volume are only the sample list and a table of the major elements from the XRF analyses, the list of all SEM analyses and the complete chemical analyses are in the digital appendix.

Sample list

The column "Mol" indicates if molybdenite is present in the sample.

Sample	Mol	Rock type	Date	Thin section	N (WGS 84)	E (WGS 84)	Collector
13ZH01	Mol	Gneiss	30.08.2013	FM001			Melcher
13ZH02	Mol	Gneiss	30.08.2013	FM002			Melcher
13ZH03	Mol	Gneiss	30.08.2013	FM003			Melcher
13ZH04	Mol	Gneiss	30.08.2013	FM004			Melcher
13ZH05	Mol	Gneiss	30.08.2013	FM005			Melcher
13ZH06	Mol	Gneiss	30.08.2013	FM006			Melcher
13ZH07	Mol	Gneiss	30.08.2013	FM007			Melcher
13ZH08		aplitic granite	31.08.2013	FM008			Melcher
13ZH09		Bt schist	31.08.2013	FM009			Melcher
13ZH10		aplitic granite	31.08.2013	FM010			Melcher
14ZH01		aplitic granite	25.08.2014	FM073	47.157995	12.13916	Melcher
14ZH02		aplitic granite	26.08.2014	FM074	47.156418	12.132571	Melcher
14ZH03		aplitic dyke	26.08.2014	FM075	47.154219	12.133478	Melcher
14ZH04		aplitic granite	26.08.2014	FM076	47.151871	12.138615	Melcher
14ZH05		aplitic granite	26.08.2014	FM077	47.150364	12.128089	Melcher
14ZH06	Mol	aplitic dyke (a) in gneiss (b)	26.08.2014	FM078	47.150756	12.119744	Melcher
14ZH07		gneiss	26.08.2014	FM079	47.150756	12.119744	Melcher
14ZH08	Mol	aplitic dyke in gneiss	26.08.2014	FM080	47.150309	12.11956	Melcher
14ZH09		alpine vein	26.08.2014		47.151441	12.121412	Melcher
14ZH10		alpine vein	26.08.2014	FM081	47.149813	12.130847	Melcher
14ZH11		alpine vein	25.08.2014		47.160939	12.136369	Melcher
14ZH12	Mol	aplitic granite	25.08.2014	FM082	47.156663	12.117582	Mali
14ZH13	Mol	Mol in Qz	24.08.2014		47.167951	12.116846	Unterweissacher
14ZH14	Mol	Mol in Qz	24.08.2014		47.167951	12.116846	Unterweissacher
15RH01	Mol	Mol in pegmatite	14.09.2015	FM085			Melcher
15RH02	Mol	gneiss	14.09.2015	FM086			Melcher
15RH03	Mol	aplitic gneiss	14.09.2015	FM087			Melcher
15RH04	Mol	gneiss	14.09.2015	FM088			Melcher
15RH05	Mol	gneiss	14.09.2015	FM089			Melcher

15RH06	Mol	gneiss	14.09.2015	FM090	47.119958	12.123647	Melcher
15RH07	Mol	gneiss	14.09.2015		47.119958	12.123647	Melcher
15RH08	Mol	gneiss	14.09.2015	FM091	47.119958	12.123647	Melcher
15RH09	Mol	Qz vein	14.09.2015	FM092	47.118933	12.121636	Melcher
15RH10		gneiss	14.09.2015				Melcher
15RH11	Mol	gneiss	15.09.2015	FM093	47.114936	12.134667	Melcher
15RH12		gneiss	15.09.2015	FM094	47.114936	12.134667	Melcher
15RH13	Mol	gneiss	15.09.2015	FM095			Melcher
15RH14		mafic dyke	15.09.2015	FM096	47.114472	12.133033	Melcher
15RH15		aplitic granite	15.09.2015	FM097	47.116742	12.136472	Melcher
15RH16		gneiss	15.09.2015	FM098	47.120594	12.148422	Melcher
15RH17	Mol	gneiss	14.09.2015				Melcher
15RH18	Mol	gneiss	14.09.2015				Melcher
15RH05	Mol	gneiss	14.09.2015	FM099			Melcher
15RH20		gneiss with Alpine vein	14.09.2015	FM100			Melcher
15RH21	Mol	gneiss	14.09.2015				Melcher
15RH22	Mol	aplitic gneiss	14.09.2015				Melcher
15RH23		alpine vein	15.09.2015				Melcher
15RH24	Mol	gneiss	14.09.2015				Melcher
17RH01		Qz vein	01.08.2017		47.12051	12.126220	Melcher, Steiner
17RH02	Mol	aplitic granite	01.08.2017		47.120510	12.126220	Melcher, Steiner
17RH03	Mol	aplitic granite	01.08.2017		47.120309	12.123820	Melcher, Steiner
17RH04	Mol	aplitic granite	01.08.2017		47.117296	12.119988	Melcher, Steiner
17RH05	Mol	gneiss	01.08.2017		47.11729	12.119988	Melcher, Steiner
17RH06	Mol	Joint	01.08.2017		47.122531	12.128260	Melcher, Steiner
17RH07		gneiss	02.08.2017	17RH07	47.12865	12.11438	Melcher, Steiner
17RH08		gneiss	02.08.2017		47.128016	12.114490	Melcher, Steiner
17RH09		aplitic dyke	02.08.2017	17RH09	47.12785	12.114552	Melcher, Steiner
17RH10		Episyenite	02.08.2017		47.127380	12.11661	Melcher, Steiner
17RH11		mafic dyke	02.08.2017		47.12928	12.12088	Melcher, Steiner
17RH12		gneiss	02.08.2017		47.1305	12.11848	Melcher, Steiner
17RH13		vein in gneiss	02.08.2017		47.130517	12.118486	Melcher, Steiner
17RH14	Mol	gneiss	02.08.2017		47.122750	12.130640	Melcher, Steiner
17RH15	Mol	aplitic granite	02.08.2017		47.1227505	12.130640	Melcher, Steiner
17RH16	Mol	aplitic granite	02.08.2017		47.122750	12.130640	Melcher, Steiner
17RH17	Mol	aplitic granite	02.08.2017	17RH17	47.122750	12.130640	Melcher, Steiner
17RH18	Mol	aplitic granite	02.08.2017	17RH18	47.122725	12.13322	Melcher, Steiner
17RH19		Qz syenite	03.08.2017		47.147020	12.140449	Melcher, Steiner
17RH20		aplitic granite	03.08.2017		47.149281	12.13678	Melcher, Steiner
17RH21	Mol	mafic dyke	03.08.2017		47.1492813	12.136780	Melcher, Steiner
17RH22	Mol	gneiss	03.08.2017		47.149515	12.1350087	Melcher, Steiner
17RH23	Mol	Joint	03.08.2017		47.1487111	12.1314801	Melcher, Steiner
17RH24		gneiss	03.08.2017		47.148711	12.131480	Melcher, Steiner
17RH25	Mol	aplitic granite	03.08.2017		47.1467703	12.1369501	Melcher, Steiner
17RH26		aplitic granite	03.08.2017	17RH26	47.146770	12.136950	Melcher, Steiner
17RH27	Mol	aplitic granite	03.08.2017		47.125326	12.1363474	Melcher, Steiner
17RH28	Mol	aplitic granite	09.08.2017		47.1218644	12.1310866	Steiner, Ordosch

17RH29	Mol	aplitic granite	09.08.2017		47.1207559	12.12979	Steiner, Ordosch
17RH30		gneiss	09.08.2017		47.1194789	12.1278649	Steiner, Ordosch
17RH31	Mol	aplitic granite	09.08.2017		47.1194789	12.1278649	Steiner, Ordosch
17RH32	Mol	Qz vein	09.08.2017		47.1156977	12.1315703	Steiner, Ordosch
17RH33		gneiss, hosts 17RH32	09.08.2017		47.1156977	12.1315703	Steiner, Ordosch
17RH34	Mol	aplitic granite	09.08.2017		47.1151637	12.1328473	Steiner, Ordosch
17RH35	Mol	aplitic granite	09.08.2017		47.1151637	12.1328473	Steiner, Ordosch
17RH36		gneiss	09.08.2017		47.1157485	12.1356746	Steiner, Ordosch
17RH37	Mol	gneiss	09.08.2017	17RH37	47.1157485	12.1356746	Steiner, Ordosch
17RH38	Mol	granite	10.08.2017		47.127105	12.1226736	Steiner, Ordosch
17RH39		gneiss	10.08.2017		47.1250858	12.1212962	Steiner, Ordosch
17RH40		aplitic granite	10.08.2017		47.1231352	12.1198383	Steiner, Ordosch
17RH41	Mol	aplitic granite	10.08.2017		47.125003	12.121123	Steiner, Ordosch
17RH42	Mol	aplitic granite	10.08.2017		47.125003	12.121123	Steiner, Ordosch
17PH01		aplitic granite	15.08.2017	17PH01	47.1396895	12.1106812	Steiner, Lassl
17PH02		aplitic granite	15.08.2017		47.1396895	12.1106812	Steiner, Lassl
17PH03		aplitic granite	15.08.2017	17PH03	47.1396895	12.1106812	Steiner, Lassl
17PH04		mafic dyke	15.08.2017		47.1399067	12.1099079	Steiner, Lassl
17PH05	Mol	gneiss	16.08.2017		47.1156089	12.1127844	Steiner, Lassl
17PH06	Mol	aplitic granite	16.08.2017		47.1149914	12.114888	Steiner, Lassl
17PH07	Mol	aplitic granite	16.08.2017		47.1149914	12.114888	Steiner, Lassl
17PH08	Mol	aplitic granite	16.08.2017	17PH08	47.117261	12.1198677	Steiner, Lassl
17PH09	Mol	aplitic granite	16.08.2017	17PH09	47.1169786	12.120134	Steiner, Lassl
17PH10		aplitic granite	16.08.2017	17PH10	47.1170284	12.1193817	Steiner, Lassl
17PH11	Mol	aplitic granite	16.08.2017		47.1159297	12.1175602	Steiner, Lassl
17PH12	Mol	aplitic granite	16.08.2017		47.1170284	12.1193817	Steiner, Lassl
17PH13		aplitic xenolith in mafic dyke	17.08.2017		47.1006453	12.127066	Steiner, Lassl
17PH14		mafic dyke	17.08.2017		47.1006453	12.127066	Steiner, Lassl
17PH15		gneiss	17.08.2017		47.1112002	12.1080498	Steiner, Lassl
18ZT1		gneiss	29.06.2018		47.1344828	12.1340546	Steiner
18ZT2	Mol	aplitic granite	29.06.2018	18ZT2	47.1362167	12.1331162	Steiner
18ZT3		aplitic granite	29.06.2018		47.136216	12.1331053	Steiner
18ZT4	Mol	aplitic granite	29.06.2018		47.1393024	12.1292134	Steiner
18ZT5		aplitic granite	29.06.2018		47.1398505	12.1273108	Steiner
18ZT6		aplitic granite	30.06.2018		47.1416639	12.1145508	Steiner
18RH1		aplitic granite	16.07.2018		47.137494	12.123592	Steiner
18RH2	Mol	aplitic granite	16.07.2018		47.141307	12.128129	Steiner
18RH3		aplitic granite	16.07.2018		47.136252	12.133122	Steiner
18PH1		gneiss	17.07.2018		47.116859	12.104134	Melcher, Steiner
18PH2	Mol	aplitic granite	18.07.2018		47.111614	12.110813	Melcher, Steiner
18PH3	Mol	gneiss	18.07.2018		47.111677	12.111131	Melcher, Steiner
18PH4		gneiss	18.07.2018	18PH4	47.111889	12.112582	Melcher, Steiner
18PH5	Mol	gneiss	18.07.2018	18PH5	47.111975	12.112997	Melcher, Steiner
18PH6		gneiss	18.07.2018	18PH6	47.112644	12.117775	Melcher, Steiner
18PH7	Mol	aplitic granite	18.07.2018		47.111393	12.121841	Melcher, Steiner
18PH8	Mol	Qz vein	18.07.2018		47.111327	12.122787	Melcher, Steiner
18PH9	Mol	aplitic granite	18.07.2018		47.111626	12.124101	Melcher, Steiner

18PH10	Mol	aplitic granite	18.07.2018		47.109885	12.115954	Melcher, Steiner
18PH11		gneiss	19.07.2018		47.101033	12.113757	Melcher, Steiner
18PH12	Mol	aplitic dyke	19.07.2018		47.106171	12.090047	Melcher, Steiner

XRF analyses

Major elements (oxides) are given in percent, trace elements are given in ppm.

sample	13ZH01	13ZH02	13ZH03	13ZH06	13ZH08	14ZH01	14ZH02	14ZH03
lithology	gneiss	gneiss	gneiss	gneiss	aplitic granite	gneiss	aplitic granite	aplitic granite
total	96.46	98.43	97.47	98.59	99.12	97.56	97.58	96.32
LOI	0.34	0.61	2.16	1.14	0.23	1.17	0.06	0.40
SiO2	74.745	76.82	72.573	76.356	76.984	73.05	76.475	75.761
TiO2	0.076	0.089	0.217	0.136	0.046	0.261	0.056	0.037
Al2O3	12.688	13.412	12.537	13.216	13.189	13.221	12.248	12.291
Fe2O3	0.693	0.675	1.863	0.661	0.658	2.45	0.615	0.694
MnO	0.006	0.014	0.059	0.004	0.088	0.058	0.011	0.04
MgO	0.125	0.299	0.56	0.116	0.065	0.61	0.094	0.129
CaO	0.413	0.456	2.964	0.439	0.493	2.128	0.636	0.612
Na2O	3.568	5.191	3.52	3.578	3.242	2.395	2.4	3.732
K2O	4.068	1.407	2.834	4.008	4.272	3.204	4.989	2.941
P2O5	0.023	0.018	0.242	0.019	0.013	0.067	0.003	0.005
Cu	10.1	0.3	25.2	8.7	2.95	2.8	0.95	3.5
Ce	8.8	72.5	19.4	68.1	77.2	96.8	72.6	58
Nb	37.2	23.4	19.8	49.6	18.7	12.6	10.7	12.9
Zr	80.9	46.1	113.1	79.5	44.9	106.6	44	107.1
Y	50.6	18.5	31	52.3	54.1	25.5	26.7	40.7
Sr	31.7	75.8	161.5	32.7	13.6	156.6	89.8	149.9
Rb	153	60.7	110.9	147.2	227.5	114.8	127.6	64.7
Th	25.2	11.5	14.2	19.1	3.7	11.9	15.9	31.5
Pb	38.3	4.8	22.9	34.3	33.3	11.5	17.8	26.5
Ga	21.1	18.3	19.6	21	22.6	20.1	16	20.7
Zn	16.2	17.8	30.5	15.5	11.9	45.9	11.1	13.9
Ni	3	0.4	5.2	0.4	0.75	1	2.4	5.5
Co	1.3	1.7	4.6	0.5	0.85	5.1	0.15	0.9
V	0.2	7.1	19.4	6.4	4.6	28.8	2.3	0.2
La	6.1	12	32.2	17.4	12.9	20.2	22.3	1.3
Ba	25.8	13.6	329.2	8.75	59.6	458.1	52.8	181.9
Sc	16.1	15.9	15.9	16.1	16	15.9	16	16
Cr	1.6	2	0.55	2.9	2.2	3.4	5.6	1.75
Cs	0.3	4.9	23.2	13.3	40	15.4	0.6	15.8
Hf	3.9	6.4	4	1.3	0.5	1.3	0.2	7.2
Nd	7.1	31.8	25.4	19.1	25.7	20.2	27	10.5

sample	14ZH04	14ZH05	14ZH06a	14ZH06b	14ZH07	15RH02	15RH03	15RH07
lithology	aplitic granite	aplitic granite	gneiss	gneiss	gneiss	gneiss	aplitic granite	gneiss
total	96.90	98.05	98.46	96.55	97.58	97.12	97.76	98.07
LOI	0.22	0.27	0.28	0.55	0.43	2.98	0.17	0.80
SiO2	75.464	76.113	76.321	70.671	70.715	62.901	75.344	77.344
TiO2	0.053	0.05	0.028	0.334	0.322	0.101	0.08	0.099
Al2O3	12.503	12.518	12.781	13.896	13.928	18.539	12.961	12.275
Fe2O3	0.779	0.835	0.43	3.102	3.011	0.665	0.729	0.719
MnO	0.032	0.035	0.012	0.094	0.061	0.045	0.015	0.011
MgO	0.102	0.102	0.101	0.809	0.724	1.045	0.104	0.23
CaO	0.658	0.666	0.628	1.875	2.28	3.625	0.79	0.468
Na2O	2.688	2.649	1.933	2.789	2.537	7.1	2.748	2.773
K2O	4.559	5.01	6.093	2.785	3.775	2.985	4.908	4.028
P2O5	0.004	0.009	0.004	0.083	0.086	0.012	0.014	0.033
Cu	0.65	4	2.1	1.4	2.8	2.6	6.7	2.9
Ce	65.5	88.3	105.8	106.5	47.5	87	44.8	0.95
Nb	14.7	16.1	12	33.1	18.9	27.4	17	10.8
Zr	62.9	85.7	56.3	135.5	144.5	107.4	54.3	72.1
Y	38.2	43.8	63.2	34.5	27.9	70.3	52.2	24.3
Sr	32.9	32.5	136.9	119.3	152.6	124.2	41.2	102.2
Rb	187.1	186.5	147.1	135	141.4	109.7	188.6	110.9
Th	24	29.7	14.4	18.2	14.3	36	16.7	7
Pb	25.1	31.5	23.9	14.4	18.9	20.2	32.6	12.5
Ga	18.5	17.5	20.1	23	20.6	20.1	21.6	18.9
Zn	17.6	22	6.7	65.3	55.8	15.6	15.1	10.9
Ni	3.5	0.6	0.9	3.9	3.9	0.7	0	0.2
Co	1.45	0.9	2.45	2.1	5.4	1.6	0.65	1.05
V	0.25	1.05	0.45	33.4	42.2	10.4	3.9	7.8
La	12.2	22	21.6	41	39.6	40	17	0.7
Ba	31.05	9.8	578	314	622.5	283.8	49.5	492.9
Sc	16	16	16.1	15.9	16	15.9	16.1	16.1
Cr	3.15	5.4	9.3	4.7	3.1	3.55	11	1.15
Cs	3.75	10.4	18.2	6.8	6.35	7.6	0.6	0.7
Hf	9.8	6.8	8.3	7.6	7.9	5.1	11.2	6
Nd	23.8	21.3	23.9	23	20.2	24.7	22.6	12.2

sample	15RH08	15RH09	15RH12	15RH13	15RH15	15RH16	17PH01(2)	17PH01
lithology	gneiss	Qz vein	gneiss	aplitic granite	aplitic granite	gneiss	aplitic granite	aplitic granite
total	97.9	97.61	100.07	95.99	97.66	98.8	96.34	96.58
LOI	0.46	0.84	0.57	0.87	0.27	0.53	0.42	1.57
SiO2	73.078	73	76.957	72.102	75.756	75.208	74.609	74.821
TiO2	0.135	0.048	0.115	0.203	0.074	0.141	0.049	0.049
Al2O3	13.93	14.194	13.368	12.937	12.81	13.413	12.531	12.583
Fe2O3	1.26	0.862	1.16	1.96	0.63	1.328	1.02	1.019
MnO	0.024	0.006	0.028	0.043	0.01	0.031	0.044	0.046
MgO	0.307	0.125	0.233	0.413	0.1	0.278	0.114	0.112
CaO	1.033	0.779	0.887	1.307	0.746	1.055	0.582	0.584
Na2O	2.56	4.034	2.744	2.153	2.743	2.869	2.842	2.807
K2O	5.377	4.461	4.465	4.689	4.735	4.324	4.463	4.479
P2O5	0.042	0.012	0.051	0.076	0.008	0.047	0.01	0.011
Cu	14.4	22.4	10.9	2.1	0.6	0.25	1.6	2.3
Ce	59.6	63.1	44.1	32.9	7.9	20.5	51.8	62
Nb	12.1	12.5	21.7	15.6	10.3	13.7	16.9	17.2
Zr	92.1	57.8	70.2	109.5	40.8	93.2	68.8	67.9
Y	33.9	36.4	39.1	37.9	23.3	33.1	45.8	43.6
Sr	177.6	90.3	52.1	140.2	143.4	162.5	34.2	31.8
Rb	160.3	132.6	190.6	182.6	118.9	143.1	186	184.6
Th	10	31.2	12.7	10.2	9.3	8.4	22.7	24.4
Pb	21.9	24.1	31.2	17.2	30.8	24.9	17.4	18.3
Ga	21.7	18.7	22.9	20.9	18	19.5	11.6	13.1
Zn	21.8	16.4	21.2	33.1	14	20.7	25.4	21.5
Ni	3.5	0.75	2.1	0.5	0	1.65	5	4.9
Co	0.25	1.55	1.5	0.05	0.1	0.15	0.1	1.6
V	13.8	0.1	7.7	17.7	6.8	13.2	2.15	1.2
La	39.2	19.4	3.1	17.3	5.45	32	21.7	17.7
Ba	819.8	282.6	11.7	360.1	41.3	466.1	179.1	105.3
Sc	15.9	16.1	16.1	15.9	16.2	16.1	16.2	16
Cr	1.35	1.25	8.7	0.35	2.4	6	6.9	5.25
Cs	11.2	4.45	22.4	6.4	12.65	5.4	17.5	13.2
Hf	8.9	4.5	1.4	3.6	2.4	6.5	5.2	6.9
Nd	27	25.8	17.1	11.3	8.9	20.7	25.7	25.1

sample	17PH03	17PH08	17PH09	17PH10	17RH07	17RH17	17RH26	17RH37
lithology	aplitic granite	aplitic granite	aplitic granite	aplitic granite	gneiss	aplitic granite	aplitic granite	gneiss
total	97.98	96.43	98.05	96.39	98.13	97.43	97.28	97.33
LOI	0.53	1.15	0.33	1.31	0.43	0.31	0.08	0.50
SiO2	76.363	75.605	75.789	73.369	72.328	74.584	75.097	72.37
TiO2	0.053	0.083	0.085	0.109	0.241	0.138	0.052	0.24
Al2O3	13.17	12.461	12.944	13.212	14.09	12.977	12.663	13.631
Fe2O3	0.673	0.7	0.862	1.087	2.477	1.292	1.197	2.273
MnO	0.063	0.014	0.02	0.025	0.057	0.03	0.056	0.067
MgO	0.159	0.14	0.148	0.176	0.892	0.266	0.069	0.498
CaO	0.47	0.208	0.534	1.026	1.205	1.16	0.636	1.656
Na2O	2.555	2.744	2.503	2.638	3.752	2.462	2.9	2.777
K2O	4.363	4.404	5.09	4.66	2.878	4.364	4.515	3.615
P2O5	0.023	0.012	0.018	0.022	0.075	0.072	0.01	0.081
Cu	2.8	6.8	0.05	1.9	0.7	0.8	4	1
Ce	110.4	22.8	72.7	32	26.6	51	95.5	30.1
Nb	24.8	20.7	22.5	18	14.8	20.5	21.8	18.3
Zr	48.5	66.2	72.3	57.9	141.8	95.8	78.4	127.2
Y	43.9	38.2	51.9	29.8	23.3	52.4	49.7	32.5
Sr	29.2	66.3	77.7	89.8	123.8	87.3	37.7	177.8
Rb	198.5	139.4	178.8	162.2	108.5	185.8	176.8	154.3
Th	5.2	11.6	22.3	17.4	21.1	20.8	18.5	18.4
Pb	65.6	24.8	17.4	25.2	19.3	21.2	31.9	19.3
Ga	16	11.4	13.7	12.4	10.7	16.2	12.1	14.1
Zn	160.2	11.1	13.9	25.2	49.2	24.5	35.9	44.9
Ni	0.8	21.4	0.05	53.1	0	39	19	5.9
Co	0.95	0.4	1.75	1.3	2.6	1.8	2.8	5.5
V	2.6	6.1	2.5	13.9	23.5	4.5	0.1	24.3
La	23.4	19.7	7.6	22.7	22.3	27.6	23.6	36.8
Ba	39.2	40.9	7.5	40.5	733.9	95.3	190.6	411.1
Sc	16.2	16.1	16.2	16.1	16	16	16.1	16.1
Cr	7.5	6.75	2.35	9.75	6.55	0.9	7.9	5.15
Cs	4.8	25.5	7.2	20.8	14.9	31.1	5.05	4.5
Hf	7.8	3	4.1	5.4	12.3	6.3	1.5	1.5
Nd	32.7	16.2	24.2	15.6	23.9	20.3	31.7	23.6

sample	18PH1	18PH9	18PH11	18PH12	18ZT3	18ZT5
lithology	gneiss	aplitic granite	gneiss	aplitic granite	aplitic granite	aplitic granite
total	98.82	96.80	98.85	98.22	98.62	97.80
LOI	0.69	0.74	0.34	0.59	0.21	0.39
SiO2	73.01	74.38	71.88	76.02	76.34	72.88
TiO2	0.28	0.06	0.32	0.05	0.04	0.17
Al2O3	14.35	13.2	14.8	13.02	12.87	13.79
Fe2O3	2.28	0.51	2.67	0.39	0.81	1.98
MnO	0.04	0.01	0.05	0.01	0.03	0.05
MgO	1.23	0.11	0.77	0.09	0.07	0.36
CaO	1.13	0.65	1.25	0.74	0.52	1.69
Na2O	3.31	2.74	3.12	3.16	3.1	3
K2O	3	5	3.75	4.64	4.75	3.68
P2O5	0.08	0.08	0.1	0.02	0.01	0.05
Cu	1.55	1.55	1.55	1.55	1.55	1.55
Ce	72.7	58.9	89.4	51.7	96	41.8
Nb	15.8	23.6	18.3	14.8	11.2	14.8
Zr	134.1	34.1	144.7	37.3	53.6	109.7
Y	26.2	41.4	27.8	32.2	39.6	24.2
Sr	79.1	35	160.5	116.2	24	135.6
Rb	110.5	203	137.3	130.5	174.2	128.1
Th	13	12.3	18.8	18.8	29.3	14.5
Pb	5.5	21.4	20.6	41.7	29.4	26.8
Ga	20	18.4	20.8	18.9	18.2	18.7
Zn	39.9	8.3	53.1	7.5	21.1	42.3
Ni	0.9	0.9	0.9	0.9	0.9	0.9
Co	1.45	1.45	1.45	1.45	1.45	1.45
V	31.9	6	32.4	12	9.2	18.4
La	26.2	22.3	22	33.9	38.1	46.9
Ba	517.2	93.8	611.6	230	167.9	827.3
Sc						
Cr	2.2	2.2	2.2	2.2	2.2	2.2
Cs						
Hf	1.15	4.8	4.9	5.8	8.2	5.2
Nd	24.4	29.4	45.7	25.2	35.8	28